

Strategies To Improve the Impedance Control Performance of a Quadruped Robot



Michele Focchi

University of Genoa, Italy

Istituto Italiano di Tecnologia (IIT)

A thesis submitted for the degree of

Doctor of Philosophy (Ph.D.)

April 2013

Thesis Supervisors:

Prof. Jonas Buchli

Professor

Agile & Dexterous Robotics Lab

Swiss Federal Institute of Technology Zurich (ETH Zurich)

Dr. Claudio Semini

HyQ Group Leader

Department of Advanced Robotics

Istituto Italiano di Tecnologia (IIT)

Prof. Darwin G. Caldwell

Director

Department of Advanced Robotics

Istituto Italiano di Tecnologia (IIT)

Copyright © 2013 by Michele Focchi
All rights reserved

A mio padre, origine di ogni mia passione
e a mia madre per la sua instancabile amorevole presenza

Abstract

The goal of this PhD thesis is to present strategies to improve the control of interaction forces that occur during the locomotion of a legged robot with the aim to improve its robustness and safety. Until recently, the majority of legged robots employ high gain (stiff) position feedback control. However, a locomotion control strategy based on joint position control is not sufficient anymore when interaction forces are present.

Impedance control and torque/force based control methods are necessary to address the difficult task of successfully traversing uneven and rough terrains where prior knowledge of the terrain is not available or when the ground model or the robot state estimation is inaccurate. In particular the first part of this work focuses on the low-level controller of the robot: impedance control is implemented with torque control in a nested loop arrangement. High bandwidth torque control is a desirable feature to be able to straightforwardly implement model based or impedance control schemes. When performing torque control, it is shown that the load (e.g. the leg) dynamics can strongly limit the closed-loop control performance. A strategy called *velocity compensation* is proposed to overcome this limitation and enhance the torque bandwidth. This work also discusses the important topic regarding the stability of the robot both with and without the contact with the environment. As a matter of fact there are several factors (sampling, filtering, inner loop bandwidth, actuator dynamics) that play a role in restricting the range of impedance parameters (*stability region*) that can be set, for which the system remains stable. Some practical rules of thumb for the selection of impedance parameters that are more suitable for locomotion are also suggested.

On one hand, a lower bandwidth in the torque loop enlarges the region of stable parameters, on the other hand it limits the range of frequency in which the desired impedance can be emulated (tracked). This can be an undesirable limitation when dealing with impact forces that usually have high frequency content. In particular, a delay of the impedance controller can result in high peak forces in the first milliseconds of the impact that are directly transmitted to the structure. This can

lead to damage of the weakest components (e.g. gearboxes and loadcells) and, over time, to fatigue fractures. To tackle this problem, the second part of this work investigates the introduction of passive compliant elements in the robot. In particular two prototypes of compliant feet have been built and evaluated: one with only a passive spring (*passive foot*) and the other one with actively controlled damping by means of magneto-rheological fluids (*MR foot*).

The main contribution of this thesis, is a methodology to analyze (based on an accurate model of the system) the joint stability and passivity taking into consideration all the non-idealities present in real implementation of an impedance controller (actuator dynamics, discrete implementation, filtering, nested loops). The analysis is presented for the adduction/adduction joint of the HyQ robot but will be extended to all the robot joint. This is the first step of a bigger project that involves the development of a gain scheduler (in the low-level control layer) to adapt the bandwidth of the inner torque loop according to the impedance parameters set by the user. The final purpose is, given the desired user specifications, to satisfy passivity and stability in all robot configurations while maximizing the range of frequency where the impedance is tracked (impedance bandwidth).

Contents

Contents	v
1 Introduction	1
1.1 Motivations	2
1.2 Contributions	5
1.3 Outline of the thesis	7
2 Background and related work	9
2.1 Legged robotics	9
2.2 Torque control	13
2.3 Impedance control	16
2.4 Passivity	18
2.5 Passive compliance	19
2.6 HyQ platform description	20
3 Improved torque control of electric actuators	25
3.1 Motivations	25
3.2 System description	26
3.3 Model with two inertias	27
3.4 Inherent limitations of the torque bandwidth	29
3.4.1 Load velocity influence on force dynamics: a simple example	31
3.4.2 Load velocity compensation by positive velocity feedback for a simple mechanical system	33
3.4.3 Load velocity compensation by positive velocity feedback for the electric actuator (model with two inertias)	33
3.4.4 Practical implementations of positive velocity feedback	36
3.5 Model with three inertias	38

CONTENTS

3.5.1	Influence of gravity	44
3.5.2	Load velocity compensation by positive velocity feedback for the electric actuator (model with three inertias)	44
3.5.3	Practical implementation of positive velocity feedback and discussion .	46
3.6	Torque controller design	47
3.7	Torque compensator to compensate harmonic drive cyclic friction	50
3.8	Summary	52
4	Impedance control	55
4.1	Impedance control for the adduction/abduction joint	55
4.1.1	Motivation	55
4.1.2	Implementation	56
4.1.3	Stability regions	57
4.1.4	Passivity analysis	60
4.1.5	Rejection of the torque ripple in the impedance loop	63
4.1.6	Impedance tracking	64
4.1.7	Torque tracking with outer impedance loop	67
4.1.8	Summary	69
4.2	Impedance control for the whole leg	69
4.2.1	Joint space implementation	70
4.2.2	Task space implementation	71
4.2.2.1	Motivation	71
4.2.2.2	Implementation	73
4.2.2.3	Experiments	76
4.2.3	Specifying performances for impedance control	77
4.2.4	Ground reaction forces	81
4.2.5	Summary	83
5	Passive compliance in robot legs	85
5.1	Selection of the passive compliance	87
5.1.1	Discussion	90
5.2	Experiments	91
5.2.1	Drop tests	91
5.3	Flying trot without torque control at the joints	93
5.4	Summary	94

CONTENTS

6	Semi-active damping with magneto-rheological fluids	95
6.1	Magneto-rheological fluids and damper	96
6.2	Robotic leg with MR foot	96
6.3	Control algorithm	98
6.3.1	Critical damping law	98
6.4	Experimental results	101
6.5	Generalization	101
6.6	Discussion and limitations	102
6.7	Summary	103
7	Discussion and Conclusions	105
7.1	Discussion	105
7.1.1	Discrete time	110
7.1.2	Open-loop actuator dynamics vs power limitation	110
7.1.3	Safety: active vs passive compliance	111
7.2	Conclusions	112
7.3	Future works	113
A	Miscellaneous mathematical derivations	115
A.1	Derivation of the velocity compensation gain for the model with two inertia	115
A.2	Derivation of the torque transfer function for the model with three inertia	117
A.3	Derivation of the torque transfer function for the model with three inertia, with velocity compensation	119
B	Design of components	121
B.1	Six axis foot sensor design	121
B.1.1	Specifications for a six axis foot sensor	121
B.1.2	Selection of the sensing technology	122
B.1.3	Design guidelines	123
B.1.4	Calibration	126
B.1.5	Experimental results	128
B.1.5.1	Static tests	128
B.1.5.2	Dynamic tests	130
B.2	Passive foot design	133
B.2.1	Design choices	135
B.2.1.1	Bearing	135
B.2.1.2	Shaft	135

CONTENTS

B.2.1.3	Springs	135
B.2.1.4	Displacement sensor	136
B.3	Construction of the magneto-rheological compliant foot	136
B.3.1	Performances	138
B.3.1.1	Frequency response measurements	139
B.4	Publications and patents	141
B.5	List of publications	141
B.6	Patents	142
B.7	Awards	143
	References	145

List of Symbols

Roman Symbols

α	velocity compensation (scalar) gain
β	gain of the PI torque controller
Δt	time interval that indicates the duration of the compression phase used to estimate m_{eq} (MR foot)
\dot{x}_l	load velocity (generic spring-mass mechanical model)
\dot{x}_{vs}	velocity of the velocity source (generic spring-mass mechanical model)
ω_d	damped natural frequency of the bouncing dynamics (MR foot)
ω_n	damping factor of the bouncing dynamics (MR foot)
ω_h	natural frequency of the bouncing dynamics (MR foot)
σ	yield stress of the material
θ_l	angular position of the rigid bar (load) (model with two inertias)
θ_m	angular positions of the rotor of the electric motor (model with two inertias)
θ_{L1}	angular position of the intermediate inertia (load) (model with three inertias)
θ_{L2}	angular position of the leg (model with three inertias)
$\tilde{\mathbf{A}}$	State matrix of the state space representation of a rigid body mass controlled with a feedback action F_b from position and velocity
$\ddot{\mathbf{q}}$	vector of joint accelerations (whole leg)
$\ddot{\mathbf{x}}$	vector of Cartesian accelerations at the end-effector (whole leg)

CONTENTS

$\dot{\mathbf{q}}$	vector of joint velocities (whole leg)
$\dot{\mathbf{q}}_{ref}$	vector of desired joint velocities (whole leg)
Γ	vector of generalized torques of a floating base robot
λ	vector of ground reaction forces for a floating base robot
τ	vector of actuation torques (whole leg)
τ_{lref}	vector of desired actuation torques (whole leg)
$\tilde{\mathbf{M}}_x$	joint space inertia matrix discarding the off-diagonal terms and considering only the diagonal ones
\mathbf{C}_h	channel matrix (foot sensor)
\mathbf{D}_x	desired Cartesian damping matrix (whole leg)
\mathbf{D}_θ	desired joint space damping matrix (whole leg)
\mathbf{F}_{int}	vector of Cartesian interaction forces (whole leg)
\mathbf{F}	force matrix (foot sensor)
\mathbf{F}_b	feedback from position and velocity to control a rigid body mass
\mathbf{F}_{ref}	vector of desired Cartesian interaction forces (whole leg)
\mathbf{h}	vector of centrifugal/coriolis/gravity torques (whole leg)
\mathbf{J}	leg jacobian
$\mathbf{J}_C(q)$	contact constrain Jacobian of a floating base robot
\mathbf{K}_x	desired Cartesian stiffness matrix (whole leg)
\mathbf{K}_θ	desired joint space stiffness matrix (whole leg)
\mathbf{P}_{des}	desired eigenvalues for a rigid body mass
\mathbf{q}	vector of joint positions (whole leg)
\mathbf{q}_r	vector of joint positions of a floating base robot
\mathbf{q}_{ref}	vector of desired joint positions (whole leg)

CONTENTS

T	transformation matrix (foot sensor)
x	vector of Cartesian position of the end-effector (whole leg)
x_b	vector of base positions of a floating base robot
x_{ref}	vector of desired Cartesian position of the end-effector (whole leg)
$Z(z)$	vector of Cartesian impedances (whole leg)
A	State matrix of the state space representation of a rigid body mass
B	Input matrix of the state space representation of a rigid body mass
B_m	viscous friction rotor
B_l	viscous friction friction link-side (model with two inertias)
$C_{comp}(z)$	torque compensator to reduce the torque ripple disturbances generated by the harmonic drive gearbox
D_a	Actively controlled damping in the vertical direction (spring-mass model)
D_f	passive damping in the MR foot
D_{gain}	desired damping at joint level
D_{MR}	damping coefficient used in the critical damping law (MR foot)
D_p	leg damping (model with three inertias)
D_{te}	gearbox damping (model with three inertias)
E	young modulus of the material
F	output force (generic spring-mass mechanical model)
F_D	controllable damping force (MR foot)
$G_t(s)$	transfer function between voltage and load torque
$G_{t_{VC}}$	transfer function between voltage and load torque after velocity compensation
I_m	motor current
I_t	torque controller integral gain

CONTENTS

J_{L1}	intermediate inertia (model with three inertias)
J_{L2}	leg inertia (model with three inertias)
J_l	rigid bar (load) inertia (model with two inertias)
J_m	rotor + gearbox inertia
K_a	Actively controlled damping in the vertical direction (spring-mass model)
K_f	stiffness of the compliant foot
K_p	Passive compliance in the vertical direction (spring-mass model)
K_t	stiffness of the transmission (generic spring-mass mechanical model)
k_t	electric motor torque constant
k_w	electric motor speed constant
K_{comp}	DC gain of the torque compensator
K_{env}	Environmental stiffness
K_{L2}	linear stiffness due to gravity
K_{MR}	stiffness coefficient used in the critical damping law (MR foot)
K_p	leg stiffness (model with three inertias)
K_{ratio}	dimensionless parameter that represents the virtual stiffness as a fraction of the passive stiffness K_f
K_{te}	gearbox stiffness
k_{xx}	desired Cartesian stiffness in the X direction
k_{yy}	desired Cartesian stiffness in the Y direction
L	Coil inductance
M_b	body mass (spring-mass model)
m_i	Intermediate inertia (spring-mass model)
M_l	load mass (generic spring-mass mechanical model)

CONTENTS

m_u	Unsprung mass of the foot tip (spring-mass model)
M_θ	joint space inertia matrix (whole leg)
m_{eq}	equivalent body mass seen by the spring
N	Gear ratio
N_{av}	number of samples used in the MA averaging filter of the link velocity
P_t	torque controller proportional gain
P_{gain}	desired stiffness at joint level
$PI_t(z)$	PI torque controller
R	Coil resistance
T_l	load torque
T_s	sampling time
t_s	Settling time for the critical damping control law (MR foot)
T_{dist}	external disturbance torque (load side)
T_{ffwd}	feed forward torque at joint level
T_{fr}	friction disturbance torque (motor side)
T_{lref}	reference torque at joint level
V_m	motor voltage
$V_{m_{VC}}$	velocity compensation voltage
$VC(s)$	velocity compensation transfer function
x_{FCE}	displacement of the foot compression/extension <i>FCE</i> joint
x_l	load position (generic spring-mass mechanical model)
x_{vs}	position of the velocity source (generic spring-mass mechanical model)
$Z(s)$	load impedance expressed at joint level
\mathbf{u}	vector of input forces to a generic rigid body mass

CONTENTS

1

Introduction

THIS dissertation deals with the force/motion control of a legged robot. The research on legged robots has been getting more and more widespread interest because legged machines are more suitable to traverse rough terrains with respect to wheeled vehicles. Legged locomotion has been used for hundred of millions of years in the animal kingdom while only recently wheeled vehicles appeared in the history. Approximately half of the earth land surface is inaccessible to either wheeled or tracked vehicles [Song and Chen, 1991] while animals and humans traverse such terrain with ease and elegance. Wheels perform better on flat, regular or uniform surfaces but reach their limits when dealing with very rough terrain. Conversely legs have the potential to increase the mobility of robots. In the robotics community, developing an autonomous machine able to elegantly move in the real world outside the laboratory was an important goal to achieve. The main reason for which legged machines are not as diffused as the wheeled counterpart is their difficulty to control and construct them. Until the 1980's computational power was not enough to perform the necessary computations and the computers were not sufficiently compact and light to be included on board of a legged robot. Advances in technology and recent environmental disasters (e.g. Fukushima 2011) highlighted the need to develop high-performance legged machines that are able to navigate areas deemed unsafe for humans (chemical gases, explosives, radiation), to provide critical assistance to humans in search and rescue operations. Recent research projects (DARPA's robotics challenge) and the development of the quadruped robot called BigDog [Raibert et al., 2008] by Boston Dynamics are just a few examples of the increased interest in the area of legged locomotion. We can find examples of autonomous walking machines in the past [Frank, 1968; Liston and Mosher, 1968]. Even though these robots used different kind of actuation (one hydraulic and the other electric) both of them shared a common feature: they employ high gain position control for the motion of the legs. This reflects a widespread habit in robotics from the last 30

1. INTRODUCTION

years, that focus on high gain position control and kinematic planning, striving to maximize tracking accuracy. This habit is rooted in the high-precision requirements of industrial robot manipulators where "the stiffer, the better". This works well in structured and well-known environments with relatively low locomotion speed. However high gain position control turns out to be unsuitable when highly dynamic locomotion is desired or in situations involving contact with unknown and unstructured environments, where the necessity to be compliant to external impacts becomes a crucial requirement.

1.1 Motivations

Compliance in a robotic system can be achieved passively or actively. Passive compliance consists in using physical components such as springs and dampers between the robot and the environment to limit the interaction forces. However the values of the compliance is fixed and is not adaptable to the changing condition of the environment. An alternative solution is to actively control the compliance (e.g at the foot). Indeed, a major benefit of active compliance is its flexibility to change the dynamic characteristics (e.g such as stiffness and damping) through software, without the need of physical compliant components. This represents a significant improvement of the versatility of a robot which needs to change leg stiffness to adapt to terrains with different surface properties [Ferris et al., 1998b]. There are many ways of actively controlling the compliance and the interaction forces at the end-effector, such as impedance control [Hogan, 1985], operational space control [Khatib, 1987], hybrid force-control [Raibert and Craig, 1981].

Impedance control is a useful framework to allow the robot to follow reference trajectories and, at the same time, handle external disturbances which are always present in dynamic legged locomotion. An application of impedance control is the implementation of virtual components [Pratt et al., 2001], such as springs and dampers, that can be virtually attached between different points on the robot. This allows to create the same forces as if a physical counterpart was attached between these points. It is important to remark that a virtual spring has not the energy storing capabilities of a real one because is actively rendered by the actuators. In fact actuators are only able to dissipate (negative work) or produce (positive work) energy not to store it. Furthermore, virtual models can change their characteristics (e.g. stiffness) as a function of time according to the situation. For instance, if a virtual spring is attached between the hip and the foot, its compliance can be set to a stiff value during the stance phase to reduce sag of the robot under its own weight (unless a model based controller is present that performs gravity compensation). During the swing phase it can be set to another value to effectively negotiate terrain asperities that might hamper the leg's motion. There are several control architectures

1.1. Motivations

that can be used to realize impedance control. All rely on closing an outer impedance control loop around an inner control loop. The inner loop can be a position loop (position based impedance control), an inner torque/force loop (torque based impedance control) or an inner velocity loop (velocity based impedance control) [Mosadeghzad et al., 2012]. Since robots are typically modeled as rigid body systems, they have torques as inputs to their dynamics. This was one of the motivations to implement a high-fidelity low-level torque control at the joints. Considering the actuators as high-fidelity torque sources that are able to apply the desired joint torques to a given robot structure has many advantages. The principal one is that torque control allows to straightforwardly implement different kinds of controllers like rigid body dynamics model-based control [Sciavicco and Siciliano, 2000] (e.g. inverse dynamics) and virtual model control [Pratt and Williamson, 1995] as well as impedance control. Moreover, the main disturbances present in legged locomotion are the ground impact forces which are best dealt within the force/torque domain. However, real implementations of torque control and impedance control with an inner loop suffer from several limitations that will be listed in Section 1.2.

All the controllers presented in this thesis are designed for the robotic platform called HyQ [Semini, 2010]. HyQ (which stands for *Hydraulic Quadruped*) is a quadruped robot which

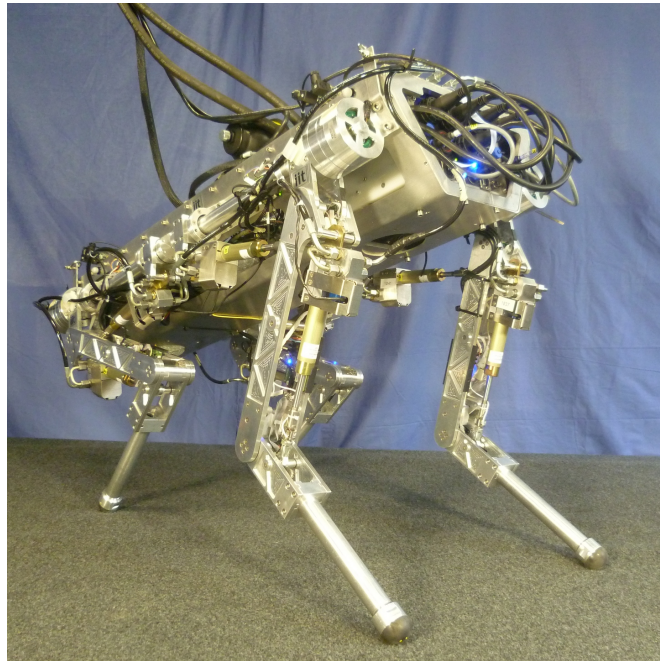


Figure 1.1: HyQ quadruped robot.

was designed to be a versatile platform which implements capabilities that normally belong to the animal kingdom. Namely being able to achieve precise and accurate foothold selection

1. INTRODUCTION

and positioning while keeping balance, to negotiate very rough terrain (climb over obstacles, move along steep slopes) as well as perform highly-dynamic movements (running, jumping). Moreover, compared to bipeds, quadruped robots offer unique advantages due to their high-load carrying capacity and low mechanical complexity. In HyQ we used a control architecture where an impedance controller is closed around an inner torque loop at joint level. Figure 1.2 depicts this architecture for one joint, where θ and θ_{ref} are the joint actual and desired position, respectively. The output of the impedance controller is fed as a reference torque T_{ref} to the inner torque loop. Torque and position sensors feed back the joint torque (T_l) and position (θ) measurements. The output of the torque controller u is the command sent to the actuator.

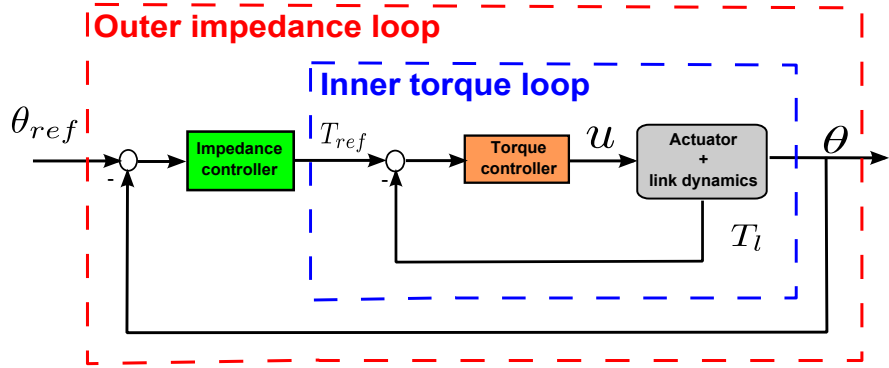


Figure 1.2: Block diagram of impedance control with an inner torque loop for a generic joint.

Let us consider first the torque loop alone. Whenever torque is controlled on a load that is free to move (e.g. the links of a leg of HyQ) and not rigidly fixed to the ground, limitations on the torque bandwidth arise that depend on the dynamics of the load. This holds in general and is not strictly related to a specific actuation technology. The cause of this limitation is the presence of an intrinsic (*natural*) load velocity feedback that exists in the torque dynamics. In this situation, increasing the controller gains does not improve tracking performance and can lead to instability. This problem has been largely overlooked in the past, since in many cases the load dynamics are ignored in the analysis [Williamson, 1995], [Pratt et al., 1997].

When an outer loop is closed around the inner loop, the dynamics of the controlled system changes, and mutual influences exist between the inner and the outer loop. Neglecting these mutual interactions might lead to results and conclusions that are incorrect and not representing reality. A common practice in designing nested loop control systems is to maximize the bandwidth of the innermost loop. This is a widely spread belief that many researchers assume to be valid [Ellis, 2000; McMillan et al., 1999] without carrying out the relevant analysis. More in detail, maximizing the bandwidth of the inner loop can be useful to enlarge the range of frequencies in which the real impedance *tracks* the desired one, but it reduces the range of

impedance parameters for which the whole system is stable (*stability region*). Other limitations arise in the real implementations of the controller (e.g. in discrete time), that directly influence the stability region, such as the sampling frequency and sensor signal filtering [Janabi-Sharifi et al., 2000]. They both introduce delays into the control loop.

The stability of the robot must be investigated also when it is interacting with the environment. Indeed, a system that is stable can become unstable whenever interacting with a certain kind of environment. The property that ensures the stability of the system also during the interaction is *passivity* that is a more strict condition than just stability.

In case the robot is equipped with low-bandwidth actuators, a high bandwidth for the impedance control is hard to be achieved. In these cases the actuator is not able to track the impedance sufficiently fast to deal with the impact forces due the interaction with the ground. Since the only compliance in the HyQ leg is represented by the passive compliance in the hydraulic actuators (which is low), whenever the controller delays to intervene, high peak forces may occur. These forces are directly transmitted to the structure and can lead to damage of the weakest components (e.g. gearboxes and loadcells) and, over time, to fractures for fatigue.

Based on these motivations, the work of this thesis will deal with the development of methodologies to analyze (and ultimately address) the above-mentioned control limitations. Moreover it will be presented the design of different types of feet, to mitigate the effects of the ground impacts which have frequencies out of the bandwidth of the controller.

1.2 Contributions

The original contributions presented in this thesis, represent material from already published papers and from an unpublished one and can be grouped in four topics: (1) torque control, (2) impedance control, (3) passivity and (4) passive compliance as listed below:

- **Torque control: velocity compensation.** I propose a compensation for the natural load velocity feedback in order to make the torque dynamics independent from the load dynamics. This can be accomplished by a positive feedback compensation (*velocity compensation*) that eliminates the intrinsic bandwidth limitation in torque control that arises when the load is free to move. My contribution is to generalize the concept of velocity compensation to different actuation technologies, justifying it with appropriate theoretical tools (Section 3.4.1). The effect of the compensation is to move the system poles in order to eliminate or strongly reduce the detrimental effect of the zero that is limiting the bandwidth (Section 3.6). The result after the compensation is a system that is easier to control without the torque bandwidth limitations due to the zero. This enables good

1. INTRODUCTION

control performance (high torque bandwidth) by using well-established and less sophisticated controller structures like a P, PI or PID. In particular, I will show that keeping the torque controller gains constant, the bandwidth can be increased only by using velocity compensation. Despite the idea behind velocity compensation has been used in the past, a general framework and an extensive analysis of its influence on control performances (also when an outer loop is considered) is still missing in the literature.

- **Impedance control: stability regions for one joint.** Another contribution of this thesis is a methodology to investigate and rigorously characterize the limitations present in the real implementation of the impedance control. This is very important to the robotics community because it improves the basic understanding of the issues which constrain the performance of impedance controlled robots in order to be able to define strategies (e.g gain scheduling approaches) to achieve the best performances in any locomotion situation. This is a new and interesting contribution because all the sources of non-ideality are taken into account in a detailed model of the system: actuator dynamics, filters, sampling time and inner loop bandwidth, investigating their influence on the region of stable impedance parameters. The results are shown in a graphical way (stability region) and are useful to minimize laborious, trial-and-error experimentation. In this work I limit my analysis to the hip abduction/adduction (*HAA*) joint of the hydraulic quadruped HyQ which is driven by an electric actuator. Similar results are presented for the hydraulic joints in [Boaventura, 2013]. A more general analysis which involves all the three joints of the leg is part of ongoing work. Finally these studies can also give important insights to improve the design and locomotion of robots.
- **Passivity: analysis for one joint.** The analysis of the passivity of the system is studied in different conditions: with the torque loop alone and with an outer impedance loop closed around it. The analysis of passivity is repeated by varying several parameters (torque loop bandwidth, velocity compensation gain, sampling frequency, filter delay) to show their influence on the passivity. This study shows its importance when the purpose is to design a controller with which the robot remains stable also when enters into contact with the environment.
- **Impedance control: implementation for the whole leg.** The implementation of an end-effector impedance algorithm for the whole robot leg is presented and its effectiveness in shaping the end-effector stiffness is demonstrated through experiments. An end-effector implementation is important because it is defined at the interaction port where locomotion requirements and foot trajectories are usually assigned. Furthermore controlling the

1.3. Outline of the thesis

end-effector impedance makes it independent of the leg configuration. I also discuss on some procedures to quantitatively select the impedance parameters according to locomotion requirements. In particular, a rule of thumb to specify the performances and select the impedance parameters for locomotion is missing in the robotic community.

- **Passive compliance: design of a compliant foot.** The introduction of passive compliant elements in the robot is investigated, with the purpose to reduce the transmission to the robot structure of the peak forces due to ground contact. My contribution is a procedure to select the minimum amount of stiffness at the foot to primarily to cope with this peak forces while still taking advantage of the versatility of impedance control when these forces have a frequency content that is inside the controller bandwidth (Chapter 5). The selection of the passive element is made also in relation to the locomotion requirements. A prototype of a compliant foot has been built for the HyQ leg, which is equipped with a passive spring (*passive foot*).
- **Passive compliance: design of an actively damped compliant foot.** One drawback of introducing a compliant element at the foot is that for certain combination of mass and leg impedance the phenomenon of chattering may occur which results in a momentary loss of traction. Therefore, I evaluated another foot (designed by Esa Kostamo from Aalto university), which is equipped with an actively-controlled damper with the purpose to dissipate the energy stored in the spring after the compression due to an impact. This eliminates or strongly reduces the chance of chattering. The suggested solution makes use of magneto-rheological fluid technology which presents high bandwidth in actively controlling the damping force. This contribution represents a solution to damp the impacts which is novel in legged locomotion.

1.3 Outline of the thesis

This dissertation is divided into seven chapters and is organized as follows:

- **Chapter 2** illustrates the state of the art in legged robots, torque control and impedance control. The literature that covers these areas is vast and we will focus on the concepts that are most related to the arguments of the thesis, with particular focus on recent achievements and results. The chapter concludes with a brief introduction to the HyQ platform.
- **Chapter 3** introduces a mathematical model and the design of the torque controller for the electrical hip abduction/adduction (*HAA*) joint of the HyQ robot. The introduction

1. INTRODUCTION

of the velocity compensation framework and its practical implementation for electric actuators is also described.

- In **Chapter 4** an outer impedance loop is closed around the torque controller developed in the previous chapter, in a nested loop architecture. This is the most important chapter of the thesis. The chapter is divided into parts: the first part introduces the impedance control for a single joint. The analysis of the influence of the inner torque loop bandwidth, filtering and sampling on the region of stable impedance parameters is presented and subsequently a similar analysis is carried out to show also their influence on passivity. Then it is illustrated how the range of frequencies, in which the impedance is effectively tracked, is influenced by the bandwidth of the inner torque loop. In the second part of the chapter an impedance controller is designed for the whole leg both in joint space and in end-effector space. *Pros* and *cons* of the two implementations are discussed.
- **Chapter 5** illustrates a methodology (by simulation) to select the stiffness of the spring to be put in the HyQ foot, to reduce peak forces during locomotion. A prototype of compliant foot is designed based on the results of the above simulation. Experimental results of drop tests with the foot mounted on the real leg are presented to demonstrate the effectiveness of the prototype in reducing the initial peak of the impact.
- **Chapter 6** introduces a novel compliant foot (*MR foot*) where damping is actively controlled by means of magneto-rheological fluids. A control law is designed with the goal to dissipate all the kinetic energy during the first ground contact sequence (compression and extension of the spring). Experimental drop tests with the prototype show the damping performance in terms of bounce reduction. *Pros* and *cons* of the approach are also discussed.
- **Chapter 7** summarizes the main results of the previous chapters extending them with a more general discussion and giving directions for future ongoing research.
- **Appendix A** presents mathematical extensions of the topics presented in Chapter 3.
- **Appendix B** details the mechanical design and experimental evaluation of a six axis foot sensor to measure ground reaction forces. Finally the design of the compliant foot and MR damper prototypes, used for the experiments in Chapters 5 and 6 is presented.

2

Background and related work

THIS chapter will provide an overview on the most relevant contributions in legged robotics, torque control and impedance control, which are the main topics of this thesis.

2.1 Legged robotics

We will present here recent developments in legged robotics of the last decades. For an historical review on legged robotics we suggest the work of [Song and Waldron, 1989]. For a review more focused on quadrupedal locomotion please refer to [Gonzales de Santos et al., 2006].

Robot can be powered with different kind of actuators: pneumatic, hydraulic and electric motors. When actuators are equipped with spring at their outputs they are called *series elastic actuators*. Series elastic actuators can be implemented with high geared electric motors or hydraulic pistons [Pratt, 2002]. The first legged robot robot that is using hydro-elastic actuator is the monopod built by Krupp from Yobotics [Krupp and Pratt, 2006]. An extensive overview on different actuation principles for robotics can be found in [Semini, 2010].

Research on dynamic legged robots had a significant development in the 80s with the seminal work of Marc Raibert who build his first hopping robot (*monopod*) (see Fig. 2.1(left)). The purpose was to help the research community to gain better understanding on the basic principles of legged locomotion. The monopod, later improved in a 3D hopper, was able to hop at a desired velocity, while maintaining balance in face of external disturbances. The actuation of the robot was pneumatic.

Afterwards, a number of quadruped robots with a simple kinematics and a reduced number of active joints, were built based on electric actuation. *Rush* [Estremera and Waldron, 2008] was able to autonomously stabilize on flat terrain. The robot was equipped with springs and was designed to study energy-efficient running locomotion. *Scout II* Poulakakis et al. [2005] (see

2. BACKGROUND AND RELATED WORK

Fig. 2.1(right)), developed at at McGill University, was the first quadruped able to gallop, by using compliant prismatic legs. *Kolt* [Nichol et al., 2004] from Stanford was also constructed to study a quadrupedal gallop gait and understand the primary biological features necessary for galloping. More recent examples are the Tekken series robots [Kong et al., 2009], the EPFL *Cheetah* [Rutishauser et al., 2008]. These quadrupeds were lacking of versatility due to the

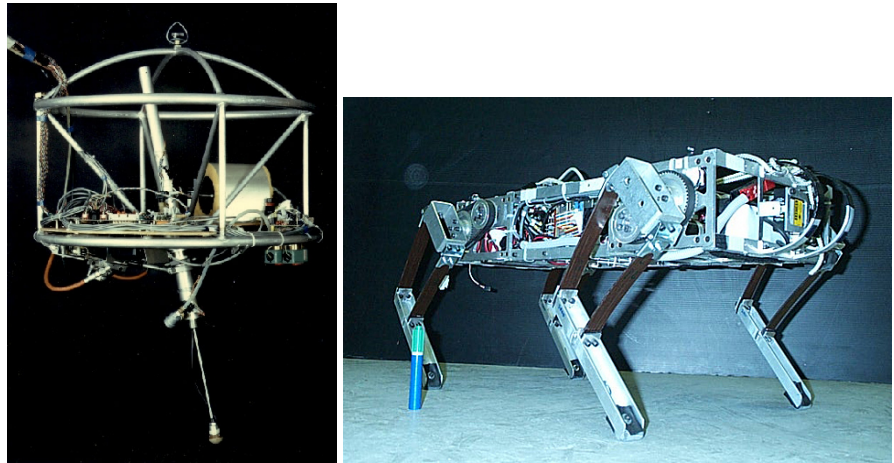


Figure 2.1: Raybert monopod (left) and Scout II (right) robots.

reduced number actuators and the reduced leg workspace.

A step forward in this direction was the design of the *LittleDog* robot [Murphy et al., 2011] (Fig. 2.2(left)), which enabled quasi-static stable walking gait on very rough terrains [Buchli et al., 2009a] using position controlled joints and high geared actuators. The platform was electrically actuated and built for learning studies for locomotion on very rough terrains. However, its performances were dependent on a precise kinematic planning and a perfect knowledge of the terrain it was traversing. This made it unable to negotiate ground that featured unknown irregularities. Moreover, the absence of a torque controller at the joint resulted in high impact forces at the feet which frequently lead to failure of the joint bearings when dynamic gaits were implemented. This issue was motivating the community to moving toward design of robots with lower joint stiffness.

Electric actuators are very popular because of their size and price, ease of use and accuracy of control. However their main drawback, the low power density, soon became evident with dynamic motions and made researchers resort to mechanical energy storage elements (springs). Apart from being able to better deal with impacts, the goal was to use springs to reduce energy consumption by trying to exploit as much as possible the natural dynamics of the robot, while reducing the positive work made by the actuators. This opened also a wide field of research on passively dynamic walking [McGeer, 1990]. In particular has been shown that biped robot can

2.1. Legged robotics

exhibit periodic and stable limit cycle while passively walking [Goswami et al., 1996]. Despite this are valuable research results, passively walking robots are of limited applicability in the world outside the laboratory.

For the above reasons, recently, several legged robots have been equipped with series elastic actuators (SEA). The purpose was to protect the actuator and gearbox from unforeseen collisions as well as periodically storing energy [Alexander, 1990] and increase efficiency of the locomotion [Cavagna et al., 1964]. Taking inspiration from the Meka robotics arm [Meka robotics, 2011], an example of legged robot equipped with SEA is the biped *Hume* which is bipedal robot designed to traverse rough terrains.

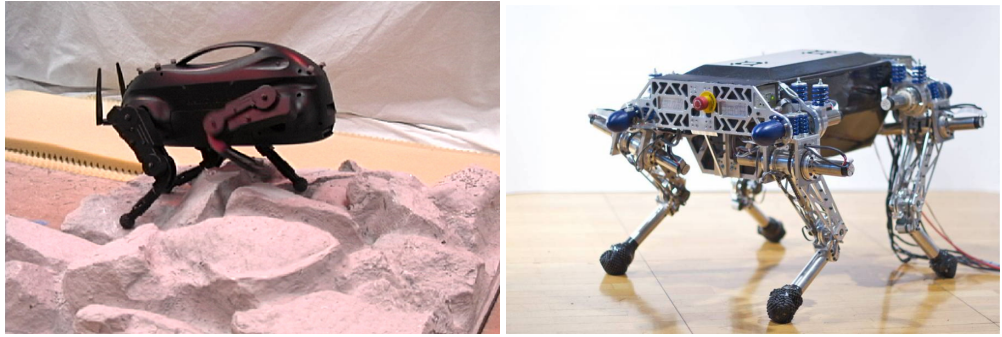


Figure 2.2: Little Dog (left) and StarlETH (right) robots.

Similarly, *StarlETH* [Hutter et al., 2012] (see Fig. 2.2 (right)) is a compliant quadruped robot which represents a step forward in terms of versatility whose legs are torque controlled during the stance phase and position controlled during the swing phase. StarlETH showed locomotion capabilities in walking, trotting and walking on a stem tree, we can mention other robots with some passive compliant elements in the joints like the humanoid *Coman* from IIT [Tsagarakis et al., 2013] and the biped *Mabel* [Grizzle et al., 2009]. Again, all these robots are powered with electric actuators which reach their power limits when the weight/inertia/size of the robot increases or very dynamic movements are commanded. In fact high speed legged locomotion requires high accelerations and loading of the robots legs. Several solutions to enhance the power capabilities of electric actuators were investigated by Seok [Seok et al., 2012], who designed a high torque density actuator with high back-drivability. An optimal trade-off was found between reducing the actuator inertia and increasing torque density by playing with the motor gap radius and the gear ratio. Moreover he showed that by appropriate over-votaging techniques, the motor can generate much higher power than the one specified in manufacturer datasheet which is rated for nominal voltage. Indeed power limits are given by the coils heating which is proportional to current. Usually robots need to produce torques higher than the continuous operating torque limit, only for a short period of time, because the torque

2. BACKGROUND AND RELATED WORK

profile is strongly discontinuous in locomotion. Therefore, provided that the temperature does not exceed the limits, the supply voltage can be increased, thus increasing significantly the deliverable power.

In term of actuating technologies Raibert and his lab at the MIT and later at Boston Dynamics set a milestone for recent developments of legged robots, by opening a new line of research on highly dynamic hydraulically actuated robot. Thanks to the higher power density of the hydraulics actuators and to the torque control implemented on all joints, astonishing performances in terms of versatility and highly dynamic motion were achieved by the quadruped robot *BigDog* ([Buehler et al., 2005], [Raibert et al., 2008]). The Cheetah [Boston Dynamics Corp., 2012] robot (see Fig. 2.3) achieved a very fast running was on a treadmill.

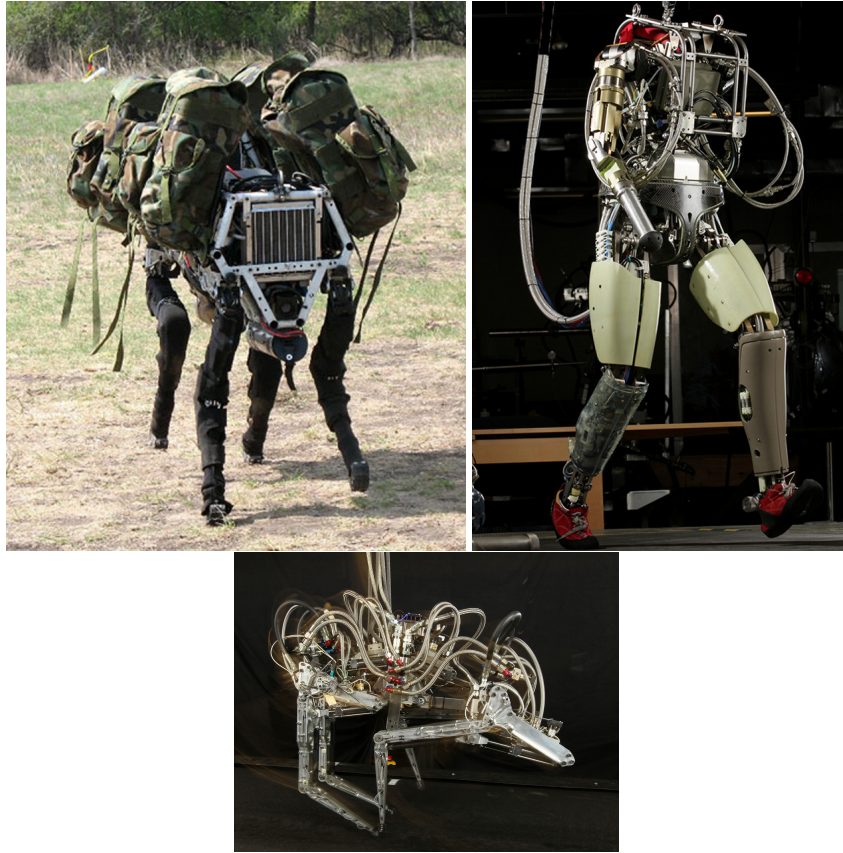


Figure 2.3: BigDog (left), Petman (right) and Cheetah (bottom), by Boston Dynamics

Much of the success of these examples of legged robots was due to their actuation system performance. Indeed hydraulic actuators have a wider dynamic range, are more powerful than pneumatic actuators, have an excellent power-to-weight ratio and high bandwidth [Semenini et al., 2011c]. Some problems of hydraulic actuation is that it can be bulky and a tether

2.1. Legged robotics

is generally needed to supply the oil in pressure to the robot, coming from an external pump. These problems have been addressed by an effective design of a lightweight and compact on-board hydraulic power supply, which made *BigDog* completely autonomous. However one of the main issue in current hydraulic actuators is their high energy inefficiency. For instance the leakage flow in every *BigDog* valve is about 0.35 l/min [Semini, 2010]. This is a consequence of having high performance critically-lapped valves. Such high leakage flow it means a significant power loss that substantially increase the cost of transportation (COT) [Kuo, 2007] in comparison with the one of some electrically driven robots or with animals. Boston Dynamics research is not only limited to quadrupeds and recently a biped called Petman [Boston Dynamics Corp., 2011] has been developed. Petman is able to balance while successfully climbing stairs or closely resembling natural human motion while walking on a treadmill. Unfortunately information on the development of all Boston Dynamics robots is not publicly available.

Other hydraulic robots which implement torque control are the humanoids built by Sarcos ltd (DB,CB) [Cheng et al., 2007]. These robot are used to study human behaviour, including active balance and dynamic full body motions. In 2009 Sarcos presented also an impressive hydraulic exoskeleton (not published) [Raytheon Sarcos, 2010] designed to help soldiers to perform repetitive tasks that can lead to injuries (e.g. heavy lifting).

From the control point of view legged robots can be classified in term of whole body stability: statically stable robots and dynamically stable robots. To the first category belong the robots that during the motion keep the projection of the CoG inside the support polygon (e.g Titan IV [Hirose et al., 2009]). The main feature of a statically stable robot is that it can stand still without falling over. This approach is very safe, but it is also very slow and energy inefficient. The alternative to static stability is dynamic stability, which allows a robot (or animal) to be stable while moving. This means that the robot can be stable as soon as keeps moving but it cannot stop in any moment and stay standing. If the goal is to achieve dynamic locomotion, dynamic stability is not just an option but mandatory. Depending if the dynamic balance is achieved within a single or multiple steps we can have different approaches. In the first case we have ZMP-based (Vukobratovic and Borovac [2004]) algorithms. ZMP algorithms compute a reference trajectory for the CoG to obtain dynamically balanced feasible trajectory when walking (e.g. *Asimo* robot [Bin Hammam et al., 2010]). Dynamic stability can also be achieved by taking one or more steps. In this case foot placement algorithms like *capture point* [Pratt et al., 2006], [Koolen et al., 2012]) compute foot positions where robot must take a step to avoid a fall and keep dynamic stability also in face of external disturbances. The foot location is computed by using simple linearized models (e.g linear inverted pendulum [Kajita et al., 2001]) which are a simple approximation to the robot dynamics

2. BACKGROUND AND RELATED WORK

2.2 Torque control

Robots are often modeled as rigid body systems. Physical causality prescribes that a rigid body inertia has a force as input and motion as output. Extending the concept to robots, they have torques as input to their link dynamics. This motivated us to implement a high-fidelity low-level torque control at the joints.

Another advantage of torque control is that enables to straightforwardly implement different kind of controllers, like rigid body dynamics model-based control (e.g. inverse dynamics [Buchli et al., 2009b],[Mistry et al., 2010] and gravity compensation) virtual model control [Pratt et al., 2001] as well as impedance control (Hogan [1985]; Kazerooni et al. [1986]) or operational space control [Khatib, 1987]. Torque control simplifies also the implementation of biomechanic templates like the spring loaded inverted pendulum (*SLIP*) [Blickhan, 1989]. This is a template, widely accepted in the robotics community, to describe the COG motion and ground reaction forces (GRF) in human and animal gaits [Geyer et al., 2006]. Finally, since a legged robot is also subjected to force inputs coming from the ground, a low-level torque control ease significantly the implementation of posture controllers to effectively redistribute feet contact forces in order to improve balancing. This is of great importance to achieve robust locomotion on unstructured terrains.

Research on robot torque/force control dates back to the 50s with industrial manipulators. Torque control was initially developed to eliminate the undesirable effects of non-linearities and friction inherent in the actuators, generally found in industrial robots [Zinn et al., 2004]. However stability issues emerged immediately due to the stiff mechanical interfaces between the actuator and its load [Whitney, 1985]. As a matter of facts, consider the case of having just a very stiff load cell between the actuator and a rigid load to measure the force. Even a slight movement will generate extremely large force readings in the load cell. This means that the open-loop gain of the actuator is very high [An and Hollerbach, 1987]. Therefore whenever contacting with stiff environments, due to the presence of unmodeled dynamics, using a high-gain feedback controller would very likely result in chatter between the actuator and the load [An, 1986]. A high joint damping would help to maintain stability in contact conditions but this on the other hand would lead to unacceptably slow performances.

To overcome these issues a solution was to reduce the transmission stiffness, initially using flexible sensor and afterwards deliberately introducing springs in series with the actuator. This is the idea behind (*series elastic actuators* (SEA)[Pratt and Williamson, 1995]). In this case the load force can be measured through the deflection of the spring without the necessity to equip the robot with expensive torque sensors (force/torque problem is turned into a position control problem). In particular a "soft" element to measure the torque is good for small torque resolu-

tion. The introduction of springs helps to reduce large impact forces and better handle shocks from the environment because of the output impedance is inherently reduced. However this is a drawback for the control performance because the overall system bandwidth is reduced in comparison to rigidly actuated devices [Eppinger and Seering, 1987]. Although these issues were studied since the 50s, more recently Eppinger showed [Eppinger and Seering, 1992] that the dynamic characteristics of the robot (actuator and rigid body dynamics) contributes significantly to limit the closed-loop torque/force performance, making the closed-loop system unstable for high gains. Also the mutual collocation of the sensor and actuator has an impact. If the spring is within the actuator and the sensor dynamically non collocated flexible modes are present that come with more poles than zeros and represent a performance limitation for conventional PD controllers [Eppinger and Seering, 1992]. In particular high bandwidth is difficult to achieve because the flexible modes of the compliant system introduce a phase delay above the first mode frequency. As a consequence attenuation of flexible mode oscillations excited by disturbances can be difficult to achieve [Zinn et al., 2004]. Approaches such as Distributed Macro Micro (DM2)[Zinn et al., 2004] can overcome this trade-off at the cost of doubling the actuation and sensing requirements and so complexity. Moreover since the torque is controlled by the actuator position that deflects the spring, the maximum speed of the electric motor is also a limiting factor of the torque bandwidth in a robot equipped with SEA.

Another drawback of SEAs is that the amount of passive stiffness is fixed and not adjustable to the task at hand. This limits significantly the versatility of the robot. Indeed the possibility to change the leg stiffness is a desirable feature in legged robotics applications because it enables to change the dynamics of the robot during the locomotion. In fact biological experiments showed that animals change their leg stiffness according to the surface they are traversing [Ferris et al., 1998a]. A possible solution is to use variable stiffness actuators (VSA) [Ham et al., 2009], [Walker and Niemeyer, 2010]. However, despite VSA seem to be a promising solution for fixed base manipulators, some aspects like weight, and velocity saturation limit their applicability to legged robots. A nice design of torque controlled robot is the DLR lightweight arm [Hirzinger et al., 2001] (see Fig. 2.4). In this design torque sensors embedded in high performance actuators gave to the robot excellent torque performance.

Another important limiting factor to the torque bandwidth, when torque is transmitted from the actuator to a moving load through a transmission with finite stiffness (e.g. gearbox, hydraulic oil, spring), is that an intrinsic load velocity feedback exists in the force dynamics, which does not depend on the actuator. This introduces a zero in the torque transfer function that depends on the load dynamics (damping and inertia) and can limit the achievable closed-loop torque bandwidth. An important model-based control, called *velocity compensation*, consists in compensating for this physical load velocity feedback [Boaventura et al.,

2. BACKGROUND AND RELATED WORK

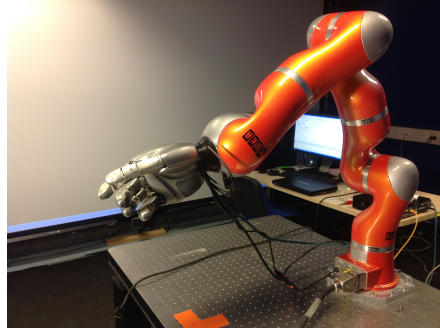


Figure 2.4: DLR lightweight arm.

2012a]. Canceling out the influence of the zero on the force dynamics is the main purpose of the load velocity compensation. With this zero/pole cancellation, it is possible to increase the controller gains without making the system unstable and thus achieve the desired torque bandwidth. The concept of load velocity compensation was originally implemented for hydraulic actuators in [Conrad and Jensen, 1987], where it is shown that force control has poor performances without velocity feedforward or full state feedback. The influence of the load motion is shown for a hydraulic actuator in [Dyke et al., 1995]. The authors called this concept *natural velocity feedback*. A solution to negate the natural velocity feedback of the actuator was proposed in Dimig et al. [1999]. Previous works addressed the compensation of the load motion for electrical drives as well. Hori et al [Hori et al., 1994] implemented disturbance observers to compensate for the effect of the load torque by feeding back the motor velocity signal. State feedback gains were found by pole placement techniques. Dhaouadi et al [Dhaouadi et al., 1993] designed a speed controller based on a torque observer to increase the phase margin at the resonant frequency and to reduce the limit cycles resulting from the gear backlash. Kaneko et al [Kaneko et al., 1991] attained similar results designing an acceleration controller and using positive feedbacks from torque and load position. This suppressed the effects of both load torque and motor friction, setting a single inertia behavior to the system. More recently Taylor [Taylor, 2011] proposed the use of a velocity loop to increase the overall system bandwidth while reducing the integral term in the PID controller. Another approach [Wyeth, 2006] considers to close a velocity loop motor-side to reduce the effects of backlash and stiction due to the gearbox and achieve higher loop bandwidth. We will show in this work that the concept velocity compensation can be generalized to any mechanical system where force/torque is under control and a compliant element is present, regardless of the type of actuator in use (e.g hydraulic/electric/pneumatic)[Boaventura et al., 2012a].

2.3 Impedance control

Traditionally, robots used to perform repetitive tasks in structured and well-known environments. In these situations position control (or pure force control in case of well defined contact tasks) is the best solution because no contact (or little) with the environment is occurring. In this situation maximizing tracking accuracy inside the workspace is the main control target. Conversely, whenever the robot operates in unstructured environments, where the knowledge of the environment is imprecise or when the motion is constrained (e.g. by the ground in the case of a legged robot), some kind of interaction control is required. In particular the robot must be able to comply with the forces that appear when it enter in contact with the environment.

Interaction forces might be regulated in two ways: with passive methods and with active methods. Passive methods devise the introduction of physical compliant elements between the robot and the environment to limit the interaction forces (e.g a passive spring on a gripper for a peg in a hole placement to accommodate misalignment errors). On the other hand active compliance is achieved through the active control of joints (position or torque) using feedback measurements of joint forces. This can emulate a virtual compliance both at the joint as at the end-effector level. A major benefit of actively control the compliance is its flexibility to change the dynamic characteristics (e.g such as stiffness and damping) on-the-fly. This is a great advantage versus introducing passive compliant/damping elements in the structure which can have only a fixed value of stiffness and damping. Indeed a desired feature is to make legged robots able to change the leg stiffness to adapt to the surface properties [Ferris et al., 1998a]. In the past, the implementation of active compliance control algorithms were limited by the bandwidth of the controller, which was constrained by the computational power and by the actuator dynamics. This limited the control of the compliance to a restricted range of frequency. However, recent technological development, both in computer and acquisition performances, made active compliance feasible also for highly-dynamic applications [Boaventura et al., 2012b].

There are many ways of actively controlling the interaction forces or the compliance: impedance control [Hogan, 1985], operational space control [Khatib, 1987], hybrid force-control [Raibert and Craig, 1981], and virtual model control [Pratt et al., 2001]. A distinction exists between direct and indirect active compliance control methods. Direct force control methods are those where the controller directly regulates the contact force to a desired reference. A classical force control strategy or a hybrid force/motion control belong to this category. Indirect force control methods are those where the force is controlled indirectly via motion control. Impedance control in its different "flavours" belongs to this category [von Jose de Gea Fernandez, 2010]. In particular, impedance control uses a single control law to regulate simultaneously both position and force by specifying a target dynamic relationship (mechanical

2. BACKGROUND AND RELATED WORK

impedance) between them. This dynamic characteristics can be defined at different locations (e.g. joint, end effector, etc). Theoretically, these locations can be any point of the robot given that a kinematic definition is available. Virtual model control, developed by Jerry Pratt, can be broadly related to this concept. Virtual model control framework is an intuitive approach to control robot dynamic behavior during locomotion regardless of the complexity of the system. According to this framework, virtual components such as spring and dampers are placed at strategic locations within the robot or between the robot and the environment [Pratt et al., 2001].

A lot of literature material is available on the control of interaction forces. A review of different control schemes can be found in [von Jose de Gea Fernandez, 2010] and [Zeng and Hemami, 1997] while a book focused exclusively on force control is [Siciliano and Villani, 1999]. Nevertheless, many aspects, often overlooked in the literature, still create stability issues on impedance control. For instance, the range of stable stiffness and dampings that can be virtually created can be strongly limited by filtering [Janabi-Sharifi et al., 2000], sampling frequency, actuator dynamics and also by the bandwidth of inner control loops (e.g. a torque loop). A brief review on the issues that affect the performance of force controlled robots can be found in [Hogan and Colgate, 1989]. Lawrence in [Lawrence, 1988] considers the non-ideal, practical effects of computation and communication delays on impedance control and find some stability boundaries. However he carried out his analysis in continuous time and it is not necessarily valid for discrete time systems. Indeed sampling is not completely equivalent to time delays because when sampling there are additional zeros that do not appear in continuous time. In [Lawrence, 1989] the analysis is extended from SISO to multiple degree of freedom manipulators considering also the non linear effect of torque/speed saturation in the actuator. However, An extensive quantitative analysis of all the aspects that influence the impedance stability regions is still missing in the research community and this will be the main core of this thesis.

2.4 Passivity

Besides the nominal stability an additional specification is necessary for a robot which is interacting with the environment: this is called *coupled stability*. Indeed a robot that is stable can become unstable whenever enters in contact with an environment that has certain dynamic properties (e.g certain combinations of stiffness and damping). In fact, whenever the robot is in contact with the environment, the dynamic of the whole system is depending both on the dynamics of the robot and of the environment. Since the environment is usually considered as a passive, a practical solution to ensure closed-loop stability during the interaction, is to design

the controller such that the robot system behaves passively at the interaction port. This ensures a stable interaction with any kind of environmental stiffness and damping. Colgate [Colgate, 1986] was a pioneer in defining and investigating passivity for mechanical systems. Using a Nyquist stability analysis, Colgate and Hogan [Colgate and Hogan, 1988] have derived the necessary and sufficient conditions for stability in contact with arbitrary passive objects. Motivated by the necessity to preserve stability in robots when interacting with humans (haptic interfaces), analytical necessary and sufficient conditions for passivity were found in [Colgate and Schenkel, 1997]. However this analytical passivity criterion is of limited applicability because it is only valid for a 1 degree-of-freedom (DOF) haptic interface. A more general analysis with a discrete time implementation of the controller is presented in [Colgate, 1994] for a two-link manipulator introducing the concept of *multi-port coupled stability*. In [Vallery et al., 2007] several control schemes for series elastic actuators are investigated with respect to passivity issues. Passivity-based controllers have been recently implemented on articulated robotics arms [Albu-Schäffer et al., 2007]. As happens for the nominal stability, passivity is also influenced by filtering and sampling delay as well as by the inner loop torque bandwidth. Some work has been done recently on this topic by [Mosadeghzad et al., 2012] which compares how passivity property is preserved in a robotic joint when impedance control is implemented with different nested inner loops (namely velocity, position and torque).

2.5 Passive compliance

Traditionally passive compliant elements are introduced in legged robotics to reduce energy consumption and protect the weaker components. The first motivation is given by biomechanics research that demonstrated that springs and running are intimately related. For instance in animals, during the stance phase, the energy is initially stored in elastic elements such as tendons or muscle fibers. Then, this energy is released during knee extension, pushing the body upward and forward at the lift off. The introduction of springs can help legged robots to store impact energy and use it for locomotion, thus reducing the positive work made by the actuators.

The other use of springs is related to their decoupling effect that is beneficial to reduce the peak forces (due to ground impacts) that can be transmitted to the mechanical structures [Carrella, 2011]. Peak forces are due to the fact that the bandwidth limitation in the impedance controller creates difficulties in dealing with impact forces and abrupt contacts with the environment. At this respect a certain amount of passive compliance is beneficial to filter these peaks that would lead over time to damage of the weakest components (e.g. gearboxes and loadcells). However, the flexibility introduced into the structure also constitutes a limiting factor to the tracking of the foot trajectory because it creates positioning error due to the spring

2. BACKGROUND AND RELATED WORK

compression. Therefore it is of great importance to select just the minimum amount of compliance to fulfill the desired requirements of force transmission reduction. Some indications on how to select the value of the passive spring for a hopping robot are given in [Alexander, 1990]. In particular a design rule is obtained using a simplified bouncing model.

Another shortcoming of introducing springs (e.g at the feet) is that not only a steady state error but also an additional dynamics is introduced in the system that may induce unwanted oscillations. Depending on the relationships between the robot mass, the leg impedance and the actual value of the selected spring, an impact may result in bouncing/chattering with a momentary loss of grip [Alexander, 1990]. Traditionally, different strategies are adopted to reduce chattering; they involve the introduction of a certain amount of damping together with the spring [Ganguli, 2005]. The aim is to dissipate the energy stored in the spring which may induce undesired bouncing.

In principle this can be achieved using a passive damping element. However a passive damper would perform well only when the system has a well-defined dynamics. This is not the case of a legged robot, because the robot inertia reflected at the foot can be very different depending on robot orientation and joint configuration. Being able to vary the damping coefficient endows the system with more advantages and makes the system more versatile. Indeed, if the damping force is controllable, different control laws can be implemented to remove the energy stored in the spring. A well-established technology in the automotive field [Fischer and Isermann, 2004] is to actively control the damping by using magneto-rheological (MR) fluids, because of their inherent high bandwidth. An example of using MR active-dampers in robotics is presented in [Chew et al., 2004] where Chew et al. proposed a concept of series damper actuator (SDA) built for torque control purposes. In their study the experimental setup consisted of an electric motor and rotational magnetorheological damper (Lord MRB-2107-3). The advantage is that the damping coefficient of the system can be continuously controlled to enable high torque fidelity at both high and low torque ranges. Herr [Herr and Wilkenfeld, 2003] successfully implemented MR technologies in prosthetic devices with the purpose to automatically adapt the damping in the knee, to the gait of the amputee. More recently Walker [Walker et al., 2009] implemented an MR based clutch located in series to the actuator to adjust in real-time the output impedance with the purpose to improve safety in interaction with humans.

2.6 HyQ platform description

The experimental platform used for the project is the quadruped robot HyQ [Semini et al., 2011c] (Fig.2.5 (left)). HyQ is a new versatile hydraulically powered quadruped robot that has been developed to serve as a platform to study not only highly dynamic motions, such as

2.6. HyQ platform description

running and jumping, but also careful navigation over very rough terrain.

The robot is equipped with 12 active degrees of freedom (*DOF*). Each leg has three *DOF*, which is the minimum required to allow a foot positioning in a three-dimensional workspace (Fig.2.5 (right)). HyQ is equipped with different types of actuators. The hip abduc-

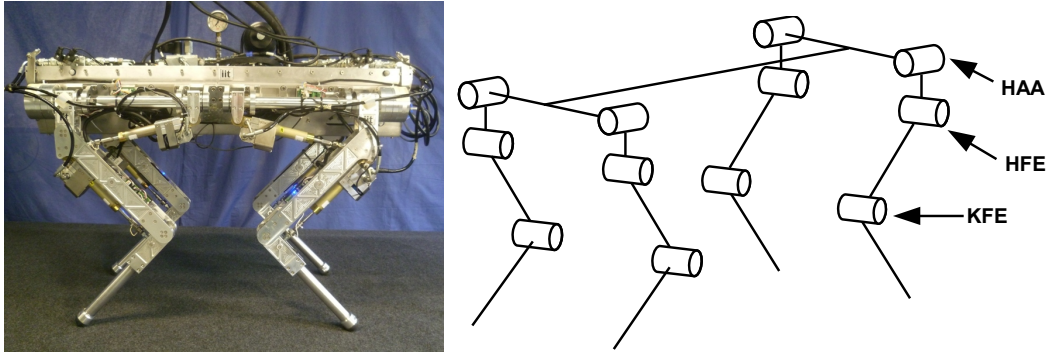


Figure 2.5: HyQ: Hydraulic Quadruped robot. Picture of the robot (left). Sketch with labels of the kinematic tree of the robot (right). Each leg has three leg joints, hip abduction/adduction (*HAA*), hip flexion/extension (*HFE*) and knee flexion/extension (*KFE*)

tion/adduction (*HAA*) joints are driven by brushless DC electric motors and connect the legs to the robot torso, creating the lateral leg motion. The hip and knee flexion/extension (*HFE* and *KFE*, respectively) are actuated by linear hydraulic cylinders, which are driven by high performance servo-valves (bandwidth around 250Hz) [MOOG Inc., 2003]. Load-cells, located at the piston rod ends, measure the forces of the pistons. By kinematic transformations, considering the lever arm between the piston attachment point and the joint axes, the joint torques are obtained. Similarly, a custom torque sensor, embedded in the *HAA* joint, provides a direct measurement of the torque.

Having different actuator types was a consequence of the different requirements that exist for the joints of the HyQ leg. In particular, hydraulic actuation which has a high power-to-weight ratio, has been chosen for the *HFE* and *KFE* joints which must provide high speed and torque during fast locomotion modes. This gives the robot the capability to perform powerful and dynamic motions that would be hard to achieve with more traditional electric actuators. Furthermore, the intrinsic compliance of hydraulic hoses and oil can help to partially absorb shocks. The *HAA* joint, on the other hand, needs to be more compact than the relatively long hydraulic cylinders. Moreover, power requirements are usually lower for the abduction-adduction joints thus justifying the choice of electric actuation which has lower power density but it can be embedded in a more compact arrangement.

In detail a DC brush-less motor with a gearbox has been selected to achieve a maximum torque output of 80 Nm [Emoteq Inc., 1998]. Position sensing is performed by absolute and

2. BACKGROUND AND RELATED WORK

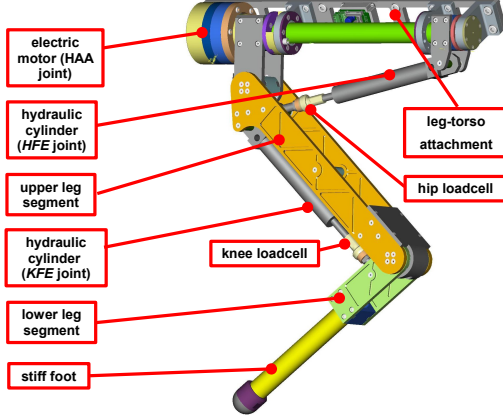


Figure 2.6: CAD view of the HyQ left front leg. The labels show the different components of the actuators and of the mechanical structure.

relative encoders on each joint. A CAD view of the left-front (*LF*) leg is shown in Fig. 2.6 where the location of the main components of the actuators and of the mechanical structure are indicated. The characteristics and features of the HyQ robot are summarized in Table 2.1. The right column lists the purpose of each feature. Further details of the robot design and selection of the actuator types can be found in [Semini, 2010] and [Semini et al., 2011c].

For the sake of simplicity, in this thesis, the tests on actuators and sensors, that do not need to be performed on the whole robot are done on a simpler test rig made of a single *LF* leg mounted on a vertical slider. The HyQ leg can be equipped with a stiff foot or with a compliant foot. The stiff foot consists just in a rigid connection between the foot tip and the lower-leg link (see Fig. 2.6) while the compliant foot has a *compliant* spring between them. This introduces an additional prismatic joint (foot compression/extension *FCE*) in the leg kinematics. Figure 2.7 shows the standard definitions for the joints variables for the left-front leg, with and without the passive compliant foot.

2.6. HyQ platform description

Table 2.1: HyQ specifications

Specifications/features		Purpose/comments
Dimensions (LxWxH) [m]	1m x 0.5m x 1m	-
Weight [kg]	65kg, 100kg	offboard/onboard pump
Degrees of freedom	12	Each leg can reach any 3D point in its workspace
Joint range of motion [deg]	120 for all the joints	A large foot workspace increases the robot's speed and number of foot holds on rough terrain
Joint torque [Nm]	145 (hydr.), 80 Nm (elec.)	High torque for strong and fast motions
Joint speed [rad/s]	12 (hydr.) , 1.2 (elec.)	High joint speed improves balancing and dynamic performance of robot
Sensors of each joint	Absolute and relative encoders, force/torque sensor (strain gauges)	Joint initialization without homing, accurate/fast joint control in position and torque
Sensors at each foot	3 axis force sensor	Measurement of ground reaction forces
Sensors on the torso	Inertial measurement unit (IMU)	Robot balance, state estimation
	3D laser range sensor (360°) and stereo camera	Map creation and robot localization, path planning, obstacle avoidance
Materials	Aluminium alloy (ERGAL) and stainless steel	Light-weight and robust construction
Onboard computing	2 Pentium computer	One for low-level real time joint control and one for vision and high-level planning and control
Control loop frequency [kHz]	1 (Linux Xenomai real time)	For precise, reliable and stable control

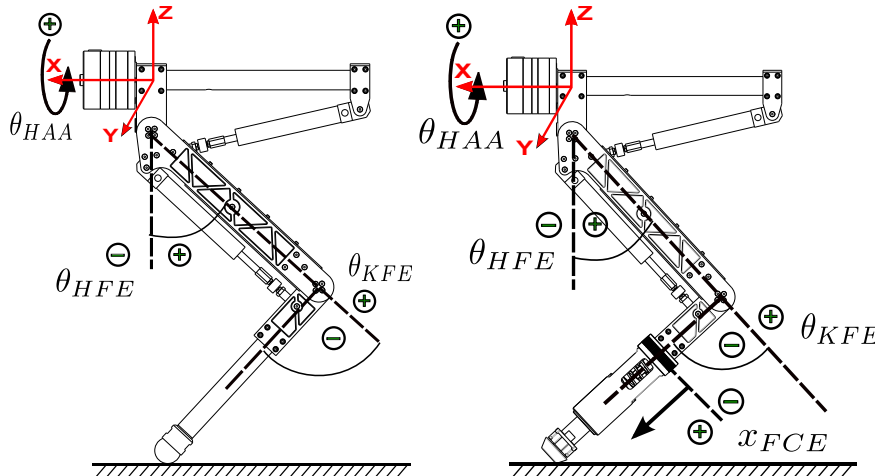


Figure 2.7: Standard definitions for the joint position and positive directions of the left-front leg with the stiff foot (left) and the compliant foot (right).

2. BACKGROUND AND RELATED WORK

3

Improved torque control of electric actuators

IN this chapter we will investigate the torque controller formulation and implementation for the electrical adduction/abduction *HAA* joint. Part of this material has already been presented in [Focchi et al., 2012]. This complements the work presented in [Boaventura, 2013], in which the torque controller for the hydraulic joints *HFE*, *KFE* is described. This torque control loop will be included in a nested loop architecture with an outer impedance loop as described in detail in Chapter 4. In the first part, an accurate model of the system is presented. The *velocity compensation* framework is introduced with the goal to increase the bandwidth of the torque loop without the need of a complex controller structure. Finally, a torque controller is designed based on the insight gained by the model of the system. The issue of the torque ripple due to the use of a harmonic drive gearbox is also addressed by designing an additional lead-lag compensator based on the idea of a notch filter.

3.1 Motivations

Torque control in electric motors can be performed in different ways. The most common one is to measure the motor current. Knowing the relation between torque and current, the torque that the motor is applying to the load can be estimated. This approach is mostly followed for its simplicity because it does not require modifications in the actuator (a simple current sensor must be added to the motor-driver board). The estimation of the load torque obtained with this approach, includes the motor viscous friction/stiction which is not part of the torque which is transmitted to the load. In fact friction can be very large when a gearbox is used, leading to an over or under-estimation of the load torque.

3. IMPROVED TORQUE CONTROL OF ELECTRIC ACTUATORS

A possible solution, is to use a friction identification technique [Murakami et al., 1993] or disturbance observers [Ohnishi et al., 1996]. Alternatively a torque sensor, which directly measures the torque applied to the load, can be used to close the loop. This measurement will include friction in the load but will not include the friction in the motor. In this case a feedback controller calculates the error between the measured torque and the desired one and applies an appropriate voltage to the motor to correct the tracking error. Closing the loop directly on the variable that we want to control (load torque) has the purpose to decrease the effects of friction and inertia, thereby attaining a higher torque fidelity than with current control alone [Robinson, 2000]. For this reason we decided to outfit the robot with torque/force sensors on all the joints.

Regarding the *HAA* joint, since an electric motor in a direct drive fashion was not sufficient to fulfill the torque requirement for locomotion, gear reductions were necessary to amplify the motor torques. Due to the gearbox transmission, a small compliance is introduced in the system. It is worth to point out that besides gearboxes, also couplings, shafts, bearings and many other components used in the assembly of drive trains introduce compliance in the actuator. From a control point of view, even a small compliance like the one introduced by the gearbox introduces complexity in the system if high performance control is desired. Indeed this compliance introduces high frequency mechanical resonances that might pose limitations on stability if they are not taken into account in the controller design. Thus, an accurate model of the system is crucial for the synthesis of the torque controller.

3.2 System description

The electric joint actuator of the HyQ robot consists of a DC brush-less motor (Emoteq HT2301) [Emoteq Inc., 1998] and a harmonic drive gearbox (CSD-25-100) [Harmonic Drive Inc., 2009] with gear ratio 100 : 1. As shown in Fig. 3.1, a frame-less brush-less motor consisting of stator and rotor is inserted into a custom-made motor frame, which is mounted to the robot torso (see Fig. 2.6).

The electric rotor is solidly connected to the harmonic gear train that creates the motion of the *HAA* joint. Link position and load torque are measured by an encoders and a torque sensor that are both located link-side after the gearbox. The torque sensor is custom made, designed to measure torques up to 150 Nm. We use a high resolution (80000 counts/rev) relative encoder (Avago AEDA3300 BE1) to reduce quantization errors in the link velocity computation. An absolute encoder sets the initial position at the robot start-up.

3.3. Model with two inertias

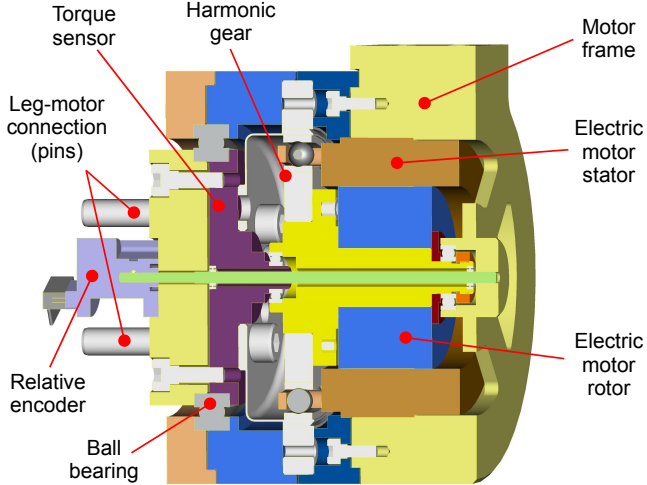


Figure 3.1: Cross-section of the mechanical assembly of the electric *HAA* joint.

3.3 Model with two inertias

This type of assembly is modelled by two second order differential equations coupled via the gearbox transmission flexibility [Hori et al., 1994]. Namely, this flexibility defines the rotational transmission stiffness K_{te} between the rotor and the load (Fig. 3.2(left)). To perform the identification of the physical parameters in the model, a rigid bar of inertia J_l has been attached to the gearbox output (Fig. 3.2(right)). In this case the load can be represented as a single lumped rotational inertia. The equations that describe the load and electrical motor dynamics are the following [Kaneko et al., 1991]:

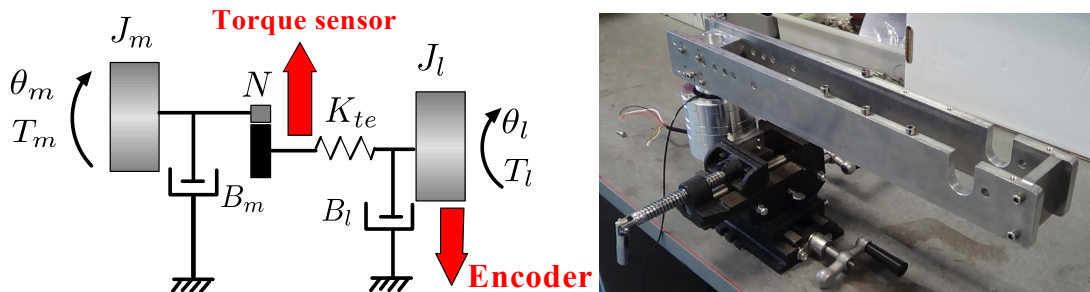


Figure 3.2: Schematic of the model with two inertia for the motor drive system with simple torsional load (left). The rigid bar used for the identification is modelled as a lumped rotational inertia (right).

3. IMPROVED TORQUE CONTROL OF ELECTRIC ACTUATORS

$$\begin{aligned}
J_m \ddot{\theta}_m + B_m \dot{\theta}_m + \frac{K_{te}}{N} \left(\frac{\theta_m}{N} - \theta_l \right) &= k_t I_m \\
J_l \ddot{\theta}_l + B_l \dot{\theta}_l - K_{te} \left(\frac{\theta_m}{N} - \theta_l \right) &= 0 \\
I_m &= \frac{V_m - k_w \dot{\theta}_m}{R} \\
T_l &= K_{te} \left(\frac{\theta_m}{N} - \theta_l \right)
\end{aligned} \tag{3.1}$$

where θ_m and θ_l are the angular positions of the rotor and load, respectively. J_m is the electric rotor inertia, B_m the damping coefficient which includes both rotor and gearbox viscous friction, J_l and B_l load with inertia and damping, I_m is the motor current, N is the gear ratio, V_m is the input voltage. k_t and k_w are the torque-current and back-emf motor constants, respectively and R is the motor coil resistance. The electrical dynamics is neglected (for now), therefore the current is obtained from voltage by a simple algebraic equation. For the identification tests, the link is located on horizontal plane to eliminate the effect of gravity (Fig.3.2(right)). The link is free to move in the air. In fact, the system behavior is significantly different if the joint is constrained or unconstrained. The system is then driven in open loop by a voltage input signal. This signal must be rich enough to excite the relevant mechanical resonances and have enough amplitude to overcome stiction. We choose a sinusoidal chirp signal with 20V amplitude (nominal voltage is 24V) and frequency ranging from 0 to 60Hz. The identified parameters are presented in Table 3.1.

Table 3.1: Identified parameters for the model with two inertias

Name	Description	Value	Origin
$J_l [kgm^2]$	Link inertia	0.198	CAD
$J_m [kgm^2]$	Rotor + gearbox inertia	$5.72 \cdot 10^{-5}$	Datasheet
$B_l [Nms/rad]$	Visc. friction link side	1.008	Identified
$B_m [Nms/rad]$	Visc. friction rotor	0.0015	Identified
$K_{te} [Nm/rad]$	Gearbox stiffness	$8.0769 \cdot 10^3$	Identified
$L [H]$	Coil inductance	$2.02 \cdot 10^{-3}$	Datasheet
$R [\Omega]$	Coil resistance	3.32	Datasheet
$k_t [Nm/A]$	Motor torque constant	0.19	Datasheet
$k_w [Nms/rad]$	Motor speed constant	0.19	Datasheet
N	Gear ratio	100	Datasheet

3.4 Inherent limitations of the torque bandwidth

One difficulty in the design of the torque loop controller is that the load dynamics may introduce severe limitations in the closed loop performance of the torque loop. This problem has been largely overlooked since in many cases the load dynamics are ignored in the analysis [Williamson, 1995], [Pratt et al., 1997]. This may, however, pose limitations to the achievable torque/force bandwidth. The cause of this limitation is the presence of the intrinsic (*natural*) load velocity feedback that exist in the torque dynamics (3.9), which does not depend on the actuator. This natural feedback has been shown for a hydraulic actuator in [Dyke et al., 1995], but in a previous work ([Boaventura et al., 2012a]) we demonstrated that this is not strictly related to a specific actuation technology. Let us express the system transfer function where the output is the torque signal T_l and the voltage V_m is the controllable input. The block diagram of the system is shown in Fig. 3.3. According to (3.1), the torque T_l that is transmitted to the

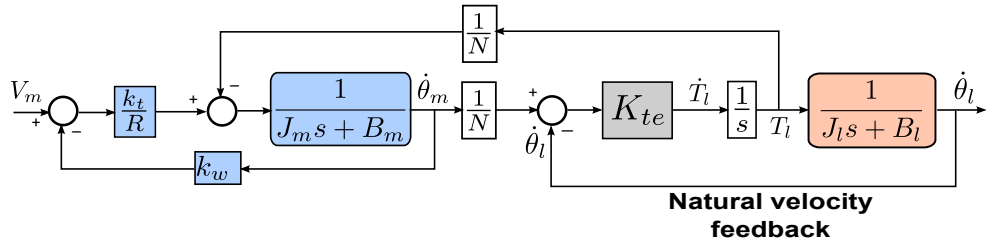


Figure 3.3: Block diagram for an electric motor driving a load. The natural feedback from the load velocity is indicated.

load is:

$$T_l = K_{te} \left(\frac{\theta_m}{N} - \theta_l \right) \quad (3.2)$$

Therefore, performing the Laplace transform, and manipulating (3.1), the following transfer function from the input voltage to the load torque can be obtained:

$$G_t(s) = \frac{T_l}{V_m} = \frac{k_t K_{te} (J_l s + B_l) N}{(J_l s^2 + B_l s + K_{te}) N^2 (R (J_m s + B_m) + k_t k_w) + R K_{te} (J_l s + B_l)} \quad (3.3)$$

To exhibit the above-mentioned limitations we should have a look at the numerator of (3.3). Low values of load damping B_l (e.g viscous friction in bearings) introduce a low frequency zero ($s = \frac{B_l}{J_l} = -5.091 \text{ rad/s}$) that is very close to the imaginary axis in continuos time (see Fig.3.4 (left)) or very close to the unit circle in the discrete time.

3. IMPROVED TORQUE CONTROL OF ELECTRIC ACTUATORS

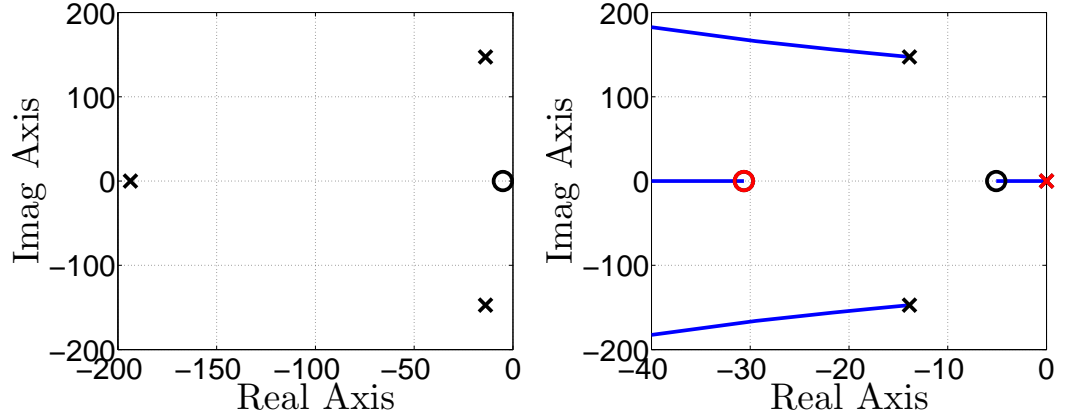


Figure 3.4: Open-loop poles and zero of the torque transfer function $G_t(s)$ (left). Root locus with a PI controller $C_{PI}(s)G_t(s)$ (right). The open loop poles and zero are black while the controller ones are red. The dominant pole introduced by the controller in the origin moves toward the zero with increasing the controller gain P_t , and it cannot be moved to higher frequencies thus limiting the torque bandwidth to the frequency of the zero.

An integrator term in the controller, that eliminates steady state errors, introduces a pole at the origin. Let us consider a simple PI controller:

$$C_{PI} = P_t + \frac{I_t}{s} = P_t \frac{s + \frac{P_t}{I_t}}{s} \quad (3.4)$$

where P_t and I_t are the proportional and integral gains, respectively. This pole introduced by the controller (see Fig.3.4 (right)), will become the dominant pole of the closed loop system. If the controller gain is increased the integrator pole will move towards the zero. To make the response faster, a very large gain will move the pole very close to the zero but in any case the bandwidth is limited by the frequency of the zero because the dominant pole cannot move to higher frequencies.

In general increasing the controller gain a lot is never a good solution. Even if this seems feasible for the continuous time case, if higher order dynamics (e.g electrical dynamics) are included the system can become unstable for large gains. Similarly, if the controller is implemented in discrete time, there is also a limit to the gain where the system becomes unstable. This happens because the gain margin for a discrete system is generally much lower than the gain margin for a continuous time system. This is another reason why it is not sufficient to do the analysis only in continuous time as will be better detailed in the following sections. From

3.4. Inherent limitations of the torque bandwidth

the above discussion we can conclude that the bandwidth limitation is related to the presence of the zero that depends on the viscous friction at load side B_l and inertia J_l (load dynamics) (see (3.3)). If high damping B_l is present in the system it will be possible to achieve a higher torque bandwidth. This means that in a system with more viscous friction it is easier to control the torque. On the other hand viscous friction is detrimental from the energy point of view, because more power will be required to perform dynamic motions and move the joint at higher speeds. In our system we design to have a very low friction at the joints. For the electric motor the limiting zero is located at a frequency of 5 rad/s. This means that the maximum torque bandwidth would be limited by this frequency. A different control strategy than a simple PI seems to be necessary to overcome this limitation. Higher order control and loop shaping techniques can be investigated that might consider canceling out poles and zeros of the system. However, these are not robust solutions in presence of parameter uncertainty.

The approach proposed in this thesis is to compensate for the natural load velocity feedback in order to make the torque dynamics independent from the load dynamics. The effect of the compensation is to move the system poles in order to eliminate or strongly reduce the detrimental effect of the zero in limiting the bandwidth. After this compensation a simple controller like a PI can be tuned to achieve the desired bandwidth without the above-mentioned limitations. To develop such compensation it is useful to open a parenthesis to gain *physical* understanding of the presence of this zero. To get a better understanding it is beneficial to do the analysis first on a simpler linear mechanical system. By this analysis we will obtain more general results and we will discover that this zero is a common feature of a force controlled system regardless of the type of actuator in use (e.g hydraulic/electric/pneumatic).

3.4.1 Load velocity influence on force dynamics: a simple example

In this section we will show that the natural load velocity feedback is present also in a basic mechanical system composed of an ideal velocity source vs , a transmission with stiffness K_t (to be distinguished from K_{te} of the electric actuator), a generic *load*, and the force F transmitted to the load (Fig. 3.5).

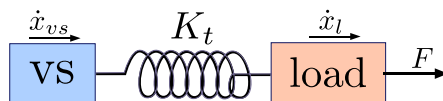


Figure 3.5: Generic spring-mass mechanical system representing a velocity source, that drives a load through a compliant transmission.

Through this compliant transmission element, the force is transmitted from the actuator to the load, where the force is normally measured. Since springs are impedances, they have veloc-

3. IMPROVED TORQUE CONTROL OF ELECTRIC ACTUATORS

ity as input to their dynamics and force as output. On the other hand, masses are admittances and have forces as input and velocity as output to their dynamics [Hogan, 1985]. In Fig. 3.5, the velocity source v_s is a mass, accelerated by an external actuator, and has an instantaneous velocity \dot{x}_{vs} , which is transmitted to the transmission spring. The spring output force F acts on the load mass, which is accelerated and has an instantaneous velocity \dot{x}_l . The load force dynamics \dot{F} can be written as:

$$\dot{F} = K_t (\dot{x}_{vs} - \dot{x}_l) \quad (3.5)$$

The presence of \dot{x}_l in (3.5) underlines that the dynamics of the force that is transmitted to the load depends also on the load itself, and not only on the actuator. The actuator dynamics defines how quickly the velocity \dot{x}_{vs} can be changed. On the other hand, the load dynamics determines how fast the load velocity \dot{x}_l can vary given an input force. This interaction between force and load dynamics is intrinsic to the physics, independent of the actuation and load characteristics, and it can be mathematically seen as a *load velocity feedback*. Based on the block diagram of Fig. 3.6, given that M_l is the mass and B_l is the damping of the load, we can calculate the following transfer function:

$$\frac{F(s)}{\dot{x}_{vs}(s)} = \frac{K_t (M_l s + B_l)}{s (M_l s + B_l) + K_t} \quad (3.6)$$

Looking at Fig. 3.6, we can notice that the pole of the load dynamics appears also as a zero of the force transfer function in (3.6). This result occurs regardless of how fast the actuation dynamics is [Dyke et al., 1995]. Thus, linking to the analysis done in the previous section, in a force closed-loop, the performance of the system is limited by the frequency of this zero.

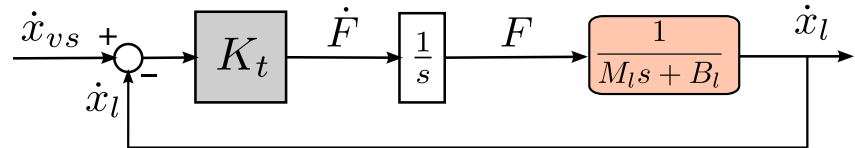


Figure 3.6: Block diagram for an ideal velocity source, acting on a load through a transmission stiffness. The load velocity \dot{x}_l is being fed back into the load force dynamics (*natural feedback*).

3.4.2 Load velocity compensation by positive velocity feedback for a simple mechanical system

As described in the previous subsection, the dynamics of the force/torque that is transmitted from the actuator to the load depends not only on the actuator dynamics but also on the load dynamics. However, if we want to control this load force, it is desirable that its dynamics only depends on the variable we can directly actuate, which is the velocity \dot{x}_{vs} for this generic mechanical case. An intuitive way of compensating this load motion influence is to measure the load velocity \dot{x}_l and to *continuously* apply, with our ideal velocity source, an extra velocity $\dot{x}_{ex} = \dot{x}_l$. In this case, the load force dynamics is given by:

$$\dot{F} = K_t [(\dot{x}_{vs} + \dot{x}_{ex}) - \dot{x}_l] = K_t \dot{x}_{vs} \quad (3.7)$$

Taking (3.7) into account, we can write the transfer function for the velocity-compensated system as:

$$\frac{F(s)}{\dot{x}_{vs}(s)} = \frac{K_t}{s} \quad (3.8)$$

The mathematical effect of the load velocity compensation is to algebraically eliminate the term K_t from the denominator of (3.6). This is equivalent to open the natural loop created by the load velocity feedback. By eliminating this term, a perfect zero/pole cancellation becomes possible and the same velocity-compensated dynamics (3.8) is obtained. Canceling out the influence of the zero on the force dynamics is the main consequence of the load velocity compensation. With this zero/pole cancellation, we are then able to increase the gains without making the system unstable, taking the dominant closed-loop pole to higher frequencies.

Considering a more realistic scenario, where we do not have an ideal velocity source, this extra velocity \dot{x}_{ex} has to be created by an actuator, which has its own dynamics. If this actuator dynamics influences significantly the force dynamics, we also need to take it into account when compensating for the load velocity as shown in Fig 3.7.

3.4.3 Load velocity compensation by positive velocity feedback for the electric actuator (model with two inertias)

The goal of this section is to find out the expression for the load velocity compensation for the HAA electric actuator. We will demonstrate that the zero/pole cancellation happens also in this case. We start from the expression of the derivative of the torque (3.9) and try to work out which is the compensation voltage $V_{m_{VC}}$ necessary to create a motion in the rotor of the motor

3. IMPROVED TORQUE CONTROL OF ELECTRIC ACTUATORS

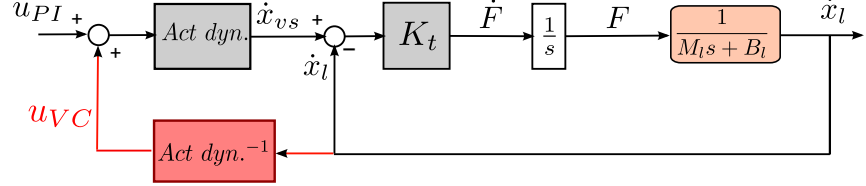


Figure 3.7: Block diagram for a generic velocity source with dynamics, acting on a load through a transmission stiffness. The natural feedback from the load velocity is compensated by a positive feedback (in red) by inverting the actuator dynamics.

that "follows" the load motion (see block diagram in Fig. 3.8). This way the torque derivative

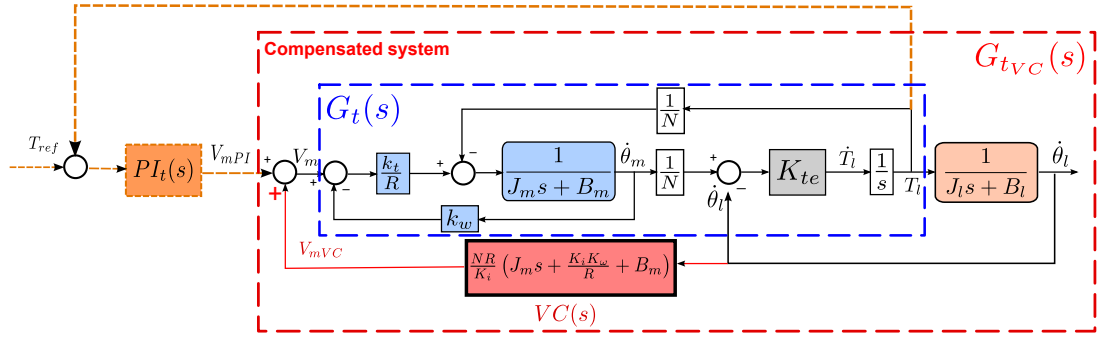


Figure 3.8: Block diagram for the electric actuator. The natural feedback from the load velocity is compensated by a positive feedback from load velocity by inverting the actuator dynamics ($VC(s)$). The velocity compensation will enable to control the torque as the load was still.

will not depend anymore on the load motion [Boaventura et al., 2012a] and the following holds:

$$\dot{T}_l = K_{te} \left(\frac{\dot{\theta}_m}{N} \right) \quad (3.9)$$

The expression of the motor voltage V_{mVC} that compensates for load motion is obtained by inverting the actuator dynamics (see appendix A.1 for the complete development):

$$V_{mVC} = \frac{N}{k_t} [R(J_ms + B_m) + k_t k_w] \dot{\theta}_{l1} = VC(s) \dot{\theta}_{l1} \quad (3.10)$$

The transfer function between torque T_l and load velocity can be obtained from the 3rd equation of (3.1):

$$\frac{\theta_l}{T_l} = \frac{1}{J_ls + B_l} \quad (3.11)$$

3.4. Inherent limitations of the torque bandwidth

Referring to Fig.3.8, the transfer function of the torque after closing the positive feedback from load velocity is:

$$G_{tvc} = \frac{T_l(s)}{V_{m_{pl}}(s)} = \frac{G_t}{1 - G_t \frac{1}{J_ls + B_l} VC(s)} \quad (3.12)$$

by setting, $F_1 = (J_ls + B_l)$ and $F_2 = (J_ms + B_m)$, for the sake of clarity and substituting G_t (3.3) and the $VC(s)$ gain of (3.10) into (3.12), we get:

$$G_{tvc} = \frac{\frac{k_t K_{te} N F_1}{R K_{te} F_1 + [RF_2 + k_t k_w] (J_ls^2 + sB_l + K_{te}) N^2}}{1 - \frac{\frac{k_t K_{te} N F_1}{k_t} \frac{N}{[RF_2 + k_t k_w]} }{R K_{te} F_1 + [RF_2 + k_t k_w] (J_ls^2 + sB_l + K_{te}) N^2} \frac{1}{F_1}} \quad (3.13)$$

rearranging, we get:

$$\begin{aligned} G_{tvc} &= \frac{k_t K_{te} N F_1}{R K_{te} F_1 + [RF_2 + k_t k_w] (J_ls^2 + sB_l + K_{te}) N^2 - K_{te} N^2 [RF_2 + k_t k_w]} \\ &= \frac{k_t K_{te} N F_1}{R K_{te} F_1 + [RF_2 + k_t k_w] N^2 (J_ls^2 + sB_l + K_{te} - K_{te})} \\ &= \frac{k_t K_{te} N F_1}{R K_{te} F_1 + [RF_2 + k_t k_w] N^2 F_1} \end{aligned} \quad (3.14)$$

By the last step we can see that by factoring out the term F_1 in the denominator, it is now possible to simplify it with the numerator leading (after substituting F_2) to a second order system:

$$G_{tvc} = \frac{\frac{k_t K_{te}}{RN}}{J_ms^2 + s \left(B_m + \frac{k_t k_w}{R} \right) + \frac{K_{te}}{N^2}} \quad (3.15)$$

This cancellation is very similar to the one described in 3.4.2 for the simple mechanical system. The effect of the feedback is to move the pole locations (not the zero) and in this particular case two complex conjugate poles are moved toward the real axis, one of them cancels the zero while the other one moves to the left on the real axis. In terms of the transfer function (3.3) this is represented by the algebraic elimination of the term K_{te} in the second step of (3.14). This allows to cancel the pole $(J_ls + B_l)$ with its respective zero. The compensated system therefore becomes a second order system and its poles depend only on motor parameters B_m ,

3. IMPROVED TORQUE CONTROL OF ELECTRIC ACTUATORS

J_m , k_t , k_w and on transmission stiffness K_{te} , and no longer on load dynamics (B_l and J_l). the block diagram of Fig. 3.9 show the system after the compensation where it can be seen that the natural velocity feedback from the load is not present anymore. If for this system transfer function between V_m and T_l is computed, G_{tvc} (3.15) it will obtained.

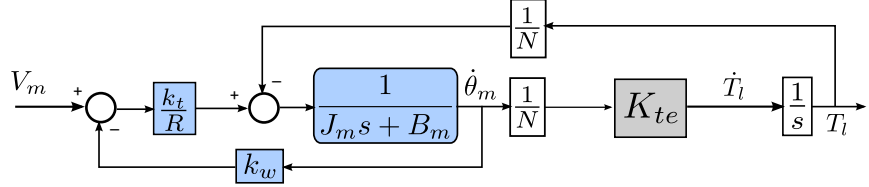


Figure 3.9: Block diagram of the compensated system (G_{tvc}).

This result is important because it has shown that the use of velocity compensation resulted in a system that is easier to control without the torque bandwidth limitations due to the zero. This enables to design a controller using well-established structure like a P, PI or PID and to achieve good control performance by increasing the gain to place the dominant pole at a high frequency.

3.4.4 Practical implementations of positive velocity feedback

As we demonstrated in the previous subsection, the velocity compensation cancels the zero that is present in the torque dynamics. This cancellation allows us to increase the controller gains and put the dominant pole at high frequencies without making the system unstable. However, the velocity compensation is a model-based compensation and is therefore susceptible to parameter uncertainties. The risk is that any control system that is designed on this idea can lack robustness and becomes very sensitive to parameter variations and uncertainties. Indeed, a perfect zero/pole cancellation is as challenging as creating a perfect model. In practice, the velocity will be either under or over-compensated.

Therefore, it is important to investigate the effects of a non-perfect cancellation in order to develop control strategies that can deal with it. In the zero-pole map of Fig. 3.10, we show the dominant open-loop poles of the compensated system for different levels of under and over-compensations. An under compensation places both dominant open-loop poles to the left side of the zero, and an over compensation places one pole to the left and another to the right. A slight over-compensation can make the system unstable for certain controller gains.

In the case of over-compensation if a PI controller is added to the system, as the controller gain increases the integrator pole at the origin and the pole to the right of the zero will collide and move around the zero (in a small circle) and become real again on the left hand side of the

3.4. Inherent limitations of the torque bandwidth

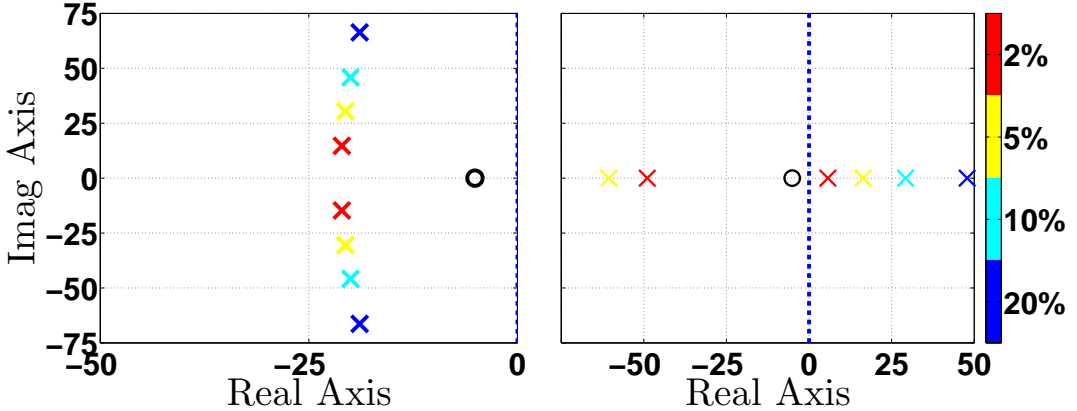


Figure 3.10: Open-loop poles for the compensated system: On the left plot we show the under compensation case, and on the right side we show the over-compensation one. The color bar illustrates different percentages of under/over compensations.

zero. This causes in any case an improvement of the bandwidth because the poles of the closed-loop system can be placed beyond the frequency of the zero. In case of under-compensation there is no benefit in terms of bandwidth because the zero can still attract the dominant pole introduced by the PI. Fig. 3.11 shows the root locus of the closed loop poles of the compensated system when the same PI controller (designed to have a zero in $s = -45\text{rad/s}$) is controlling the torque in the two cases. The root locus shows that in the under-compensated case, the dominant pole (and so the bandwidth) is limited by the frequency of the zero that attracts it (5 rad/s), while in the over-compensated case a bandwidth of 9 rad/s can be achieved. The conclusion is that in real implementations it is better to move a system pole to the right of the zero using enough positive feedback gain.

A practical issue of applying (3.10) is that the compensation also includes the derivative of the velocity (acceleration), which is usually quite noisy due to the double numerical differentiation. Filters could be used to reduce the noise but they would introduce delay that would be detrimental on the velocity compensation whose main target is to set a compensating voltage that changes promptly to load motion. However, simulation and empirical results showed that the influence of the term $J_m s \dot{\theta}_l$ in (3.10) is not significant in the range of frequencies of interest (J_m is two order of magnitudes lower than the other terms) and we will neglect it henceforth, the simplified velocity compensation is:

$$V_{mVC} = \frac{N}{k_t} [RB_m + k_t k_w] \dot{\theta}_l = VC(s) \dot{\theta}_l \quad (3.16)$$

It is worth to mention that by applying (3.16) instead of (3.10) it will no longer result in a

3. IMPROVED TORQUE CONTROL OF ELECTRIC ACTUATORS

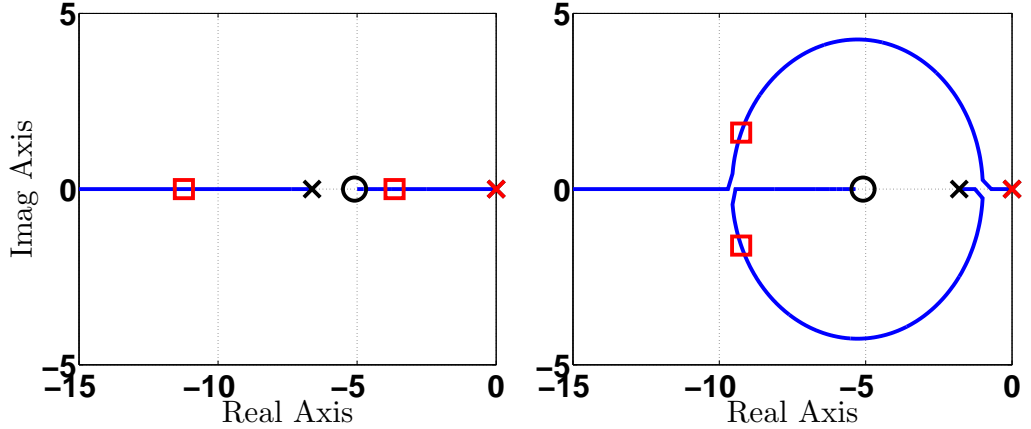


Figure 3.11: Root locus of the compensated system: on the left plot we show the under-compensated case (99.8%), and on the right side we show the over-compensated one (100.5%). Black crosses are the open loop poles, red squares are the closed loop poles moved by the controller. In the under-compensated case there is no benefit in terms of bandwidth when using a PI controller.

perfect cancellation (even with a perfect model). However, the poles will move qualitatively in a similar manner as with (3.10). Therefore according to the above discussion it is still possible to multiply (3.16) for an appropriate gain α in order to move the system pole to the right of the zero:

$$V_{mvC} = \alpha \frac{N}{k_t} [RB_m + k_t k_w] \dot{\theta}_l \quad (3.17)$$

3.5 Model with three inertias

The model with two inertias implemented in Section 3.3 turns out to be inaccurate when the electric actuator is mounted on the HyQ robot. Indeed the load represented by the HyQ leg (see Section 2.6) cannot be modeled as a single lumped inertia like we did for the rigid bar (see Fig. 3.2(left)) used for the identification. Therefore, it is necessary to derive a more accurate model and extend this model with the findings about velocity compensation before carrying out the design of the torque controller. To determine the order of the model necessary to describe the new system, represented by the actuator and the leg, we repeated the open loop tests using the same chirp signal. By inspecting the data we can see that an anti resonance (at 12 Hz) appeared in the link velocity response (Fig. 3.12) that was not present in the chirp tests carried out with the rigid bar.

Vibrational mechanics [Bishop and Johnson, 2011] tells us that this anti-resonance is an

3.5. Model with three inertias

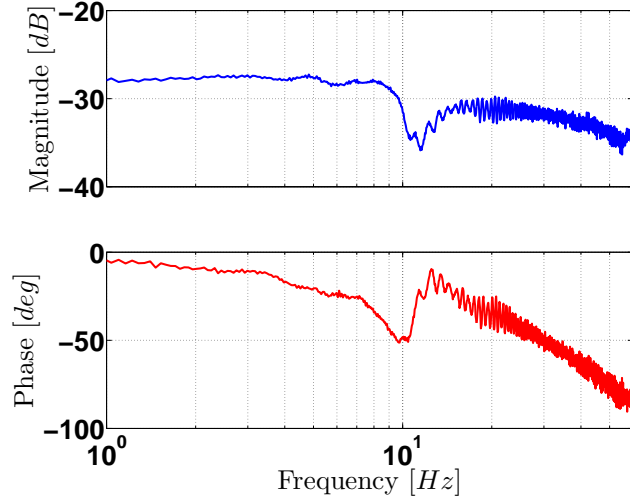


Figure 3.12: Frequency response of the link velocity to a chirp input voltage V_m . An anti-resonance is present at 12Hz.

indication of an additional spring-mass pair that is connected in series to the point where we are measuring the velocity. It follows that a model with two inertia and one spring cannot capture this behavior and a more complex model with three inertia coupled by two springs must be used, as shown in the schematic in Fig. 3.13 where K_{te} and K_p are the stiffnesses related to the gearbox and the leg flexibility, respectively.

Looking at a frontal view of the leg (Fig. 3.15(right)) the leg compliance K_p is the torsional compliance due to the mechanical elasticity of the structure while K_{te} is the gearbox compliance. D_p and D_{te} are the relative damping terms. The intermediate inertia J_{L1} in Fig. 3.13

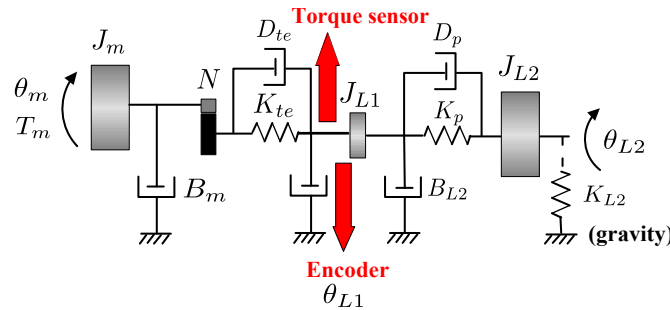


Figure 3.13: Motor drive system with torsional load, schematic for the 3 inertia-2 spring model.

represents the mechanical part that interfaces the leg inertia J_{L2} with the gearbox as shown in Fig. 3.14. J_m , the inertia of the rotor of the electric motor remains unchanged. According to the topology depicted in Fig. 3.14 the position encoder measures the angle θ_{L1} of the intermediate

3. IMPROVED TORQUE CONTROL OF ELECTRIC ACTUATORS

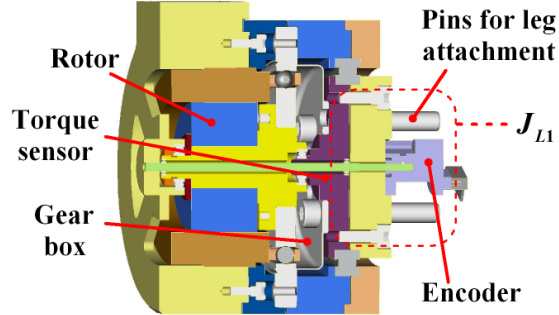


Figure 3.14: Cross-section of the mechanical assembly of the electric joint. The red box indicates the intermediate inertia J_{L1} that represents the mechanical interface part between the leg and the gearbox.

inertia J_{L1} while in the model with two inertia the encoder was measuring θ_l . This is because in the three inertia model we need to choose which variable to consider when we are generically speaking about the "load position". Despite being useful distinguishing θ_{L1} from θ_{L2} from the modeling point of view, in practice to control the leg position for locomotion, we will assume the leg position is represented by the variable that we measure (θ_{L1}). Indeed, the leg structure is designed to have low compliance ($1.9 \cdot 10^3 \text{Nm/rad}$) and the positioning error introduced by its deformation is small. Link velocity is measured by averaging first order differences of the position encoder by a moving average filter (4 samples).

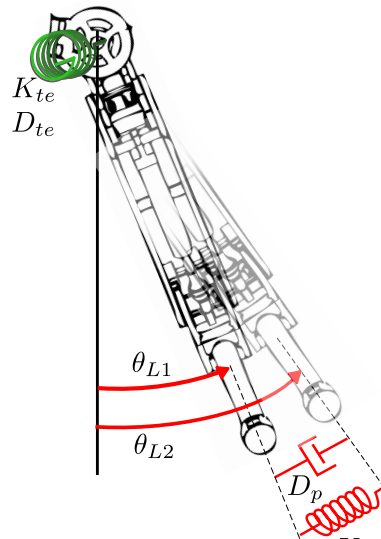


Figure 3.15: Frontal view of the HyQ leg. The rotational stiffness K_p and damping D_p are resembling the compliance/damping of the leg mechanical structure and while K_{te}, D_{te} are the compliance/damping of the gearbox transmission.

3.5. Model with three inertias

The electrical dynamics that were neglected in section 3.3 for sake of simplicity, are now included in this more refined model. However, when the loop is closed with a high gain, its influence may not be negligible anymore. In fact, with a higher loop gain, the electrical dynamics may in fact become faster but the other dynamics can move towards the imaginary axis and eventually cross the stability boundary. Also the damping D_{te} in the gearbox is added to the model together with the damping of the mechanical structure of the leg D_p . According to the schematic depicted in Fig. 3.13, the Laplace transforms of the differential equations of the model with three inertia are:

$$\begin{aligned} (Ls + R)I_m &= V_m - k_w s \theta_m \\ (J_ms + B_m)s\theta_m &= k_t I_m - \frac{1}{N}(K_{te} + sD_{te})(\frac{\theta_m}{N} - \theta_{L1}) + T_{fr} \\ (J_{L1}s + B_{L1})s\theta_{L1} &= -(K_p + sD_p)(\theta_{L1} - \theta_{L2}) + (K_{te} + sD_{te})(\frac{\theta_m}{N} - \theta_{L1}) \\ (J_{L2}s + B_{L2})s\theta_{L2} &= (K_p + sD_p)(\theta_{L1} - \theta_{L2}) + T_{dist} \end{aligned} \quad (3.18)$$

where I_m , θ_m denote the motor current and motor angular position; θ_{L1} and θ_{L2} are the angular position of the intermediate inertia and of the leg; V_m is the motor voltage. Differently from the model (3.3) two input disturbances: T_{fr} and T_{dist} have been introduced because they will be part of further analysis in the following sections. T_{fr} is the friction torque due to the harmonic drive gearbox while T_{dist} is an external disturbance torque that may be applied to the leg. Values for K_{te} , D_{te} , K_p , D_p , J_{L1} , B_{L1} , B_{L2} were estimated using open loop chirp tests as in (3.4.3) and are reported in Table 3.2. The leg inertia J_{L2} is variable and depends on the configuration of the hydraulic joints HFE, KFE. In particular it will be minimum (lower bound) when the leg is retracted and maximum (upper bound) when it is completely extended. These values are obtained from CAD data. For J_m , B_m , k_t and k_w the values reported in Table 3.1 remain valid, because the electric actuator is unchanged.

In Fig. 3.16 we compared simulation results obtained by the identified model with experimental data. The plot shows the velocity $\dot{\theta}_{L1}$ in response to an input chirp signal. The simulated output fits well with the measured experimental data in the range of frequency of interest. The anti-resonance at 12 Hz is clearly visible in the plot at $t = 1.9s$. Quantization effects due to the sampling rate (1 kHz) are present in the plot of the real data.

We will consider, henceforth, this model as the default model for the future analysis. Considering the damping D_{te} in the transmission, the torque transmitted to the load J_{L1} , measured by the torque sensor, can be expressed as:

$$T_l = (K_{te} + sD_{te}) \left(\frac{\theta_m}{N} - \theta_{L1} \right) \quad (3.19)$$

3. IMPROVED TORQUE CONTROL OF ELECTRIC ACTUATORS

Table 3.2: Additional identified parameters for model with three inertia

Name	Description	Value	Origin
$J_{L1} [kgm^2]$	Intermediate inertia	$1 \cdot 10^{-4}$	Identified
$J_{L2} [kgm^2]$	Leg inertia	0.439 leg ext. 0.129 leg ret.	CAD
$K_p [Nm/rad]$	Leg stiffness	$1.923 \cdot 10^3$	Identified
$D_p [Nms/rad]$	Leg damping	7.56	Identified
$B_{L1} [Nms/rad]$	Visc. friction inertia J_{L1}	0	Identified
$B_{L2} [Nms/rad]$	Visc. friction inertia J_{L2}	0.756	Identified
$K_{te} [Nm/rad]$	Gearbox stiffness	$8.0769 \cdot 10^3$	Identified
$D_{te} [Nms/rad]$	Gearbox damping	16.56	Identified

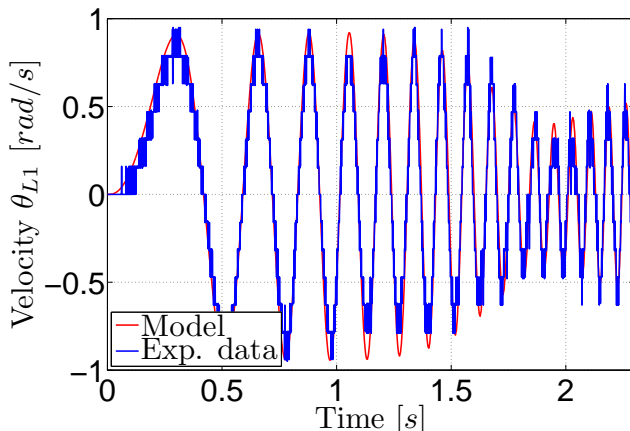


Figure 3.16: Velocity $\dot{\theta}_{L1}$ response to the chirp input, simulation (red) and experiments (blue). The nice fitting of the data demonstrates the accuracy of the model for a large range of frequencies. The 12 Hz anti-resonance is visible at a time $t = 1.9\text{s}$.

From (3.18) and (3.19) the transfer function from the motor voltage V_m to the load torque T_l is given by (see appendix A.2 for the complete derivation):

$$G_t = \frac{k_t(D_{te}s + K_{te})p_1}{N(p_1q_1 + q_2q_3)} \quad (3.20)$$

3.5. Model with three inertias

where:

$$\begin{aligned}
 p_1 &= (J_{L2}s^2 + B_{L2}s)(J_{L1}s^2 + B_{L1}s) \\
 &\quad + [(J_{L2}s^2 + B_{L2}s) + (J_{L1}s^2 + B_{L1}s)](D_p s + K_p) \\
 q_1 &= (Ls + R) \left(J_m s^2 + B_m s + \frac{D_{tes} s + K_{te}}{N^2} \right) + k_t k_w s \\
 q_2 &= \frac{N}{k_t} (Ls + R)(J_m s^2 + B_m s) + N k_w s \\
 q_3 &= \frac{k_t}{N} (J_{L2}s^2 + B_{L2}s + D_p s + K_p)(D_{tes} s + K_{te})
 \end{aligned} \tag{3.21}$$

Without considering higher frequency poles and zeros, the system still has two resonant poles and one zero close to the imaginary axis (see Fig. 3.17 (left)) as in the case of the model with two inertia. Therefore, the same bandwidth limitations are present for torque control. Hence, a similar development like the one done for the model with 2 inertia will be carried out to address these limitation in Section 3.5.2. The following is a specific section where a refinement of the model is presented, which includes the effect of gravity. Readers that are not interested in these details, might skip directly to Section 3.5.2, paying attention that gravity will be included in the model.

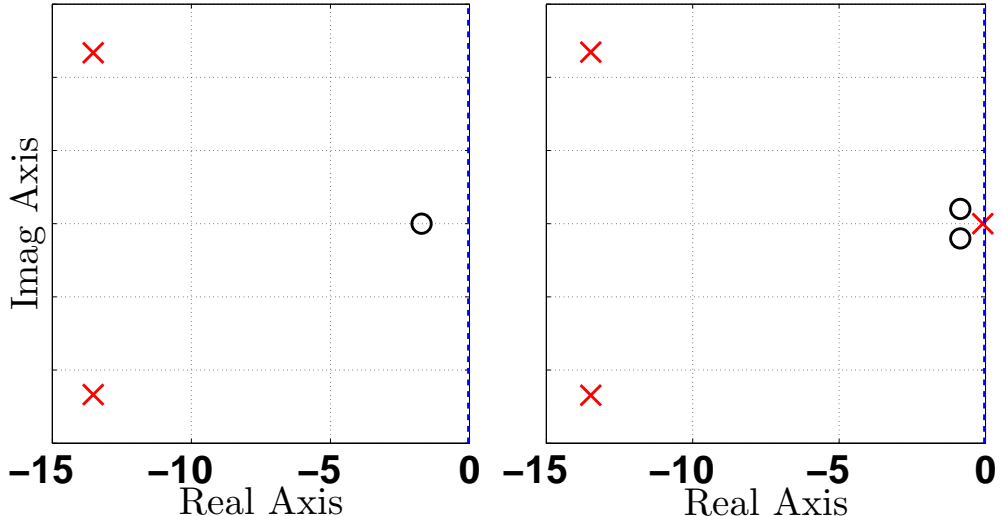


Figure 3.17: Open-loop poles and zeros of the transfer function G_t computed for the model with three inertia including gravity (right) and without gravity (left). The effect of gravity leads to have two complex zeros instead of a real one close to the imaginary axis.

3. IMPROVED TORQUE CONTROL OF ELECTRIC ACTUATORS

3.5.1 Influence of gravity

Up to this point, gravity has been neglected for the sake of simplicity. As known gravity can be modelled as a non-linear position dependent torque on the load dynamics. If we linearize the dynamics of the load (around the operating point $\theta_{L1} = \theta_{L2} = 0$) it is possible to model the gravity as a torsional spring K_{L2} (see Fig. 3.13). Therefore, the load dynamic equation becomes:

$$(J_{L2}s + B_{L2})s\theta_{L2} = (K_p + sD_p)(\theta_{L1} - \theta_{L2}) - K_{L2}\theta_{L2} + T_{dist} \quad (3.22)$$

In Table 3.3 we present the computed values of the "gravity" spring for the leg in retracted and extended configuration: The effect of gravity on the torque transfer function G_t is that a term

Table 3.3: Gravity parameters

Name	Description	Value	Origin
K_{L2}	Linear stiffness due to gravity	7.17 Nm/rad leg ext. 11.2 Nm/rad leg ret.	computed

K_{L2} will appear in p_1 and q_3 of (3.21) that become:

$$\begin{aligned} p_1 &= (J_{L2}s^2 + B_{L2}s + K_{L2})(J_{L1}s^2 + B_{L1}s) \\ &\quad + [(J_{L2}s^2 + B_{L2}s + K_{L2}) + (J_{L1}s^2 + B_{L1}s)](D_ps + K_p) \\ q_3 &= \frac{k_t}{N}(J_{L2}s^2 + B_{L2}s + D_ps + K_p + K_{L2})(D_{te}s + K_{te}) \end{aligned}$$

From the point of view of the root locus, the effect of gravity leads to two complex zeros instead of a real one close to the imaginary axis as shown in Fig. 3.17. We will show in the following section that the velocity compensation can have a beneficial effect also in this case.

3.5.2 Load velocity compensation by positive velocity feedback for the electric actuator (model with three inertias)

Similarly to what we did in Section 3.4.3 for the model with two inertias, in this section we will work out which is the positive velocity compensation feedback gain $VC(s)$ for the model with three inertia. First it will be shown how this compensation will result in a perfect cancellation of the bandwidth-limiting zeros in the torque transfer function. Then the practical implementation of the compensation will be discussed in a similar fashion as Section 3.4.4. Since we are considering the electrical dynamics we will have to account for it in the velocity compensation

3.5. Model with three inertias

gain:

$$V_{mVC} = \frac{N}{k_t} [(Ls + R)(J_ms + B_m) + k_t k_w] \dot{\theta}_{L1} = VC(s) \dot{\theta}_{L1} \quad (3.23)$$

Apart from the term Ls that represents the electrical dynamics, the equation 3.23 is the same as (3.10) because the dynamics of the electric motor is unchanged after the introduction of the leg in place of the rigid bar. By closing the velocity loop using (3.23), the transfer function from the motor voltage V_m to the load torque T_l can be obtained (see appendix A.3 for the complete derivation):

$$G_{tvc} = \frac{k_t(D_{te}s + K_{te})p_1}{N(p_1q_1 + (q_2 - VC(s)q_3))} \quad (3.24)$$

where:

$$\begin{aligned} p_1 &= (J_{L2}s^2 + B_{L2}s + K_{L2})(J_{L1}s^2 + B_{L1}s) \\ &\quad + [(J_{L2}s^2 + B_{L2}s + K_{L2}) + (J_{L1}s^2 + B_{L1}s)] (D_p s + K_p) \\ q_1 &= (Ls + R) \left(J_ms^2 + B_ms + \frac{(D_{te}s + K_{te})}{N^2} \right) + k_t k_w s \\ q_2 &= \frac{N}{k_t} (Ls + R)(J_ms^2 + B_ms) + Nk_w s \\ q_3 &= \frac{N}{k_t} (J_{L2}s^2 + B_{L2}s + D_p s + K_p + K_{L2})(D_{te}s + K_{te}) \end{aligned}$$

Note that the zeros in (3.24) introduced by the polynomial p_1 depend entirely on the load dynamics (where the load is represented by the two inertias J_{L1} and J_{L2}). When the damping coefficients B_{L1} and B_{L2} are small, as in the case of HyQ's electric actuator, some of these zeros are very close to the stability region boundary. In the case of continuous time systems the boundary is the imaginary axis and in the case of discrete time systems it is the unit circle. Note that the zeros may be real or complex (see Fig. 3.17 (right)) depending on the value of the stiffness K_{L2} . As happens for the model with two inertia, these zeros impose limitations in the achievable closed loop bandwidth when using a simple proportional and integral torque controller. This is because the controller pole will be attracted towards the zeros and the closed loop bandwidth of the torque loop will be limited even if high gains are used in the torque controller.

The effect of the velocity compensation is that these unwanted zeros can be cancelled if the velocity feedback gain is chosen as $VC(s) = q_2/s$. If this is the case the term p_1 in the numerator of (3.24) can be canceled out with the term p_1 in the denominator.

3. IMPROVED TORQUE CONTROL OF ELECTRIC ACTUATORS

3.5.3 Practical implementation of positive velocity feedback and discussion

As already explained in Section 3.4.4 the implementation of the compensator in (3.23) requires second and third order derivatives of the velocity signal that, as shown in Fig 3.16 is prone to quantization errors. Since these higher order derivatives would be very noisy, the compensator has to be approximated to (3.17) which is obtained by discarding the derivative terms from (3.23). Therefore, an exact cancellation of the transmission zeros p_1 is not possible anymore. Nevertheless, the use of the simplified velocity compensation (3.17) results in an improvement in the closed loop torque bandwidth by tuning the compensation gain α .

$$VC(s) = \alpha \frac{N}{k_t} [RB_m + k_t k_w] \quad \alpha > 0 \quad (3.25)$$

For the parameter values given in Table 3.2 and setting $K_{L2} = 0$, the polynomial p_1 has four real roots $z_4 < z_3 < z_2 < z_1 = 0$. The transfer function (3.24) has also a pole at zero. This is an unobservable pole and therefore it is canceled out with the zero z_1 . The second zero z_2 is the closest to the imaginary axis and this zero limits the torque bandwidth that can be achieved with a PI torque controller. As the compensation α increases one real pole in (3.24) moves towards the stability boundary along the real axis and for a certain value of the gain α the pole will become identical to z_2 . This is the ideal value for the gain α required for cancelling the unwanted zero at z_2 . In this particular case, z_2 varies as a function of the leg inertia. Hence, it may be difficult to completely cancel out this zero for all leg configurations with a fixed value for α (gain-scheduling approaches might be useful at this respect). However, as long as the pole in (3.24) is placed to the right of the zero z_2 then the bandwidth limitation introduced by this zero is avoided. When the gravity is taken into account ($K_{L2} \neq 0$) then the roots of p_1 , which are closest to the imaginary axis (z_1 and z_2) are complex conjugate (see Fig. 3.17). As α increases two poles in (3.24) will move towards the imaginary axis as a complex conjugate pair, but there is no value of α that will completely cancel out the unwanted zeros z_1 and z_2 . In this case the velocity compensation will not be as effective as for the case where $K_{L2} = 0$. Nevertheless, it still results in an improvement of the achievable closed loop torque bandwidth. This can be demonstrated in simulation. Fig. 3.18 compares 1Nm torque step responses generated with and without the velocity compensation in the case the gravity is included or excluded from the model. For the simulations a PI controller has been used to close the torque loop whose design will be described in the next section.

Fig. 3.18 has two purposes: first to show the influence on the torque control of introducing the gravity in the model and second, to demonstrate the improvement in torque tracking due to velocity compensation. When gravity is considered the torque bandwidth is low and the re-

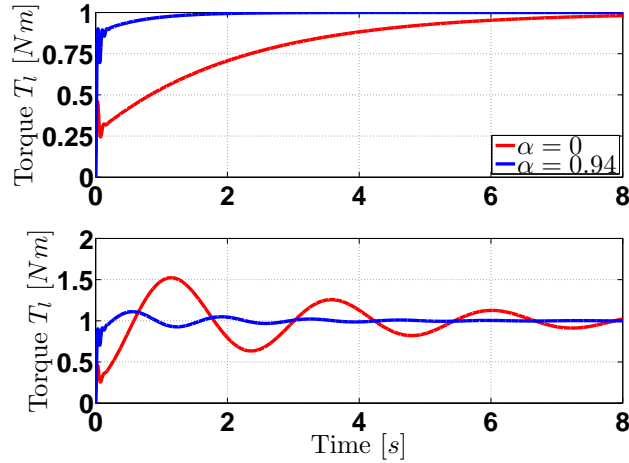


Figure 3.18: Torque step responses without gravity $K_{L2} = 0$ (upper plot) and with gravity $K_{L2} = 11.2 \text{Nm}/\text{rad}$ (lower plot) for different velocity compensation gains: $\alpha = 0.94$ (blue) and $\alpha = 0$ (red). The leg inertia for the extended configuration ($J_{L2} = 0.439 \text{kgm}^2$) is considered.

spose is oscillatory and needs several seconds to settle. However, a significant improvement is achieved by using velocity compensation. Similar results can be established after discretization of the continuous time system. It is worth mentioning that the following simulation are carried out with the leg free to move in the air. Indeed, the dynamics is very different, when an actuator is connected to a finite inertial load (as it is the case of the HyQ leg) or when it is rigidly connected to the ground [Robinson, 2000]. In general the torque bandwidth is much higher in the second case than in the first case. If we consider the actuator connected to ground, whenever the controller is commanding a voltage to the motor to track a torque reference, the force immediately rises due to the compression of the transmission compliance. Conversely, in the case the actuator is connected to a load which is free to move in the air, as soon the force start to rise the load starts to move making the force drop. This is because the spring initially compress then, as soon the load accelerates, it uncompresses again. The outcome is that the controller will delay consistently in following the desired force due to the continuous exchange between load kinetic energy and elastic potential energy in the transmission. Velocity compensation eliminates this by making the torque control perform as if the load is rigidly interconnected to the ground, thus achieving the same high bandwidth even if the load is moving.

3.6 Torque controller design

In the previous sections a lot of effort has been put in accurate modeling and in designing a positive feedback compensation to eliminate the intrinsic bandwidth limitation in torque control

3. IMPROVED TORQUE CONTROL OF ELECTRIC ACTUATORS

that arise when the load is free to move. In this section we will reap the benefit of this effort by designing a PI torque controller (see Fig. 3.19) for the model of the compensated system, that will meet our specifications. The *MA* filter in the figure indicates an averaging filter to reduce quantization noise in the velocity signal.

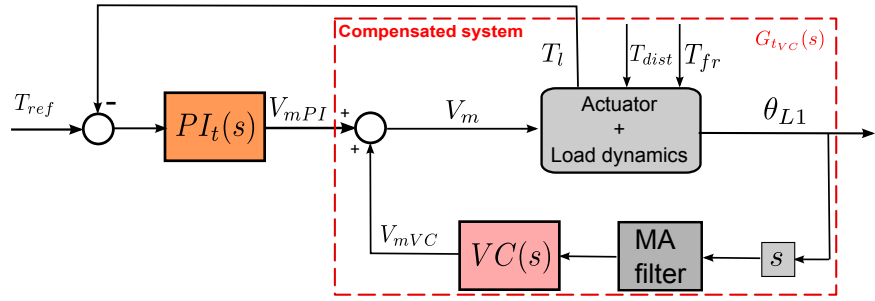


Figure 3.19: Block diagram of the compensated system with a PI torque controller.

Henceforth all the design and analysis will be carried out in discrete time, because sampling introduces noticeable differences in comparison to the continuous time case. For example the system can become non-minimum phase even if the underlying continuous time is of minimum phase (non-minimum phase systems are more difficult to control).

A discrete time implementation of the PI controller is:

$$PI_t(z) = P_t + I_t \frac{zT_s}{z-1} = (P_t + I_t T_s) \frac{(z - \frac{P_t}{P_t + I_t T_s})}{z-1} \quad (3.26)$$

where z is the Z-transform variable and $T_s = 1ms$ is the sampling time interval; P_t and I_t are the proportional and integral gains to be determined. Traditionally, the design of an inner loop controller is carried out with the aim of maximizing the closed loop bandwidth of the inner loop. Further, it is not obvious that maximizing the bandwidth of the torque loop is always consistent with the specifications for an outer loop (in our case an impedance loop). In the approach presented in this thesis the controller gains were selected so that the loop gain has a phase margin larger than 30° and a gain margin larger than 12 dB for the upper and lower bounds of J_{L2} and K_{L2} when a velocity compensation gain of $\alpha = 0.94$ is set. This would result in a response with good robustness to parameter variations (e.g. gravity, inertia, delays in the MA filter). In addition, the closed loop torque response was required to be stable for all values of the velocity compensation gain α between zero and one (but the gain and phase margins can be less than 12 dB or 30 degrees, respectively). A set of controller gains satisfying the given

3.6. Torque controller design

specifications are:

$$P_t = 0.382\beta \quad I_t = 18\beta \quad 25 > \beta > 0 \quad (3.27)$$

Changing the gain β only affects the static gain of the controller but the controller zero remains fixed. This gives ample freedom to investigate the effects of increasing the closed loop torque bandwidth (by changing the torque loop gain β) when the outer loop specifications are considered. It is important to remark that as in all robotic applications, we must consider that the load inertia is rarely constant, thus the controller must perform well for a range of load inertias.

Table 3.4 presents a sensitivity analysis about how the torque bandwidth (-3dB) is varying in accordance to variations of the velocity compensation gain α and of the leg inertia J_{L2} , keeping the torque controller gain fixed to $\beta = 1$. The leg inertia is always bounded between these two extreme cases (in extended and retracted configuration):

Table 3.4: Closed loop torque bandwidth

J_{L2}[kgm²]	α	Bandwidth [Hz]
0.439	0.985	18.4
0.439	0.94	4.44
0.439	0.85	1.49
0.439	0.6	0.17
0.439	0	0.08
0.129	0.985	2.23
0.129	0.94	1.37
0.129	0.85	0.48
0.129	0.6	0.2
0.129	0	0.09

The results in Table 3.4 show that the torque bandwidth significantly increases with the velocity compensation gain α while the same controller gain $\beta = 1$ is maintained. Also the leg inertia plays a role. As explained in the previous section on loads with lower inertia it is harder to control the torque. This is confirmed by the results in the table where the torque bandwidth for the lower inertia (retracted leg) is globally lower than in the case with the larger inertia (extended leg).

To experimentally demonstrate the influence of the velocity compensation we fixed a 5 kg weight to the foot tip of real leg end-effector to create an artificial load and permit a reasonable

3. IMPROVED TORQUE CONTROL OF ELECTRIC ACTUATORS

step magnitude. Then we commanded a 10 Nm torque step leaving the leg free to move in the air. Adding a mass to the foot tip is very important because an outer position loop is not closed and without the 5kg mass the leg, which is very light, would move and hit its end-stop. We compare in Fig. 3.20 the system response with $\alpha = 0.94$ and without $\alpha = 0$ velocity compensation. Velocity compensation improves significantly the torque loop bandwidth but the

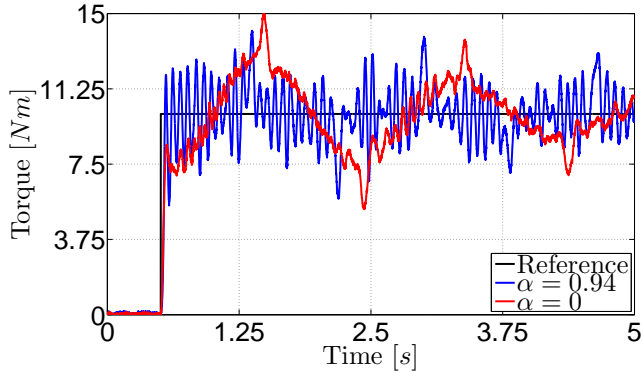


Figure 3.20: Experimental response to a 10 Nm step reference for the torque. A gain $\beta = 1$ has been set for the PI controller. The black line is the reference, the blue line the response when velocity compensation is active $\alpha = 0.94$, and the red when it is not active $\alpha = 0$.

response becomes very oscillatory. This happens because the velocity compensation amplifies the torque ripple generated by the harmonic drive (T_{fr}). In the following section we will present a methodology to address this problem.

3.7 Torque compensator to compensate harmonic drive cyclic friction

One drawback of using a harmonic drive gearbox is that it introduces torque ripples. The problem is related to the working principle of the gearbox that is based on the motion of an elliptic element (wave generator). This motion creates torque fluctuations with a fundamental frequency which is twice the wave generator angular velocity. While this disturbance is normally neglected in position control schemes, because it is passively filtered out by the inertia of the system, conversely it has a detrimental effect on torque control and creates vibrations and wearing of the components. In our electric actuator we identified that disturbance to be:

$$T_{fr} = \frac{1.3}{N} \cos(2\theta_m + \pi) \quad (3.28)$$

This term is added to the motor torque in the first equation of (3.18). To understand how

3.7. Torque compensator to compensate harmonic drive cyclic friction

to reduce the effect of this disturbance on the closed loop torque response, it is useful to plot the bode diagram of the relative transfer function. That is between the torque ripple T_{fr} and the torque T_l . Figure 3.21 shows that there is a resonance at 15Hz for which the disturbance is strongly amplified (magnitude -4.2 dB, blue line) and therefore can lead to unwanted vibrations on the torque. Without velocity compensation (red line) the disturbance is more attenuated (-10dB at the resonance).

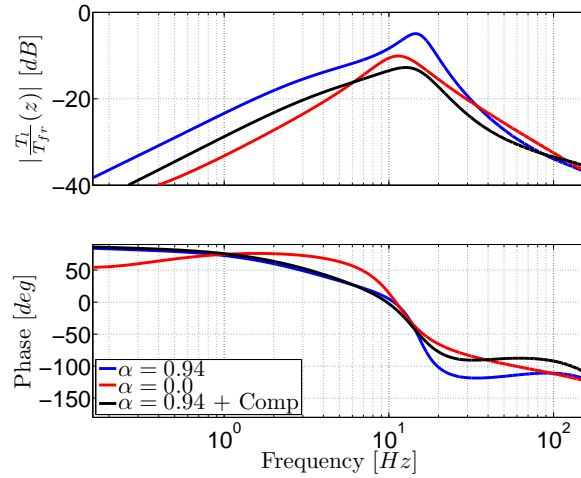


Figure 3.21: Bode diagram of the closed loop torque sensitivity to the disturbance T_{fr} with (blue) and without (red) velocity compensation and (black) using velocity compensation and the torque compensator. Leg inertia is $J_{L2} = 0.439$.

This effect can be mitigated by designing an additional compensator to reduce the effect of torque ripples in the harmonic drive. An alternative is to pursue a more complex torque loop controller (with more degrees of freedom) so that it is possible to track torques and at the same time reject the disturbances caused by the gearbox. We will present here the first solution. The target is to further reduce the peak of the sensitivity plot trying to make it below -10 dB also when velocity compensation is used which seems to be a worsening effect. To do this we design a lead/lag compensator (notch) that adds a phase lead at the resonance of 15Hz. This compensator has a pair of complex zeros and poles.

$$C_{comp}(z) = K_{comp} \frac{z^2 + 2\xi\omega_n z + \omega_n^2}{z^2 + 2\xi\omega_n z + \omega_n^2} = 5.2 \frac{z^2 - 1.882z + 0.8916}{z^2 - 1.616z + 0.6659} \quad (3.29)$$

The zeros have been placed close to the 15Hz resonance (at higher frequency) in order to have a 45° phase lead at the resonance. The two poles are placed at a high frequency to make the compensator proper. Finally the scalar K_{comp} is set to have unity DC-gain for the controller at

3. IMPROVED TORQUE CONTROL OF ELECTRIC ACTUATORS

low frequency. The bode diagram of the controller is illustrated in Fig. 3.22.

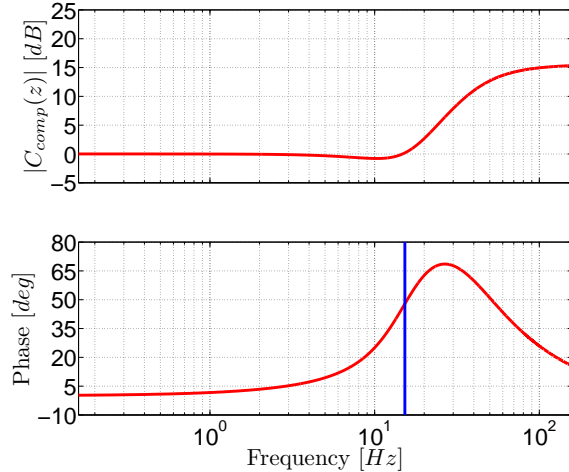


Figure 3.22: Bode diagram of the designed lead-lag compensator to reduce torque ripple disturbances created by the harmonic drive gearbox.

The use of the compensator combined with velocity compensation enables a reduction of the peak in Fig. 3.21 from -4.2 dB to -12.5 dB . This way is possible to still benefit of the advantages of velocity compensation without the drawback of the amplification of the wave generator noise. Note that this compensator is place in cascade to the output of the torque PI controller and is implemented as a digital filter. Experiments have been repeated in similar conditions as the ones shown in Fig. 3.20. Fig. 3.23 is a plot of the experimental result and show the improvements of using the compensator in terms of reduction of the oscillations in the torque response.

3.8 Summary

This chapter has presented the design of a torque controller for the *HAA* joint of HyQ. In particular positive feedback velocity compensation has been introduced and used to improve the limitations on the torque bandwidth that are intrinsically present when controlling the torque on a load that is not rigidly fixed to the ground. The origin of these limitations has been discussed in a general case then the specific compensation gain has been found for the electric actuator (*HAA*) in use for HyQ. The main benefit of the compensation is that the force/torque is easier to control in the compensated systems (with simple controller structures like P, PI). Two models have been proposed to describe the system made of actuator connected to an inertial load. Namely a model with *two inertia* describes the system when a short rigid bar is con-

3.8. Summary

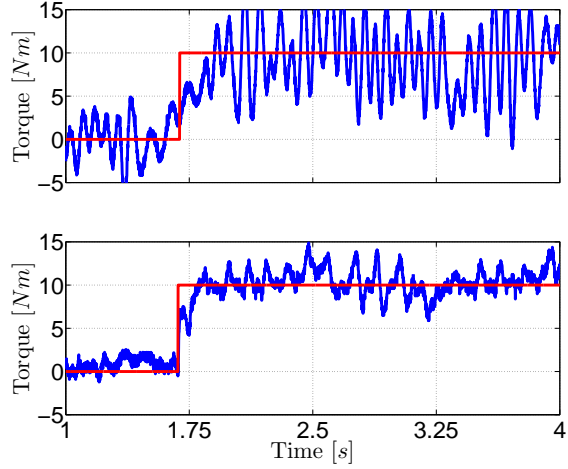


Figure 3.23: Experimental response to a 10 Nm step reference for the torque. A gain $\beta = 1$ has been set for the PI controller and $\alpha = 0.94$. The red line is the reference, the blue line the actual torque response. The upper plot is the case without torque compensator while the lower plot is with torque compensator.

nected to the electric motor while a model with *three inertia* respresents the system when the HyQ leg is attached, taking into account the additional compliance of the mechanical structure. A reliable model is a useful tool for designing controllers and carrying out accurate analysis to improve the control performance of the system without having to carry out expensive and time-consuming sets of experiments. Finally, a PI torque controller has been designed based on the model where the velocity compensation feedback loop was closed, demonstrating the improvements in bandwidth by using the above-mentioned compensation. A by-product of velocity compensation is an undesired amplification of the torque ripple generated by the harmonic drive gearbox. To reduce the effects of these torque disturbances on the torque output an additional torque compensator has been designed based on the idea of a notch filter.

3. IMPROVED TORQUE CONTROL OF ELECTRIC ACTUATORS

4

Impedance control

THIS chapter is divided in two part: the first part presents the implementation of the impedance controller for one single joint the second part for the whole leg.

4.1 Impedance control for the adduction/abduction joint

In the previous chapter we built an accurate model of the abduction/adduction joint (electric actuator) attached to one leg of the HyQ robot. Using this model, the implementation of a torque loop has been presented with different solutions to improve it in terms of bandwidth and disturbance rejection. In particular we have shown that bandwidth can be increased by using velocity compensation. This is true for the torque loop alone; however, when an outer impedance loop is closed the dynamic of the controlled system changes, and mutual influences exist between the inner and the outer loop. Neglecting these mutual interactions might lead to results and conclusions that are incorrect and not representing reality. In particular maximizing the bandwidth of the inner loop can be useful to enlarge the range of frequency in which the real impedance *tracks* the desired one but creates stability problem if certain combinations of impedance gains are chosen. Furthermore, real implementations of impedance control (filtering, sampling) may suffer from several limitations that restrict its applicability. This chapter presents a methodology to analyze and predict these limitations in the impedance control and suggest some practical rules of thumb for the selection of impedance parameters suitable for locomotion.

4.1.1 Motivation

A common practice in designing nested loop control systems is to maximize the bandwidth of the innermost loop. This is a widely spread belief that many researchers assume to be valid

4. IMPEDANCE CONTROL

without carrying out the relevant analysis [Ellis, 2000]. In general, it turns out that maximizing the inner loop controller bandwidth is not always the best strategy. Indeed, when the outer impedance loop is closed, designing the inner loop to have the highest possible bandwidth reduces the range of impedance parameters for which the whole system is stable, as presented later in this section. Therefore, a trade-off must be found between different requirements: having a high bandwidth to ensure good torque tracking and impedance emulation, and keeping the bandwidth low to increase the range of stable impedance values that can be rendered.

Other limitations arise in the real implementations of the controller (e.g. in discrete time). For instance other aspects that directly influence the stability region are the sampling frequency and filtering [Janabi-Sharifi et al., 2000]. Their effect is to introduce delays into the control loop, and their influence will also be investigated in this chapter.

4.1.2 Implementation

Considering the torque loop implemented in (3.6) an impedance controller is added as an outer loop as shown in Fig. 4.1. The impedance gains P_{gain} and D_{gain} represent the stiffness and damping for the HAA joint. For the remainder of this document these gains units will be expressed in SI units, e.i Nm/rad for P_{gain} and Nms/rad for D_{gain} and henceforth they will be omitted for sake of brevity. The output of the controller provides the reference torque T_{ref} for the inner loop:

$$T_{lref} = P_{gain}(\theta_{L1ref} - \theta_{L1}) - D_{gain}\dot{\theta}_{L1} \quad (4.1)$$

where T_{ffwd} is an external compensation torque that can be added, for example, to remove

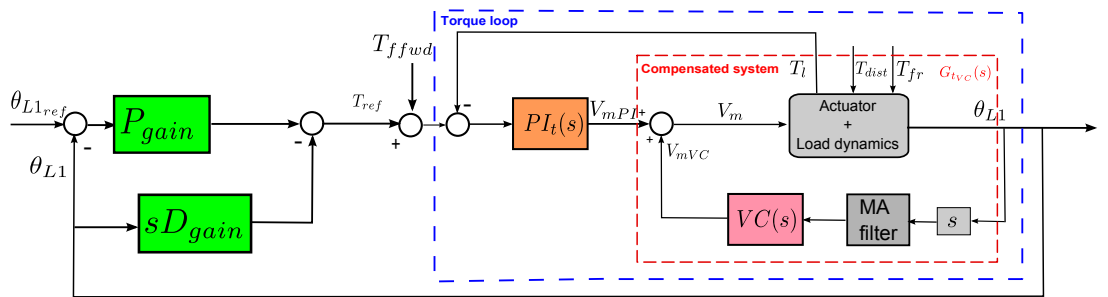


Figure 4.1: Block diagram of the compensated system with inner torque loop (orange) and outer impedance loop (green).

the effects of gravity or perform inverse dynamics (this is a must to get good locomotion performances). We need to remark that, for the sake of simplicity, we introduce the concepts (controller, transfer functions) in continuous time. However, the consequent analysis will be

4.1. Impedance control for the adduction/abduction joint

always carried out in discrete time, because only there the limitations dependent on the sampling time become visible.

For HyQ, a range of values for the impedance loop gains that is considered to be sufficient for walking, trotting and running tasks is $P_{gain} \in [0, 20000] Nm/rad$ and $D_{gain} \in [0, 50] Nms/rad$. These ranges have been determined tailoring the concepts presented in Section 4.2.3 to suit our robot inertia. However, we point out that P_{gain} and D_{gain} are in *joint space* while later in Section 4.2.3 we will discuss about *task-space* impedance gains.

4.1.3 Stability regions

In this Section we will use the three inertia model, presented in 3.5, to determine the closed loop stability region for a given range of impedance parameters P_{gain} and D_{gain} by varying the torque loop control bandwidth (β) (see definition in (3.27)), the velocity compensation gain α (see definition in (3.25), the number of samples (N_{av}) used in the MA averaging filter of the link velocity and the sampling time interval(T_s). For practical reasons, as explained in Section 3.6, we linked the torque loop bandwidth to the parameter β which enables to change simultaneously the integral and proportional gain of the PI torque controller. The analysis is performed in discrete time, by varying the stiffness P_{gain} between 1 and 20000 Nm/rad and the damping D_{gain} between 1 and 50. The stability of the overall system is determined by computing the closed loop eigenvalues and checking that they are inside the unit circle (stability boundary in discrete time). In addition when closed loop stability is attained, the region where the phase margin is less than 30 degrees is also determined. These calculations were carried out in *Matlab* using the mathematical model presented in Section 3.5.

The results are displayed in Figs. 4.2, 4.3, 4.4 and 4.5 where the white area corresponds to the stable region; light grey is a stable region with a phase margin of less than 30 degrees and the dark area is the unstable region. In the analysis all the regions have been computed for the leg in stretched configuration $J_{L2} = 0.439$ unless it is otherwise stated.

Fig. 4.2 shows that, as the torque controller gain increases, the unstable region for low stiffness and damping reduces but the unstable region for large stiffness and/or large damping increases. This clearly illustrates that increasing the torque loop bandwidth may not be consistent with the requirements for the outer impedance loop. From Figs. 4.3 (a), (b) and (c) it is clear that increasing the velocity compensation results in an increasing instability region. Once more this gives further evidence that as the torque loop bandwidth increases (an increasing velocity compensation gain increases the torque bandwidth as shown in table 3.4), the performance of the outer loop may become unstable. For low leg inertia configuration in Fig. 4.3 (d) the instability region for low damping and low stiffness increases but the unstable

4. IMPEDANCE CONTROL

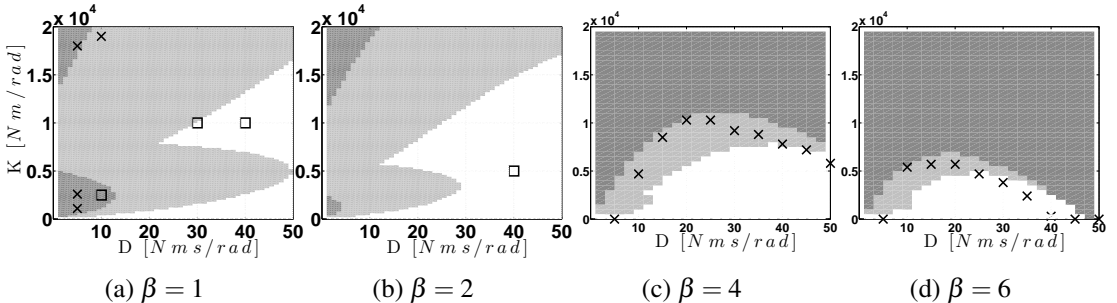


Figure 4.2: Stability regions varying the torque controller gain β (keeping $\alpha = 0.94$, $N_{av} = 4$ and $T_s = 1ms$). White area corresponds to the stable region; light grey is a stable region with a phase margin of less than 30 degrees and the dark area is the unstable region. Crosses and squares denote unstable and stable experimental points respectively.

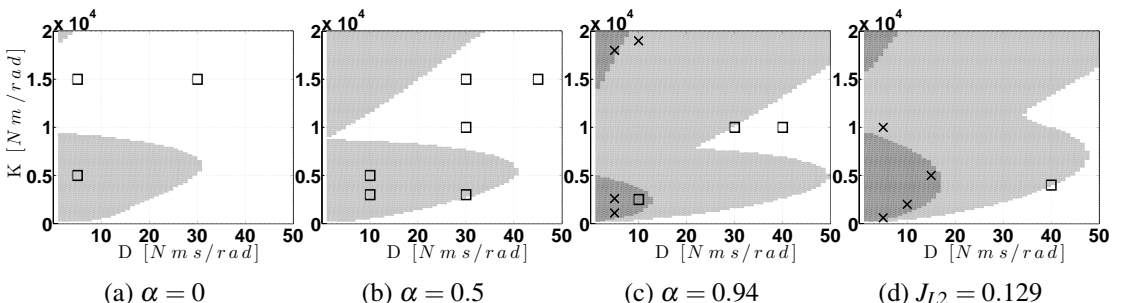


Figure 4.3: (a),(b),(c) Stability regions varying the velocity compensation gain α (keeping $\beta = 1$, $N_{av} = 4$ and $T_s = 1ms$). (d) Stability region for retracted leg (lower inertia) $J_{L2} = 0.129$ (with $\beta = 1, \alpha = 0.94$, $N_{av} = 4$ and $T_s = 1ms$). White area corresponds to the stable region; light grey is a stable region with a phase margin of less than 30 degrees and the dark area is the unstable region. Crosses and squares denote unstable and stable experimental points respectively.

region reduces for low damping and large stiffness. The region with a phase margin smaller than 30 degrees is also larger for the low inertia configuration. The effects of increasing the number of samples in the averaging filter are shown in Fig. 4.4. Averaging a large number of samples enlarges the instability region for low stiffness values but the unstable region for high stiffness and low damping reduces in size. Also using the torque compensator (not shown in the figures) even if from one side improves the torque tracking from the other reduces the size of the stability region. Figure 4.5 clearly shows that for a large sampling time interval the region for instability is the largest for low damping and stiffness. Reducing the sampling time T_s creates an additional instability region for low damping and high stiffness but the region for low damping and low stiffness reduces in size. The region where the phase margin is less than 30 degrees also increases as the sampling time increases.

4.1. Impedance control for the adduction/abduction joint

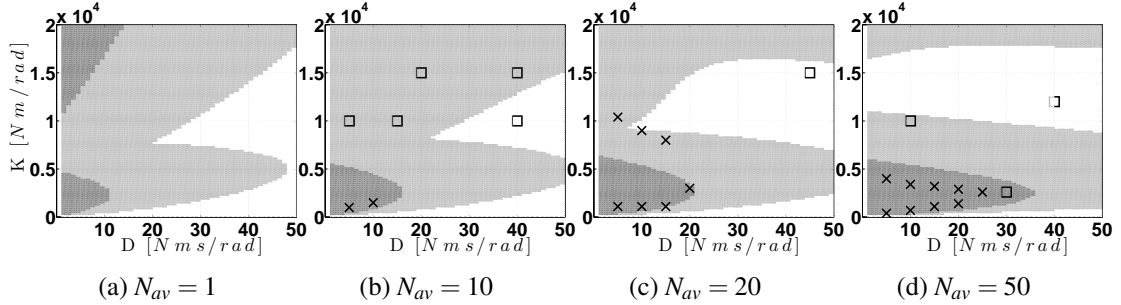


Figure 4.4: Stability regions varying number of samples N_{av} of the link velocity filter (keeping $\beta = 1$, $\alpha = 0.94$ and $T_s = 1ms$). White area corresponds to the stable region; light grey is a stable region with a phase margin of less than 30 degrees and the dark area is the unstable region. Crosses and squares denote unstable and stable experimental points respectively.

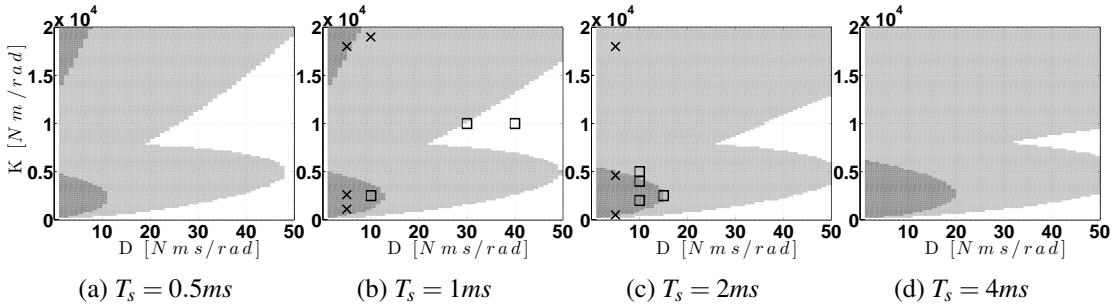


Figure 4.5: Stability regions varying the sampling times T_s (keeping $\beta = 1$, $N_{av} = 4$, $\alpha = 0.94$). White area corresponds to the stable region; light grey is a stable region with a phase margin of less than 30 degrees and the dark area is the unstable region. Crosses and squares denote unstable and stable experimental points respectively.

To determine the stability regions experimentally is not an easy task because it would involve a very large number of experiments. Even only finding the stability boundaries is not a simple task. Several experimental tests were carried out to validate the analytic results predicted by the model. The adopted methodology was to start from values P_{gain} and D_{gain} well inside the stable region and change the parameters in small steps until the instability was triggered. This enabled us to get a rough idea of the stability boundary. The experimental results are displayed together with the analytic one in Figures 4.2, 4.3, 4.4 and 4.5, where crosses and squares denote unstable and stable points respectively. Overall the experimental tests are consistent with the analytic calculations. Figures 4.2 (b), 4.3(a), 4.3(b) and 4.4(b) are fully in agreement with the theoretical results. For test points near the stability boundaries inconsistencies are present suggesting that the model lacks accuracy from a quantitative point of view but qualitatively it is correct.

4. IMPEDANCE CONTROL

4.1.4 Passivity analysis

In this section we will introduce an important concept (passivity) that is a desirable property to ensure closed-loop stability of the system when interactions with passive environments or other passive systems occur. It is well-known that a strictly passive system, connected to any passive environment, is necessarily stable [Colgate and Hogan, 1989]. Thus, since most terrain surfaces are passive, to ensure a stable contact with the environment it is desirable that the robot behave as a passive system. Now joints are made of actuators and rigid bodies and compliant elements. Physical compliant elements and rigid bodies are passive by nature. This is not always the case when compliance is obtained actively, where the compliant behavior is emulated by controlled actuators. In this case, the controller gains can destroy passivity. If the purpose is to always preserve stability during the interaction a useful but conservative solution is to design a controller in a way such that the system behaves *passively* at the interaction port [Colgate and Hogan, 1989].

The requirement to ensure this type of stability for the robot interacting with the environment is the following: the robot driving port impedance or admittance has to be passive. Driving port impedance/admittance is the impedance/admittance seen at the point where the robot makes contact with a passive environment. For linear time invariant systems this is a necessary and sufficient condition, but it is only a sufficient condition for nonlinear systems. Let $Z(s)$ denote the driving port (output) impedance transfer function. The output impedance is the amount of force/torque at the actuator output give a moving in load position. Since in the model (3.18) we have the load disturbance torque T_{dist} as input while θ_{L1} is a state variable, to find the impedance we compute the transfer function from the load disturbance T_{dist} to the link position θ_{L1} (admittance) and then do the reciprocal (this is possible because we are considering a linearized system while it does not hold for non-linear systems). Then $Z(s)$ is passive if and only if it is positive real [Anderson and Vongpanitlerd, 2006]. In [Colgate, 1994] and [Colgate, 1986] it has been shown that this is equivalent to:

1. $Z(s)$ has no poles in $\Re(s) > 0$;
2. the phase of $Z(s)$ lies between 0 and 180 degrees.¹

For sampled data (discrete) control systems, [Colgate, 1994] has suggested an approximate method based on computing the corresponding discrete time transfer function matrix $Z(z)$, assuming that the port of interaction is also sampled. The phase of $Z(z)$ is computed and corrected

¹Colgate defines impedance as the relationship between an output force produced by an input velocity. The passivity property is ensured if the phase lies between -90 and +90 degrees. In this work we chose to define impedance as the transfer function between position and force/torque, therefore the previous requirement ha been changed accordingly (the phase of $Z(s)$ must lie between 0 and 180 degrees).

4.1. Impedance control for the adduction/abduction joint

by adding $\omega T_s 0.5$ at each frequency, where T_s is the sampling time interval. Although many studies have been carried out for analyzing the passivity of sampled-data systems [Colgate and Schenkel, 1997], there is still a lack of information about the influence of the closed-loop torque control bandwidth on the combinations of stiffness and damping that can be passively rendered (in haptics called *Z-width*) [Colgate and Brown, 1994]. Therefore, this section will show that the torque loop performance plays an important role on the range of achievable impedance values for which the interaction port is *passive*.

Analogously to the continuous case, the discrete time impedance $Z(z)$ has been computed as the reciprocal of the transfer function from the load disturbance T_{dist} to the link position θ_{L1} for the sampled system. For the sake of brevity extensive results will not be shown as in Section 4.1.3 but it will be reported only the results obtained from the sensitivity analysis carried out for three cases. Namely the transfer function $Z(z)$ has been computed for the torque loop alone with velocity compensation and for the whole system with the outer impedance loop by setting low ($P_{gain} = 200, D = 10$) and high ($P_{gain} = 2000, D = 50$) impedance parameters. Subsequently the analysis of passivity has been repeated by varying several parameters to have a better understanding of their influence: the gain of the PI torque controller β , the velocity compensation gain α , the sampling time T_s , and the number of samples N_{av} of the MA averaging filter of the link velocity. For each set of parameters the analysis was performed first checking the stability of $Z(z)$ and then verifying that the corrected phase of $Z(z)$ was in the range $0 - 180^\circ$ for frequencies up to the Nyquist frequency (500Hz). If these conditions are not satisfied then $Z(z)$ is not passive for the particular set of parameter values. The results of this analysis are summarized in Table 4.1. The nominal set of parameters that are not changing are: $\alpha = 0.94$, $N_{av} = 4$ samples, leg inertia $J_{L2} = 0.439$, $P_t = 0.38$ and $I_t = 18$.

As the results in the following table show, the overall (impedance + torque loop) system is always passive for low impedances $P_{gain} = 200 \quad D_{gain} = 10$ while passivity might be destroyed when the torque controller gain β (and so the torque bandwidth) increases or the sampling frequency decreases. In particular it can be noticed that when the torque gain is larger than or equal to 4 the closed loop system with the position loop becomes unstable. This is a clear indication that increasing the bandwidth of the torque loop is not always consistent with the requirements of the outer loop. When only the torque loop is closed the discrete time system is almost never passive except that for low values of α . The table shows that the velocity compensation is the key parameter affecting the passivity if the torque loop alone is considered. In particular when the amount of velocity compensation increases, the inner torque loop becomes not passive and therefore the torque control system alone can become unstable when the leg interacts with the environment. Finally the use of the torque compensator designed in Section 3.7 destroys the passivity of the system when only the torque loop is closed while keeping it for

4. IMPEDANCE CONTROL

Table 4.1: Passivity

	Torque loop (alone)	Impedance loop $P_{gain} = 200$	Impedance loop $P = 20000$
		$D_{gain} = 10$	$D = 50$
$\beta = 1$	No	Yes	Yes
$\beta = 0.5$	No	Yes	No
$\beta = 2$	No	Yes	No
$\beta = 4$	No	Yes	Unstable
$\beta = 6$	No	Yes	Unstable
$\alpha = 0$	Yes	Yes	Yes
$\alpha = 0.5$	Yes	Yes	Yes
$T_s = 4 \cdot 10^{-3}[s]$	No	Yes	No
$T_s = 2 \cdot 10^{-3}[s]$	No	Yes	No
$T_s = 0.5 \cdot 10^{-3}[s]$	No	Yes	Yes
Averaging $N_{av} = 1$	No	Yes	Yes
Averaging $N_{av} = 10$	No	Yes	Yes
Averaging $N_{av} = 20$	No	Yes	Yes
Averaging $N_{av} = 50$	No	Yes	Yes
Low Inertia $J_{L2} = 0.129$	No	Yes	Yes
With torque compensator	No	Yes	Unstable

low impedance and again making the system unstable for high impedances. It is worth pointing out that the performed analysis is conservative because is done on the linearized system (about $\theta_{L1} = \theta_{L2} = 0$ operating point) and the fact the linearized system is passive is a sufficient condition for the non-linear to be passive as well. Further analysis showed that the system becomes unstable if the leg is in contact with an environment with a stiffness K_{L2} between $72Nm/rad$ and $3500Nm/rad$. This has been verified with experimental tests using the experimental arrangement depicted in Fig. 4.6 where the leg base is rigidly fixed to the ground. The experiment has been carried out in the following way: first, a $0Nm$ constant torque reference is given for which, under the effect of the gravity, the leg settles down to a vertical ($\theta_{L1} = 0$) resting position. Then a $5Nm$ torque step is set to the torque reference that would make the leg move until hitting a passive linear spring. The distance of this linear spring from the HAA axis can be adjusted to artificially obtain a certain rotational stiffness K_{L2} . If the stiffness K_{L2} is well inside the range $72Nm/rad$ and $3500Nm/rad$ the leg starts to "bounce" on the spring showing an instability behaviour. For stiffness K_{L2} out of this range the interaction is stable and the torque attains the $5Nm$ reference signal.

4.1. Impedance control for the adduction/abduction joint



Figure 4.6: Setup for passive tests. The rotational stiffness K_{L2} is obtained by positioning a linear spring at a certain distance from the HAA axis.

4.1.5 Rejection of the torque ripple in the impedance loop

The problem of the torque disturbances introduced by the harmonic drive was initially addressed in the previous chapter by designing an additional torque compensator, based on the idea of a notch filter, that give some improvements. In this section we will carry out an analysis to see how the effects of this torque disturbance may be reduced when the outer impedance loop is closed. In particular we will show that increasing the bandwidth of the inner torque loop will reduce the effects produced by this disturbance. To start we will carry out the analysis of the controlled system with the inertia of the leg retracted $J_{L2} = 0.129 \text{ kgm}^2$, $\alpha = 0.94$ and low impedance gains ($P_{gain} = 200$ and $D_{gain} = 10$). Fig 4.7 shows the frequency response of the transfer functions of the torque ripple T_{fr} to torque T_l . The torque peak occurs at around 15 Hz. A similar bode diagram (not reported), computed considering the position as output, showed that the influence of the disturbance is much higher for the torque than for the position. This is expected because the position profits of the beneficial filtering effect of the load inertia.

Since we have two loops are present, we want to investigate which is the impact of increasing the inner loop bandwidth on the disturbance rejection. In the upper plot is set a gain $\beta = 1$ of the PI torque controller while in the lower plot a higher gain $\beta = 10$ (higher torque bandwidth) and lower gains in the impedance controller. We chose to carry out this analysis for low impedance gains because, for high impedances if we set $\beta = 10$, thanks to the insights gained from Fig. 4.2, we know the system is unstable. Using $\beta = 10$ the torque disturbances get always lower amplitudes, having a significant reduction in the mid frequency region from

4. IMPEDANCE CONTROL

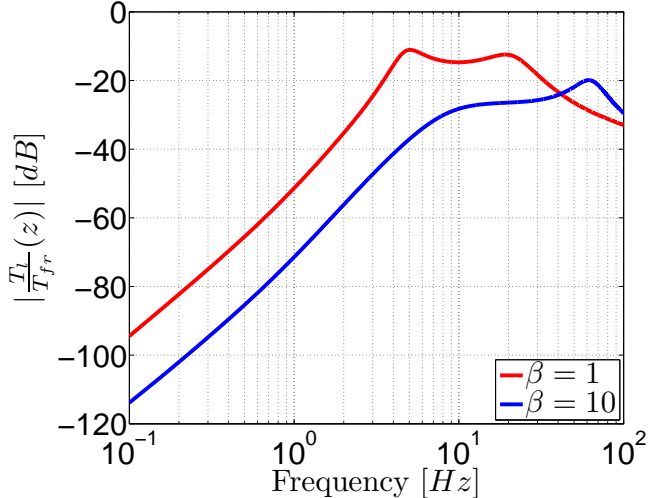


Figure 4.7: Bode diagram (magnitude) of the transfer functions from friction torque disturbances $T_{fr}(s)$ to torque $T_l(s)$ after closing the outer impedance loop ($P_{gain} = 200$ and $D_{gain} = 10$). The red line shows the response for $\beta = 1, P_{gain} = 2000, D_{gain} = 50$ while the blue line for $\beta = 10$. The friction torque amplitude is 0.013Nm and this is included in the bode plots.

10 to 35 Hz. A 20 dB attenuation is anyway ensured for the resonance above 60 Hz. This clearly shows that increasing the bandwidth of the inner torque loop reduces the effects of the torque ripple in the drive. This is as expected, since this is one of the objectives of the nested loop design when maximizing the bandwidth on the inner loop. The trade-off in this case is that we cannot use large impedance gains because the closed loop system becomes unstable (see 4.1.3). Therefore the range of impedances that can be implemented is reduced.

4.1.6 Impedance tracking

From control system theory we know that a generic reference input can be tracked well only in a certain frequency range. The same idea holds if the reference input is not a reference signal but a "dynamic response" between position and load disturbances: which is the desired impedance. Impedance tracking essentially means how well the impedance is emulated by the controller from the point of view of an external perturbation. That is equivalent to say that the target impedance should be compared to the actual load impedance (that is the torque/forces that are produced by changes in load position). The actual load impedance is the inverse transfer function from the load torque disturbance T_{dist} to load position θ_{L1} . These are respectively the effort and flow [Hogan, 1985] variables of the *driving* port by which the robot interacts with

4.1. Impedance control for the adduction/abduction joint

some passive environment or another system.

The target impedance is specified by a first or second order polynomial, $P_{gain} + D_{gain}s$ or $P_{gain} + D_{gain}s + J_{gain}s^2$ (and for discrete time systems $s = T_s^{-1}(z - 1)$, where T_s is the sampling time interval). Therefore for a high order system (like ours), we cannot achieve good impedance tracking above a "critical" frequency. This fact has to be taken into account when comparing the target impedance to the real impedance. In some cases only the low frequency region (where stiffness is dominant) may be important. Being aware of which is the maximum frequency up to which the impedance is properly rendered is very important when designing locomotion task requirements. By using the model with three inertia (computed for the retracted leg inertia $J_{L2} = 0.129$), we can perform analysis without having to carry out complex and time-consuming experiments. In the discussion below only the amplitude bode plots have been considered.

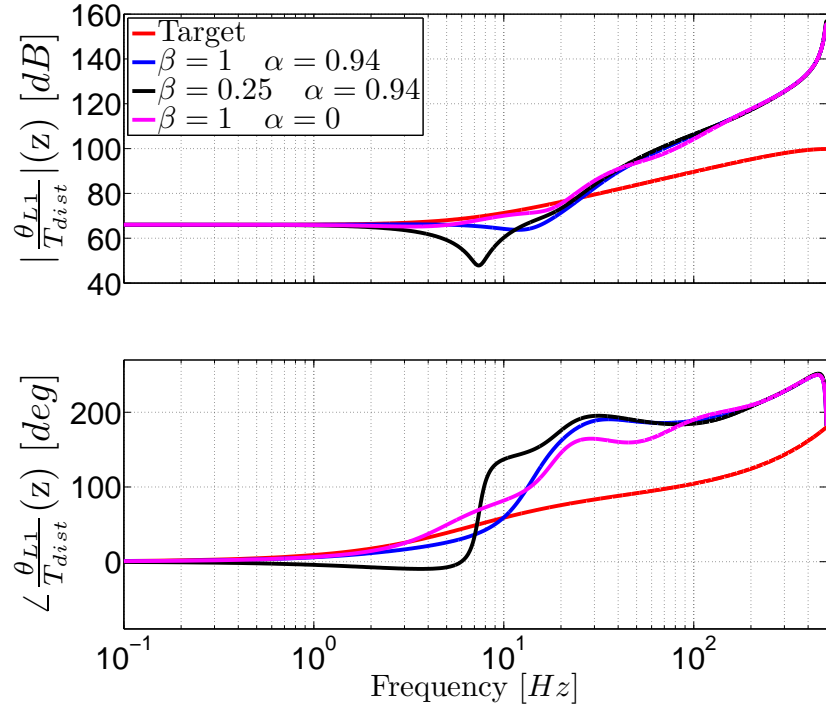


Figure 4.8: Bode diagram of the load impedance (high impedance gains). Target impedance ($P_{gain} = 2000, D_{gain} = 50$) (red) and load impedance computed for $\beta = 1$ (blue), $\beta = 0.25$ (black) with $\alpha = 0.94$ and for $\beta = 1$ with $\alpha = 0$ (magenta).

Figure 4.8) is the bode diagram of the target (high gains $P_{gain} = 2000, D_{gain} = 50$) and real impedance. Real impedance is computed in different cases: $\beta = 1, \beta = 0.25$ with $\alpha = 0.94$

4. IMPEDANCE CONTROL

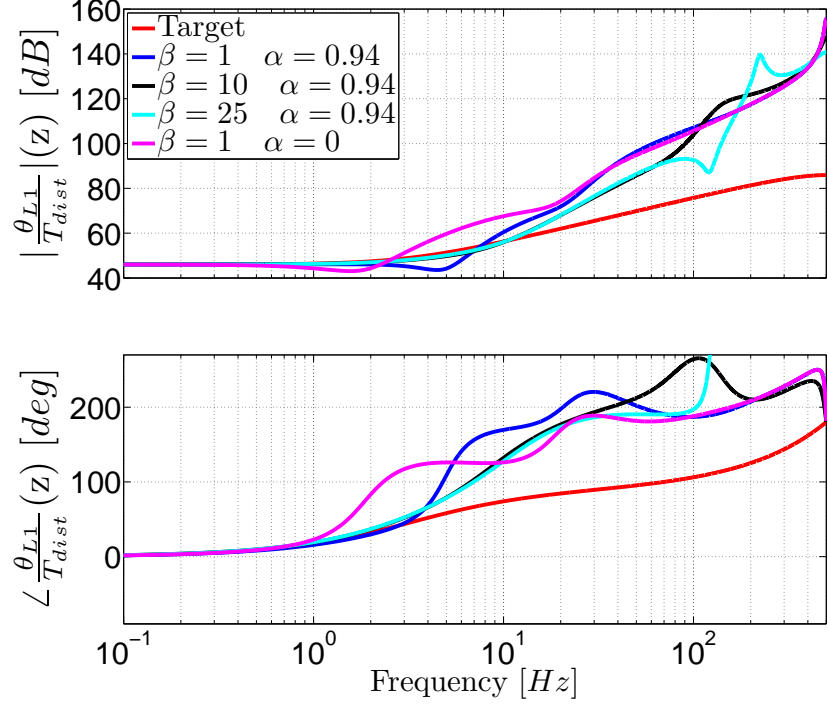


Figure 4.9: Bode diagram of the load impedance (low impedance gains). Target impedance ($P_{gain} = 200$, $D_{gain} = 10$) (red) and load impedance computed for $\beta = 1$ (blue), $\beta = 10$ (black) with $\alpha = 0.94$ and for $\beta = 25$ with $\alpha = 0$ (magenta).

and $\beta = 1$ with $\alpha = 0$. We first notice that the real impedance in most cases is almost constant up to 5 Hz while the desired impedance starts increasing after 1 Hz. After 20 Hz we can see that the real impedance has larger amplitude compared to the target impedance. This is because the target impedance does not have a second order factor and the real system has order much larger than two. In this frequency region (1 – 20Hz) impedance tracking will not be possible. The question we pose is: can we achieve an improvement in tracking the target impedance in the mid frequency region, between 1 to 20 Hz, by increasing the bandwidth of the inner torque loop? For the case of high impedance parameters the answer is no, because we cannot increase too much the bandwidth of the inner loop due to instability. To further probe this question, by setting the velocity compensation to zero (this substantially reduces the inner torque loop bandwidth) noticeably improves the impedance tracking, see Fig 4.8). Therefore, in general we cannot state that a high bandwidth torque loop leads to better impedance tracking. Conversely, reducing the gain of the inner torque loop ($\beta = 0.25$) degrades the impedance tracking performance, see black plot in Fig 4.8). Therefore, to achieve a minimum level of

4.1. Impedance control for the adduction/abduction joint

performance, there seems to be a lower bound for the inner loop torque bandwidth. Does this behavior also occur for different target impedances? To answer this question we have reduced the impedance gains ($P_{gain} = 200$, $D_{gain} = 10$) and the results are shown in Fig. 4.9). For lower impedance parameters setting the velocity compensation to zero degrades impedance tracking. With the velocity compensation set to $\alpha = 0.94$, by increasing the torque loop PI gain (β) from 1 to 10 improves the impedance tracking but increasing further the PI gain ($\beta = 25$) does not yield further improvements in impedance tracking. Also note that for lower impedance parameters after $10Hz$ we can see that the real impedance becomes much larger compared to the target impedance. These results demonstrate that it is quite difficult to make generic statements regarding the inner torque loop bandwidth effects on impedance tracking.

What we can say about the statement that a high bandwidth torque loop leads to better impedance tracking in general is incorrect. The only conclusion we can derive is that there is a lower bound in the bandwidth that is required for the inner torque loop for tracking the impedance in a specified frequency region. Indeed, increasing the inner torque loop bandwidth above certain value does not improve the impedance tracking. The reason for this is that at high frequencies a high order system cannot be made to behave as a first or second order system ($P_{gain} + D_{gains} + J_{gains}s^2$). Note however that if the inner torque loop bandwidth is too low then impedance tracking is only good at low frequencies (impedance control becomes stiffness control). Increasing the bandwidth of the inner torque loop will improve impedance tracking in the mid frequency region until it reaches a "critical" frequency where further improvements cannot be achieved. This limit is related to the inertial effects of the load that after a certain frequency start to dominate. This limits are intrinsic to the system and will not change even if an actuator with higher open loop bandwidth is employed. Therefore a practical rule of thumb to design a controller does not exist and an extensive analysis like the one performed the above sections is necessary to be able to find out, given the desired impedance, which are the maximum range of frequency in which it can be emulated and verify if the initial locomotion specifications are satisfied.

4.1.7 Torque tracking with outer impedance loop

As we have shown in the previous sections, considering the nested loops in isolation leads to incorrect conclusions because the dynamics of the loops have mutual influences. Whenever there is an outer loop, to see the effect of velocity compensation, we need to consider not only the torque loop but also the influence of the outer loop. In this section we will show that the bandwidth of the torque controller changes when the outer impedance loop is closed. In particular the quality and dynamics of the torque tracking is mainly dependent on the impedance

4. IMPEDANCE CONTROL

parameters and not anymore on the torque PI controller. This is because the outer loops affects the torque tracking ability of the inner loop. We will demonstrate this concept by addressing the implementation of gravity compensation with impedance control. Indeed a common problem that roboticists face when implementing impedance control algorithms is the steady state (position) error introduced by gravity. A way to overcome this issue, if a inner torque loop is available, is to add a feed-forward term T_{ffwd} to the output T_{ref} of the impedance controller in order to compensate for the gravity torque (see Fig. 4.1).

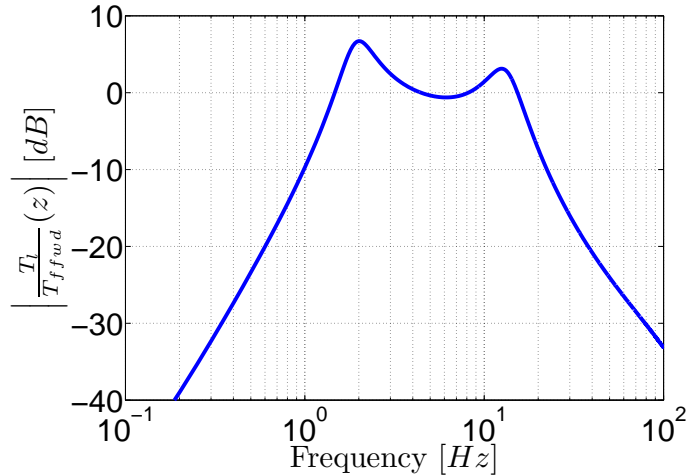


Figure 4.10: Bode diagram (magnitude) of the transfer functions between $T_{ffwd}(z)$ and $T_l(z)$ when the outer impedance loop is closed.

Fig.4.10 shows the torque response to a reference torque T_{ffwd} added at the output of the impedance controller. Clearly this figure shows that the torque response T_l does not track the reference torque input T_{ffwd} in the usual meaning of tracking. In fact the response is strongly attenuated for all the frequencies below 1.5 Hz and there is no frequency region where the magnitude ever achieves an unitary gain (except for the intermediate region 4.5-8.5 Hz). This is evidence that the interpretation that the closed loop system tracks feed-forward torques is in general incorrect.

So what does a torque T_{ffwd} do? The torque loop itself does not track any signal added at this point. However, any feed-forward torque added at to the output of the impedance loop T_{ref} can have the effect of compensating for errors in the position created by torque disturbances on the load. For example gravity will induce an error in the position, but adding a torque to compensate for gravity at the output of the impedance loop prevents the position error occurring. The impedance controller does not have to provide a torque to counteract gravity because

4.2. Impedance control for the whole leg

this has been added by the user and therefore the output of the impedance loop can become quite small and will be reacting only to the position errors caused by external forces according to the desired impedance. This, in the end, results in an improvement of the tracking of the impedance.

4.1.8 Summary

In this section has been presented the implementation of an impedance loop with an inner torque loop for the *HAA* joint. Nested loops is a suitable control architecture (indeed this occurs naturally in many physical systems). What is not suitable is the traditional approach for designing a nested loop control system (i.e. maximizing the bandwidth of the inner loop). In particular has been shown that increasing the bandwidth of the inner torque loop decreases the region of impedance parameters for which the system is stable (*stability region*). On the other hand if the bandwidth is too low the range of frequency in which the impedance is reasonably tracked, is reduced. Increasing the bandwidth improves impedance tracking in the mid frequency region until it reaches a "critical" frequency where further improvements cannot be achieved. This limit is related to the inertial effects of the load that after a certain frequency start to dominate. Therefore, a trade-off must be found between different requirements: having a reasonably high bandwidth to ensure good impedance tracking, and keeping the bandwidth low to increase the range of stable impedance values that can be rendered.

The region of stable impedance parameters is also affected by the delay introduced by averaging filters (e.g to filter velocity signal) or sampling time. From a controlling point of view, stability regions ensure the stability of the system where there is no contact with the environment. However, a system that is stable can become unstable whenever interacting with a certain kind of environment. The property that ensures the stability of the system also during the interaction is passivity that is more strict than just stability. An analysis of the passivity of the system showed that the torque loop alone is never passive except that for very low value of the velocity compensation gains. Conversely when the outer impedance loop is closed, the overall system is always passive for low impedances while passivity might be destroyed when the torque bandwidth increases or the sampling frequency decreases.

4.2 Impedance control for the whole leg

The implementation described in [4.1.2](#) it was for a single (*HAA*) joint, while to be able to control the impedance of the whole leg it is necessary to consider all the joints of the leg at the same time. In this section two different implementations of an impedance controller for the

4. IMPEDANCE CONTROL

whole leg will be described: the first by defining the impedance in the joint space, the second in the task-space.

4.2.1 Joint space implementation

A joint space impedance controller can be trivially obtained extending the (4.1) to the vectorial case where we consider all the 3 joints of the leg. Vectorial variables will be henceforth marked bold.

$$\boldsymbol{\tau}_{lref} = \boldsymbol{K}_\theta(\boldsymbol{q}_{ref} - \boldsymbol{q}) + \boldsymbol{D}_\theta(\dot{\boldsymbol{q}}_{ref} - \dot{\boldsymbol{q}}) \quad (4.2)$$

where $\boldsymbol{\tau}_{lref}$ is the 3×1 vector of the desired actuation torques to be sent as reference to the lower-level torque controllers of each actuator (see Fig. 4.11). $\boldsymbol{q}, \boldsymbol{q}_{ref}, \dot{\boldsymbol{q}}, \dot{\boldsymbol{q}}_{ref}$ are the 3×1 vectors of the actual and desired link positions and velocities, and \boldsymbol{K}_θ and \boldsymbol{D}_θ are the joint stiffness and damping matrix, respectively:

$$\boldsymbol{K}_\theta = \begin{bmatrix} P_{gain_{HAA}} & 0 & 0 \\ 0 & P_{gain_{HFE}} & 0 \\ 0 & 0 & P_{gain_{KFE}} \end{bmatrix} \quad \boldsymbol{D}_\theta = \begin{bmatrix} D_{gain_{HAA}} & 0 & 0 \\ 0 & D_{gain_{HFE}} & 0 \\ 0 & 0 & D_{gain_{KFE}} \end{bmatrix} \quad (4.3)$$

where P_{gain_i} and D_{gain_i} are the stiffness and damping for the joint i . Henceforth bold variable are vector variables.

The block diagram in Fig. 4.11 shows a schematic of the joint space impedance controller for the HyQ leg. The vector $\boldsymbol{\tau}_{ref}$ computed by the outer impedance controller is sent as a reference to the inner torque loops. If the (4.2) is implemented, this will result, at the end-effector, in an impedance that is configuration dependent and therefore non-constant during the motion. This can be graphically shown (Fig. 4.12) by plotting the stiffness ellipsoid at the end-effector for different leg configurations (we decide to consider the stiffness ellipsoid because it is more meaningful in static cases but the same discussion holds for the damping ellipsoid). Indeed, a stiffness matrix can be graphically represented by a stiffness ellipsoid [Mussa-Ivaldi et al., 1985] that can be generated computing eigenvalues and eigen-vectors of the stiffness matrix. The stiffness ellipsoid gives an idea of the force direction and modulus in consequence of a displacement(unitary) in a certain direction. In Fig 4.12 two different stiffness ellipsoids computed at the end-effector are represented for the leg in a stretched and retracted configuration. The major and minor axis represent the directions (eigen-vectors) where the stiffness is maximum and minimum respectively. In particular the major and minor axes lengths

4.2. Impedance control for the whole leg

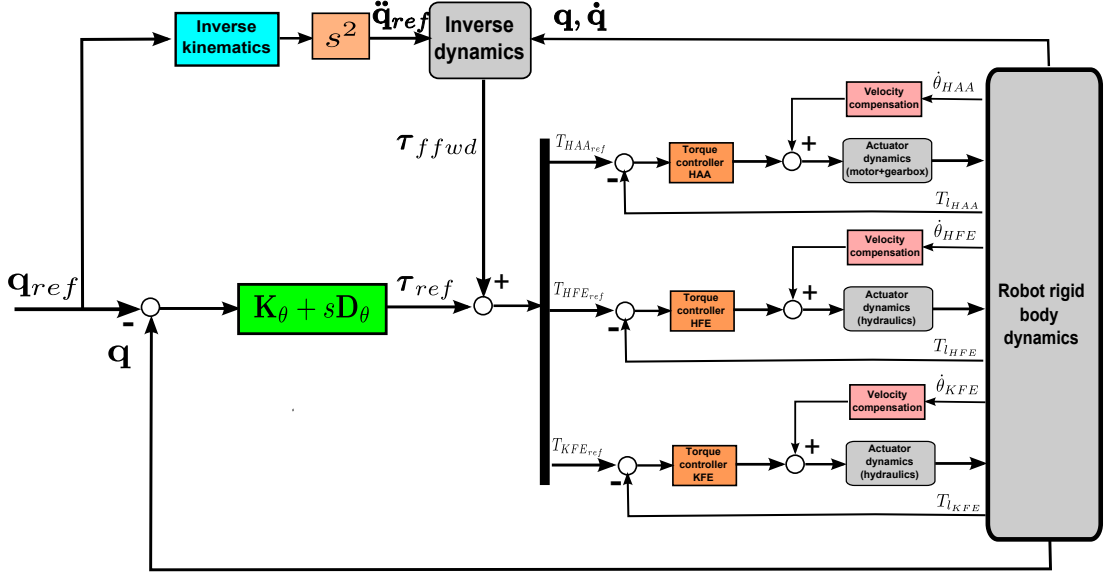


Figure 4.11: Block diagram of the joint-space impedance controller implemented for the HyQ leg.

are the eigenvalues of the stiffness matrix.

Fig. 4.12 shows that in the stretched configuration the dominant stiffness is in the Z direction while in a retracted configuration it the dominant stiffness is in the X and Y direction. We will show in the following section that implementing the leg impedance in a frame which is aligned with the robot base, allows to obtain stiffness ellipsoids whose principal axes are always aligned with X, Y and Z directions of the robot base and that are not changing with the leg configuration. For the definition of the base frame please refer to Fig. 2.7. This is of great importance because enables the robot to have the same dynamics (impedance) when interacting with the ground during locomotion, independent of what is the configuration the stance legs are in the moment of touch-down.

4.2.2 Task space implementation

In this section we present the implementation of the leg impedance in the end-effector space.

4.2.2.1 Motivation

In fact, it is reasonable to specify impedance at the point where the interaction occurs, which in the case of the HyQ robot, is the end-effector. Furthermore locomotion requirements and foot trajectories are also planned at the end-effector level (task space). This means that the

4. IMPEDANCE CONTROL

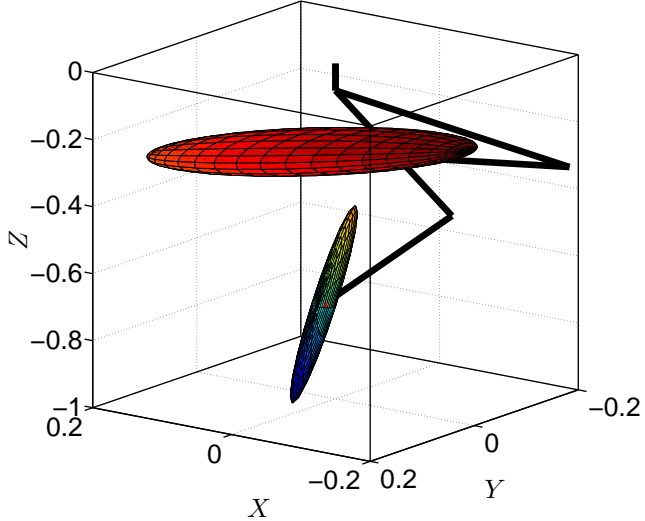


Figure 4.12: Stiffness ellipsoids at the end effector computed for the leg (links are colored in black) in stretched and retracted configuration, with impedance control implemented joint space (diagonal stiffness matrix). This will map in a configuration dependent stiffness at end-effector.

robot has to be able to suitably track these, disregarding the joint space. As anticipated another desirable feature is that controlling the impedance at the end-effector makes this invariant with the robot configuration. In addition the end-effector impedance can be defined in a frame which is aligned with the robot base frame. This can be useful, for instance, during locomotion to obtain ground forces which are more "vertical". For instance, the dominant force during slow trot is the gravity. Gravity force will act on the robot body creating a downward motion that will result in a static error in the Z (vertical) coordinate of the stance feet positions.

Conversely, having a diagonal stiffness matrix at the end-effectors defined in a frame aligned with the robot base frame, enables to generate forces that are collinear with the displacements. In particular the ground reaction forces will be vertical because the controller will generate vertical forces in response to the vertical foot displacements. Having a joint space impedance controller would result in forces that are not vertical but aligned with the stiffness ellipsoids major axis (see Fig. 4.12). Figures 4.13 are generated with the SL simulator [Schaal, 2009] and show ground reaction forces (blue lines) when the robot is standing still on the floor. The left figure shows that these forces are perfectly vertical if the impedance control is implemented in the task-space space. In the case the controller is implemented in the joint space (right figure) internal forces are generated that have horizontal components acting between the end effectors. Having ground reaction forces as much as possible vertical is desirable be-

4.2. Impedance control for the whole leg

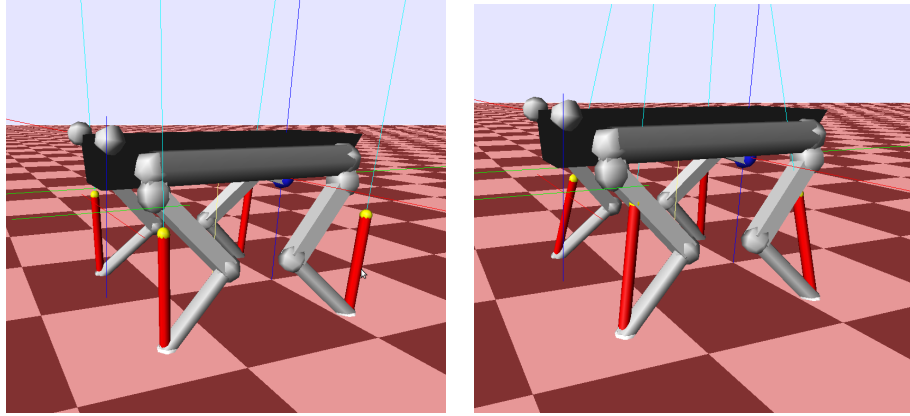


Figure 4.13: Comparison of ground reaction forces with the robot standing still on the ground in case of impedance controller implemented at the end-effector (task) space (left) and at the joint space (right). In the latter case these force are not vertical.

cause it enables to reduce the chance of slippage during locomotion. This becomes crucial when the robot is negotiating very slippery surfaces. However, this holds if the Z direction of the base of the robot is aligned with gravity. During normal locomotion the orientation of the base changes due to roll and pitch motions. Therefore, if the angular posture measurements of the body are available (e.g. by an IMU sensor), it is possible to define the stiffness matrix in an inertial frame. This allows to have always a similar body dynamics when the robot is negotiating the ground independently by the body orientation.

4.2.2.2 Implementation

The fundamental philosophy of implementing the impedance controller at the end-effector is to define a dynamic relationship $\mathbf{Z}(z)$ (impedance) between the end-effector Cartesian position \mathbf{x} (i.e. the foot of the robot) and the Cartesian interaction forces \mathbf{F}_{int} applied on the robot by the environment [Hogan, 1985].

$$\frac{\mathbf{F}_{int}}{\mathbf{x}} = \mathbf{Z}(z) \quad (4.4)$$

In particular if the environment is applying a certain interaction force \mathbf{F}_{int} to the end-effector, this will map as interaction torques $\boldsymbol{\tau}_{int} = \mathbf{J}(\mathbf{q})^T \mathbf{F}_{int}$ on the robot joints. Where $\mathbf{J}(\mathbf{q})$ is the leg Jacobian. These interaction torque will generate joint accelerations and displacements according to the robot leg dynamics:

$$\mathbf{M}_{\theta} \ddot{\mathbf{q}} + \mathbf{h}(\mathbf{q}, \dot{\mathbf{q}}) = \boldsymbol{\tau} + \mathbf{J}(\mathbf{q})^T \mathbf{F}_{int} \quad (4.5)$$

4. IMPEDANCE CONTROL

where \mathbf{M}_θ is the joint space inertia matrix and \mathbf{h} the vector of joint torques representing centrifugal/coriolis/gravity forces and $\boldsymbol{\tau}$ is the vector of actuating torques. The aim of a task-space impedance controller is to create torques $\boldsymbol{\tau}$ that, if mapped back to the end-effector, will result in forces \mathbf{F}_{ref} that respect a certain dynamic relationship (e.g. spring-damper) with the deflection of the actual end-effector position \mathbf{x} w.r.t. the desired equilibrium point \mathbf{x}_{ref} . If we consider such dynamics $\mathbf{Z}(z)$ as the one of a virtual spring-damper, we get:

$$\mathbf{F}_{ref} = \mathbf{K}_x(\mathbf{x}_{ref} - \mathbf{x}) + \mathbf{D}_x(\dot{\mathbf{x}}_{ref} - \dot{\mathbf{x}}) \quad (4.6)$$

where \mathbf{D}_x is a damping, and \mathbf{K}_x a stiffness matrix defined in the end-effector space. To generate the forces \mathbf{F}_{ref} at the end-effector, we need to apply torques at the joints. The reference torques for the actuators can be obtained with the transposed of the leg Jacobian \mathbf{J} .

$$\boldsymbol{\tau}_{ref} = \mathbf{J}^T (\mathbf{K}_x(\mathbf{x}_{ref} - \mathbf{x}) + \mathbf{D}_x(\dot{\mathbf{x}}_{ref} - \dot{\mathbf{x}})) \quad (4.7)$$

Despite this is valid for fixed base robots [Sciavicco and Siciliano, 2000], we will show in Section (4.2.4) that this might not be the most accurate way to map forces in the case of a floating base robots, because mutual interaction between legs are neglected. However, this approach works reasonably well in practice. More complex implementation of impedance control that will consider mutual interactions between legs will be part of future works. In our case, since we are not willing to control foot orientation, \mathbf{J} , \mathbf{D}_x and \mathbf{K}_x will be 3×3 matrices. The block diagram of the controller is shown in Fig. 4.14. Let us consider, because it is useful for the following analysis, that the actuators are ideal torque sources ($\boldsymbol{\tau} = \boldsymbol{\tau}_{ref}$). After substituting (4.7) in 4.5 it will result in the following controlled dynamics for the leg:

$$\mathbf{M}_\theta \ddot{\mathbf{q}} + \mathbf{h}(\mathbf{q}, \dot{\mathbf{q}}) = \mathbf{J}^T (\mathbf{K}_x(\mathbf{x}_{ref} - \mathbf{x}) + \mathbf{D}_x(\dot{\mathbf{x}}_{ref} - \dot{\mathbf{x}})) + \mathbf{J}(\mathbf{q})^T \mathbf{F}_{int} \quad (4.8)$$

However, as can be deduced by (4.8), the desired behavior $\mathbf{F}_{int} = \mathbf{Z}\mathbf{x}$ cannot be achieved, unless the leg dynamics is compensated. This can be (ideally) achieved adding the torques \mathbf{T}_{ffwd} computed by an inverse dynamics algorithm [Mistry et al., 2010]. These torques are computed using the second derivative of the reference trajectory and the robot joint velocities and positions. What in practice, we implement in the HyQ robot is a "partial" feedback linearisation because we do not multiply the controller (4.7) for the leg inertia matrix \mathbf{M}_θ . In particular this inverse dynamics is implemented in the joint space (Fig. 4.14). The total actuator torque after

4.2. Impedance control for the whole leg

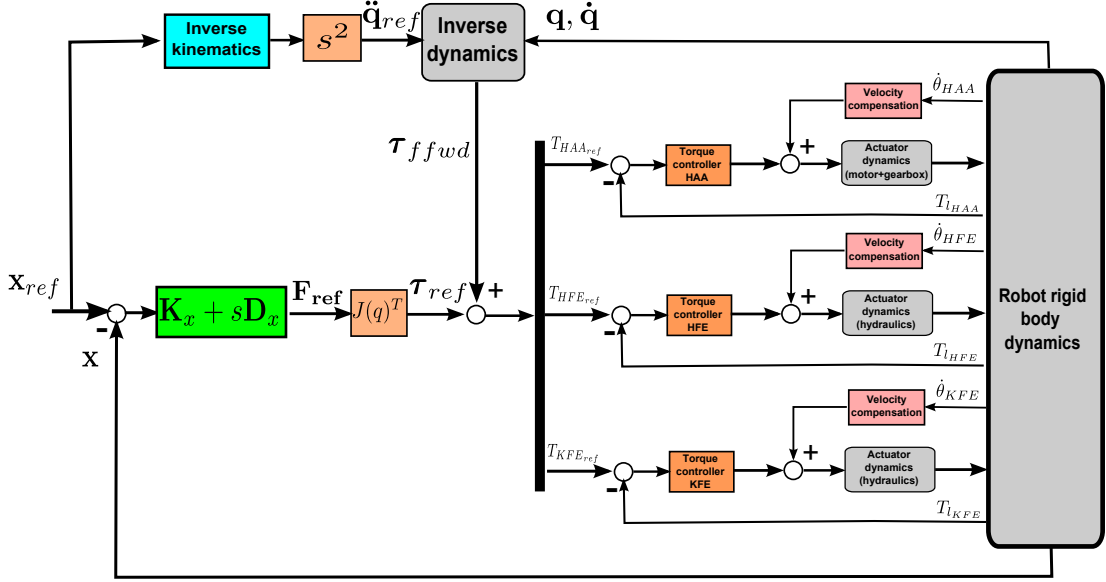


Figure 4.14: Block diagram of the task-space impedance controller implemented for the HyQ leg.

adding the inverse dynamics, becomes:

$$\boldsymbol{\tau} = \mathbf{J}^T (\mathbf{K}_x(\mathbf{x}_{ref} - \mathbf{x}) + \mathbf{D}_x(\dot{\mathbf{x}}_{ref} - \dot{\mathbf{x}})) + \hat{\mathbf{M}}_\theta \ddot{\mathbf{q}}_{ref} + \hat{\mathbf{h}}(\mathbf{q}, \dot{\mathbf{q}}) \quad (4.9)$$

where $\hat{\mathbf{h}}(\mathbf{q}, \dot{\mathbf{q}})$ and $\hat{\mathbf{M}}_\theta$ are an estimation of the coriolis/gravity forces and inertia matrix, obtained by real measurements.

If an inverse dynamic algorithm is not available, it is useful to assess which is the general influence of the the leg dynamics on the end-effector impedance. To do this we will project the dynamics of the leg in the end-effector space by following the operational space formulation approach [Khatib, 1987]. The (4.5) becomes:

$$\underbrace{(\mathbf{J}^{-T} \mathbf{M}_\theta \mathbf{J}^{-1}) \ddot{\mathbf{x}} + \overbrace{\mathbf{J}^{-T} \mathbf{h} - (\mathbf{J}^{-T} \mathbf{M}_\theta \mathbf{J}^{-1}) \dot{\mathbf{J}} \dot{\mathbf{q}} }^\psi}_{\Psi} = \mathbf{F}_{ref} + \mathbf{F}_{int} \quad (4.10)$$

where \mathbf{F}_{ref} are the actuator torques mapped to the end-effector space. Therefore substituting the cartesian impedance law (4.6) in (4.10):

$$\mathbf{F}_{int} = \mathbf{K}_x(\mathbf{x}_{ref} - \mathbf{x}) + \mathbf{D}_x(\dot{\mathbf{x}}_{ref} - \dot{\mathbf{x}}) - \Psi \quad (4.11)$$

4. IMPEDANCE CONTROL

If we transform to the Laplace domain, we get:

$$\mathbf{F}_{int} = [\mathbf{Z}(z) + \delta\mathbf{Z}(z)]x \quad (4.12)$$

This shows that the term ψ which represents the leg dynamics projected in the end-effector space, creates discrepancies between the emulated impedance and the desired one $\mathbf{Z}(z)$. Simulations can be carried out using the locomotion trajectory to assess quantitatively the influence of the different terms on the emulated impedance in relation to the values of the parameters \mathbf{K}_x and \mathbf{D}_x of the desired parameters. When studying the dynamics the controlled leg dynamics (4.8) the actuator dynamics and the influence of the inner torque loop was neglected. However a analysis similar the one of Sections 4.1.3 and 4.1.6 can be carried out for the controller (4.7) if a model of the leg which includes all the actuators is considered. Since the leg is has not linear the analysis should be carried out for different leg configurations. This will part of future works.

4.2.2.3 Experiments

To show the effectiveness of the implemented task-space impedance controller experimental tests have been performed considering the leg only as a fixed base system. A way to demonstrate that forces generated by the robot emulate the desired impedance behavior is showing how the controller is able to track a desired stiffness ellipsoid. For the sake of simplicity, we constrained this experiment only to the x-y plane, therefore the ellipsoid shrinks to be an ellipse. The impedance controller (implemented using (4.9)) will only produce a torque or force once the force acting on the robot has produced changes in the robot motion (velocity and position). In this test, the foot desired position \mathbf{x}_{ref} is kept constant while a user was moving the foot on a circular path (constrained on the x-y plane) creating disturbance torques. These disturbance torques create displacements in the links and then the impedance controller produces a force. The time- history of these forces are recorded together with the displacements and by simple vector algebra computations, it is possible to assess the stiffness ellipse in the x-y plane. Selecting the stiffness parameters (k_{xx} and k_{yy} in the diagonal of the stiffness matrix) is possible to define different shape of the stiffness ellipse, according to Table 4.2.

Table 4.2: Stiffness ellipses

Ellipse Shape	$k_{xx}[N/m]$	$k_{yy}[N/m]$
Shape 1	300	300
Shape 2	150	400
Shape 3	400	150

4.2. Impedance control for the whole leg

In particular, the left plot of Fig. 4.15 shows a configuration in which the values are equal (shape 1) and the stiffness ellipse becomes a circle. In the right and bottom plots, a stiffness ellipses is represented in which the stiffer direction is y (shape 2) and x (shape 3) respectively. The plots in Fig. 4.15 demonstrate the effective versatility of the implemented controller in shaping the stiffness behavior at the end-effector.

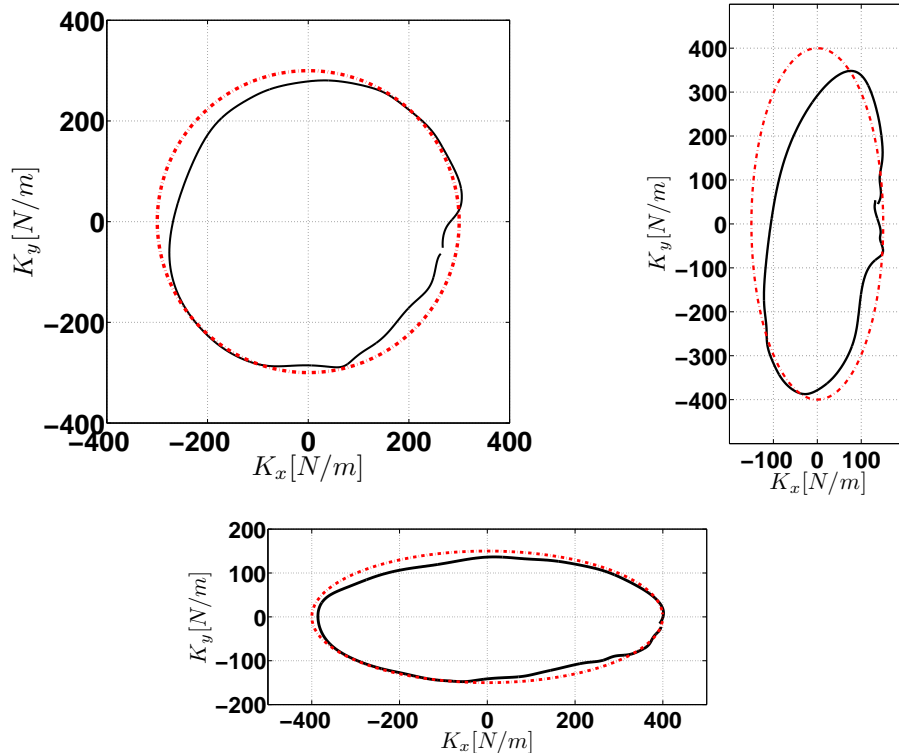


Figure 4.15: Stiffness ellipse emulation in the x-y plane: desired stiffness ellipse (dashed line) and experimentally estimated stiffness ellipse by measured end-effector forces and positions (solid back line). The plots are relative to the set of parameters defined in Table 4.2. Left: shape 1, Right: shape 2, Bottom: shape 3

4.2.3 Specifying performances for impedance control

A fundamental problem in robotic systems is that of specifying the dynamic behavior when the system is constrained and unconstrained, that is when the system interacts with other systems (including the environment) and when it is free to move. The dynamic behavior of the system can be specified by selecting a suitable range of impedance parameters for the mechanical system, i.e. specify the dynamic relations between forces (torques) and positions. Defining a

4. IMPEDANCE CONTROL

set of parameters for the desired impedance as well as the relevant frequency range of operation and the stability of the robot is an important step before any design can be formulated as a meaningful control problem. However this is by no means a trivial a problem and too often is not considered in detail simply because it is deemed to be too difficult or because there is a lack of understanding of the tasks to be achieved. Quite often parameters are selected on a trial and error basis and subsequently this results in poorly designed control systems. The following questions should be addressed:

- How to select a suitable range of impedance parameters for a particular range of tasks.
- How to specify the frequency range of operation, e.g., walking, running, gallop, trot.
- Requirements on stability, e.g. when the system interacts with the environment and when the system is free to move.

The answers to these questions will have profound implications on the design of suitable control systems, actuator and sensor requirements as well as an impact on the design of the mechanical system. The selection of the stiffness, damping and inertia parameters should correspond to various task objectives. For example, high stiffness is specified when the environment is compliant and positioning accuracy is important. On the other hand, low stiffness is specified for contacts with a stiff environment or to maintain small contact forces. Large damping values are specified to reduce oscillations (vibrations) or to dissipate energy. Inertia or mass values can be used to smooth the response of due to external contacts. Using inertia or mass terms as part of the impedance control strategy requires accelerations and this may become quite noisy in systems that only have position sensors. Besides selecting a suitable range for the impedance parameters, there may also be a need to specify how these parameters vary during the robot operation. Switching between impedance parameter values can be a function of the type of environment or contact as well as a function of the joint state. For example, if we consider robot locomotion, during the stance phase the robot must have stiff legs to reduce sag under its own weight. Conversely, when it is swinging could be important to have the leg compliant to negotiate the obstacles. The stiffness may also be a nonlinear function and non linear (e.g exponential) virtual springs can be also implemented at the end-effector.

We will present here a practical rule of thumb to select the impedance (task space) parameters for a typical locomotion task of our quadruped robot. The stiffness matrix \mathbf{K}_x is typically selected to be diagonal. The elements on the diagonal represent the stiffness in the 3 directions X, Y, Z . Their values can be chosen taking into account which is the tracking error that we accept in each direction. For example in the case of HyQ to have a precise foot placement during trotting we selected a Z component around 6000 N/m . We set 2000 N/m in X and Y direction

4.2. Impedance control for the whole leg

to better negotiate frontal and lateral impacts respectively. To select the damping matrix \mathbf{D}_x , we need to consider the dynamics of the leg with the impedance controller and set a critical damping behavior to have no overshoot. If an full inverse dynamics algorithm is implemented, the controlled robot dynamics (4.8) can be (ideally) described by a decoupled set of integrators:

$$\ddot{\mathbf{x}} = \mathbf{K}_x(\mathbf{x}_{ref} - \mathbf{x}) + \mathbf{D}_x(\dot{\mathbf{x}}_{ref} - \dot{\mathbf{x}}) + \mathbf{F}_{int} \quad (4.13)$$

In this case we can set a damping to have critical/overdamped behaviour (no overshoot) as follows:

$$\mathbf{D}_x = 2\sqrt{\mathbf{K}_x \mathbf{I}} \quad (4.14)$$

where \mathbf{I} is the identity matrix. If an inverse dynamics algorithm is not available, the inertia of the leg reflected to the end-effector (task space inertia matrix) $\mathbf{M}_x = \mathbf{J}^{-T} \mathbf{M}_\theta \mathbf{J}^{-1}$ must be considered (see (4.10)). The terms $\mathbf{J}^{-T} \mathbf{h}$ and $\mathbf{M}_x \mathbf{J} \dot{\mathbf{q}}$ are generally low in comparison with the terms due to the impedance control $\mathbf{K}_x \Delta \mathbf{x}$ and $\mathbf{D}_x \Delta \dot{\mathbf{x}}$ and, in a first approximation, can be neglected. If gravity is compensated the leg dynamics can be approximated to:

$$\mathbf{M}_x \ddot{\mathbf{x}} = \mathbf{K}_x(\mathbf{x}_{ref} - \mathbf{x}) + \mathbf{D}_x(\dot{\mathbf{x}}_{ref} - \dot{\mathbf{x}}) + \mathbf{F}_{int} \quad (4.15)$$

Now the matrix \mathbf{M}_x is usually a full matrix. By discarding the off-diagonal terms and considering only the diagonal ones ($\tilde{\mathbf{M}}_x$) we can set a critically-damped dynamics by choosing the following damping matrix:

$$\mathbf{D}_x = 2\sqrt{\mathbf{K}_x \tilde{\mathbf{M}}_x} \quad (4.16)$$

This is obviously a crude approximation because we are discarding completely the off-diagonal terms but might be good as a starting point before performing more refined tuning. It is worth to remark that in practical implementations the damping matrix should be computed at any control loop (or at lower rate) because the task-space inertia matrix is changing with the configuration.

Another approach which is more correct that does not discard the off diagonal terms of \mathbf{M}_x is described next. Let us define a linear system that describes the dynamics of a rigid body mass that we imagine attached at the end-effector whose inertia is \mathbf{M}_x without any stiffness and

4. IMPEDANCE CONTROL

damping:

$$\ddot{\mathbf{x}}\mathbf{M}_x = \mathbf{u} \quad (4.17)$$

where \mathbf{x} is the Cartesian position of the end-effector. The state space representation of this system is:

$$\ddot{\mathbf{x}} = \mathbf{A}\dot{\mathbf{x}} + \mathbf{B}\mathbf{u} \quad (4.18)$$

where $\hat{\mathbf{x}} = [\mathbf{x}^T \quad \dot{\mathbf{x}}^T]^T$ is the state vector containing Cartesian positions and velocities. We define the matrix \mathbf{A} and \mathbf{B} as:

$$\mathbf{A} = \begin{bmatrix} \mathbf{0}_{3 \times 3} & \mathbf{I}_{3 \times 3} \\ \mathbf{0}_{3 \times 3} & \mathbf{0}_{3 \times 3} \end{bmatrix} \quad \mathbf{B} = \begin{bmatrix} \mathbf{0}_{3 \times 3} \\ \mathbf{M}_x^{-1} \end{bmatrix} \quad (4.19)$$

Now it is possible to solve a pole placement problem (e.g. use the *Matlab* command $\mathbf{F}_b = place(\mathbf{A}, \mathbf{B}, p_{des})$) to compute the feedback \mathbf{F}_b that moves the poles of the system at the desired locations p_{des} . These locations are the eigenvalues of the system $\tilde{\mathbf{A}}$ (e.g. use the *Matlab* command *damp*($\tilde{\mathbf{A}}$)) that is described by the diagonal task space inertia matrix $\tilde{\mathbf{M}}_x$ and the desired stiffness \mathbf{K}_x and damping \mathbf{D}_x .

$$\tilde{\mathbf{A}} = \begin{bmatrix} \mathbf{0}_{3 \times 3} & \mathbf{I}_{3 \times 3} \\ -\tilde{\mathbf{M}}_x^{-1} \mathbf{K}_x & -\tilde{\mathbf{M}}_x^{-1} \mathbf{D}_x \end{bmatrix} \quad (4.20)$$

The first 3 columns of F_b is the new stiffness matrix the last 3 the new damping matrix. This approach has the advantage of including the off diagonal terms, giving you a nice combination of stiffness and damping that suits the \mathbf{M}_x matrix (in a certain leg configuration) on the same time achieving the desired dynamics (p_{des}) for the impedance. The problem with this method is that solutions are not unique, and there is no guarantee about robustness properties. Furthermore, it is worth to point out that the damping matrix D_x resulting from the derivation above is suitable to obtain a critically damped behaviour for the inertia of the leg but it might result in a under-damped system if also the body mass is considered. Indeed legged systems are facing two fundamentally different periods in locomotion that are defined as stance and swing phase. This separation is reflected in a very different plant model: during stance phase, the system has a high inertia mass since the main body is heavy comparably to the leg and the ground does not move at all, conversely during the swing phase the inertia seen by the actuators of leg is only

4.2. Impedance control for the whole leg

the one of the leg links. Now the specifications for the damping matrix \mathbf{D}_x that we obtained by the pole placement were relative to a desired dynamic which considered only the leg inertia. Therefore, since during the stance the inertia is much larger, this might result in a system that is not damped enough during the stance.

This means that the desired interaction behaviour can be achieved if the leg is hitting an obstacle during the swing but oscillations can occur when the leg is in touch-down and it is loaded with part of the body mass that increase its inertia. The solution is either to increase the damping value or to find a more systematic approach. Further research is needed and this is left as an open question.

4.2.4 Ground reaction forces

In this section we will discuss the estimation of the interaction forces that mostly are relevant in a legged robot: the ground reaction forces. In particular we will discuss advantages and drawbacks of different methods to estimate them. Depending on the purpose, different approaches must be adopted for the estimation. For instance, if the goal is to implement an inverse dynamics algorithm for a floating base robot, it is important to have a noise-free estimate of the forces. Therefore an estimation based on the kinematic state of the robot is preferable. Legged robots differ from fixed-base manipulators in that they are supported by the ground and need to maintain balance stability. To characterize contact constraints we represent these as free floating systems with six passive DOFs attached to their base [Sentis, 2007]. The action of the gravity causes reaction forces to appear on the robots feet or on the supporting structures. Once in contact, the robots motion is similar to that of parallel structures [Stewart, 1965]. A widespread method to compute ground forces is using the Lagrange multiplier approach, where a set of constraints $h_c = 0$ (feet that are on the ground) is added to the full floating base dynamics [Mistry et al., 2010]. Considering the full floating base rigid body dynamics:

$$\mathbf{M}(\mathbf{q})\ddot{\mathbf{q}} + \mathbf{C}(\mathbf{q}, \dot{\mathbf{q}}) + \mathbf{g}(\mathbf{q}) = \mathbf{S}^T \boldsymbol{\Gamma} + \mathbf{J}_C^T(\mathbf{q}) \boldsymbol{\lambda} \quad (4.21)$$

$\mathbf{q} = [\mathbf{q}_r^T \mathbf{x}_b^T]^T$ are the generalized robot coordinates including joint angles \mathbf{q}_r and the six base DOFs \mathbf{x}_b . $\mathbf{M}(\mathbf{q})$ is the floating base inertia matrix, $\mathbf{C}(\mathbf{q}, \dot{\mathbf{q}})$ is the floating base Coriolis/centripetal vector, $\mathbf{g}(\mathbf{q})$ is the floating base gravity vector, and $\boldsymbol{\Gamma}$ is the joint torque vector and $\mathbf{S} = [\mathbf{I}_{n \times n}, \mathbf{0}_{6 \times 6}]$ is a selection matrix extract joint space variables from the full floating base variables. $\mathbf{J}_C(\mathbf{q})$ is the constraint Jacobian and represent a stack of the jacobian of the feet that are in stance (since our robot has point feet the constraint will be only on the position not on the orientation). Following the derivation presented in [Mistry et al., 2010] is possible to obtain

4. IMPEDANCE CONTROL

the expression:

$$\boldsymbol{\lambda} = (\mathbf{J}_C \mathbf{M}^{-1} \mathbf{J}_C^T)^{-1} [-\dot{\mathbf{J}}_C \dot{\mathbf{q}} + \mathbf{J}_C \mathbf{M}^{-1} (\mathbf{C} + \mathbf{g} - \mathbf{S}^T \boldsymbol{\Gamma})] \quad (4.22)$$

where $\boldsymbol{\lambda}$ is the estimate of the contact forces. Eq. (4.22) has the drawback to be prone to modelling errors and requires the assumption of rigid contact at the feet. Furthermore it prediction might not be accurate enough to be used in a feedback controller. However since it is obtained by kinematic measurements this estimate has a noise lower than a force sensor. This characteristic is a crucial feature for an inverse dynamics algorithm where noise would be directly reflected into the desired torques sent to the robot. Conversely, if the purpose is to close a loop, a direct measurement is might be better than an modelling error-prone estimate. A way to determine contact forces \mathbf{F}_{int} in the case of a non-redundant fixed-base manipulator (e.g. a single leg) is by the joint torque sensor readings $\boldsymbol{\tau}$:

$$\mathbf{F}_{int} = -(\mathbf{J}^T)^{-1} \boldsymbol{\tau} \quad (4.23)$$

This approach is valid only in static conditions [Sciavicco and Siciliano, 2001]. Indeed the torque sensors measure also the inertial/gravity/coriolis forces due to the leg motion and friction together with contact forces. In addition to this, it is when considering a floating base robot, estimating ground forces on each leg separately, by using (4.23), it is incorrect because there is a coupling between the robot joint motion and the resultant motion of the base. We present in Table 4.3 a comparison of the ground reaction forces (in the *LF* leg) estimated by (4.23) with the real ones computed with a penalty ground contact model. We performed a simulation in the SL environment with the robot standing still on the ground. Table 4.3 shows that the estimation presents a certain error even in static conditions.

Table 4.3: Evaluation of the joint torque approach (4.23) to estimate ground reaction forces

Force direction	Penalty contact model	Joint torque approach
F_x [N]	-33	-26
F_y [N]	-31	-32
F_z [N]	187	176

Moreover, from the dynamic point of view, since torque sensors are not located at the point of contact, it is always present a certain compliance, in the mechanical structure between them and the point of contact, that filters the dynamics of the impact (see Fig.B.8 for experimental tests that show this effect). Differently a foot sensor located at the end-effector would resolve the non-collocation issues by giving a direct measurement of the contact forces. This measure

4.2. Impedance control for the whole leg

can be used as feedback for a controller or (in future works) "fused" with the prediction (4.22) coming from the above-mentioned approach.

A short-coming that prevents the wide-spread use of force sensors in legged robots is the high price together with the weight. Generally the weight is directly related to the measurable range of forces. Indeed commercial sensors that are enough range to measure the impacts that occur during HyQ locomotion (2000N), are heavy and bulky (e.g. model Delta160 from ATI). An heavy foot sensor is prejudicial for the leg dynamics because is a mass placed in the most distal part of the leg and thus has the highest influence on leg inertia. On the other hand, lighter sensors have a smaller measuring range (ATI model mini45). This motivated us to design a custom 6 axis foot force sensor for our robot, that fulfills the requirements on force range and at the same time is rugged, lightweight and easily embeddable in the HyQ leg. Last but not least, the low price was also an important constraint in a platform designed to perform very dynamic tasks. Indeed, during experiments, robot failures can lead to damage of the sensor and might need otherwise expensive replacements. The design of the 6 axis foot sensor is described in Appendix B.1

4.2.5 Summary

In the last sections the implementation of the impedance controller for the whole leg has been presented. Two implementation are detailed: one in the joint space a one in the end- effector space. The disadvantage of the joint space implementation is that a configuration dependent impedance is created at the end-effector. The possibility to have an impedance defined in the body frame that is not dependent on joint position and the necessity to specify impedance at the interaction point (end-effectors) where locomotion requirements and foot trajectories are normally defined, motivated the task-space implementation. A discussion on how to select the impedance gains according to locomotion requirements is also presented. A simple rule of thumb is also given to quantitatively select them. Finally an overview on different methods to estimate interaction force (ground reaction forces) in legged robotics is presented with a discussion on the relative pros and cons.

4. IMPEDANCE CONTROL

5

Passive compliance in robot legs

In this chapter, a foot element is designed to be added to the HyQ leg with the goal of reducing the transmission of the impact forces to the structure and protect the delicate components like loadcells, gearboxes, etc. Indeed, large forces are generated due to the interaction of the robot with the terrain, especially during very dynamic motions (e.g. jumps, flying trot). These impacts should be handled by the impedance controller whose purpose is to create a desired impedance behaviour in response to them. As shown in Section 4.1.6, there is a range of frequencies in which the impedance is tracked and this depends also on the actuator bandwidth. In general this range becomes smaller, if the robot is equipped with low-bandwidth actuators, because the impedance controller response lags in the very first milliseconds of the impact, and therefore is not able to emulate the desired impedance. An impact is a impulsive force input with high frequency harmonics that the controller is not able to handle completely. In particular the robot can be considered without control in the first milliseconds of the impact and the generated forces are due to the interaction of the ground with the passive compliance of the leg. If the controller is not considered, this is mainly due to passive compliance of the actuators. Hydraulic actuators have inherent passive compliance due to the oil compressibility. However, the high bulk modulus results in a joint compliance that was estimated to be around $K = 2 - 3 \cdot 10^4 \text{ Nm/rad}$ for a 16 mm bore double acting cylinder attached to a 45 mm lever arm [Boaventura, 2013]. This passive hydraulic compliance may not be sufficient to protect the weakest components (e.g. gearboxes at the adduction joints, loadcells and bearings) in present of short duration but very high peak forces that are transmitted to the structure at the moment of touch-down. This can lead to damages and over time to fatigue fractures if a long-time operation is required. The introduction of passive compliant elements in the robotic leg (if appropriately designed) can significantly reduce the transmission of these peak forces thus improving robustness and reliability of the robot. In this chapter a methodology on how to

5. PASSIVE COMPLIANCE IN ROBOT LEGS

select the passive stiffness to achieve a certain reduction in the transmission of the impact force is presented. In particular a passive foot has been designed (Fig. 5.1) for the HyQ robot that introduces a prismatic ankle joint which includes the selected passive linear spring (see appendix B.2 for a detailed description of the mechanical design). To show the effectiveness of



Figure 5.1: Picture of the built prototype of the passive foot.

the proposed approach the robot is equipped with lower-bandwidth actuators for which higher peak forces are resulting during locomotion due to the higher actuation delay. Namely, for the experiments carried out in this chapter, the robot leg is equipped with Wandfluh (NG3-Mini) [Wandfluh, 2007] proportional valves for the control of the flow in the hydraulic joints. Wandfluh valves have a slower response (32 Hz bandwidth [Cunha et al., 2010]) in comparison with the Moog valves [MOOG Inc., 2003] (250 Hz bandwidth) that are the default outfit for the HyQ robot. Experimental results are presented that show the effectiveness of the built foot prototype to reduce these peak forces. The advantages and drawbacks of using compliant elements in locomotion are also discussed.

Traditionally springs are introduced in robotics for energy-efficiency purposes: they allow more efficient locomotion by exploiting the natural dynamics of the robot mechanics. However in the HyQ robot, we are not interested in the energy saving capability of springs because of the following reasons:

- due to the valve inefficiency (almost 1 kW of power is lost due the valve leakage flow) the work saved by the springs would be very low in comparison with the one dissipated by the valves.
- According to the topology of the leg depicted in Fig. 2.7, the force generated by the spring during the energy release (e.g. liftoff) phase while running, would not be pointing

5.1. Selection of the passive compliance

through the *HFE* joint axis. Having this force pointing through the hip joint is very important to have this force transmitted to the torso without having the actuators to do any work. Indeed experimental evidence from biology has shown that this is what happens for animals [Alexander, 1988]. If the force on the foot is always in line with the hip joint no torque will be needed in hip muscles. In the case of the HyQ robot, an additional ankle joint would be necessary to orientate the lowest limb in order to have a contact force always pointing through the hip axis. In the actual setup this means increasing the leg complexity (we would have an articulated leg which has redundant DOFs) and adding more inertia. However as a design guideline for HyQ we choose to keep the complexity low by having the minimum numbers of DOFs (three) to explore the 3D workspace.

5.1 Selection of the passive compliance

To select the value of the passive spring to be fitted in the passive foot, we first need to investigate how the ground reaction force is transmitted through the HyQ leg after an impact. Subsequently, we will investigate how the value of the passive spring affects this transmission. A possible template to study this, is the simple spring-mass model suggested by Alexander in [Alexander, 1990] which is useful to describe the vertical dynamics of a controlled legged robot of body mass M_b which has a compliant element K_p at the foot (see Fig. 5.2)(left).

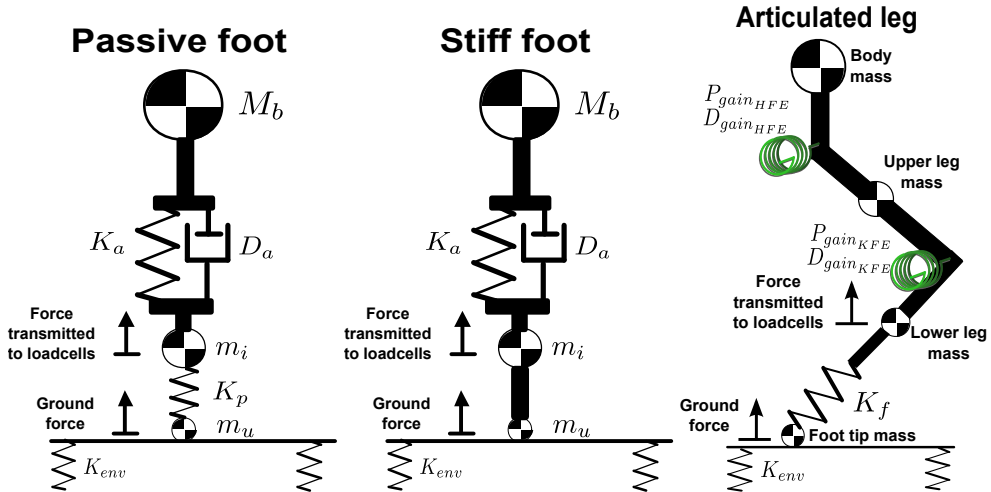


Figure 5.2: Spring-mass model of a legged robot with a compliant foot (left) and a stiff foot (middle). Schematic of the articulated leg (right) showing the joint stiffness P_{gain} and damping D_{gain} due to the joint impedance controller and the foot passive stiffness K_f .

m_i is the intermediate mass between the leg impedance (K_a, D_a) and K_p the passive com-

5. PASSIVE COMPLIANCE IN ROBOT LEGS

pliance due to the foot while m_u is the small unsprung mass represented by the foot tip and K_{env} is the ground surface stiffness.

In our case the leg impedance (K_a, D_a in the vertical direction) is due to the impedance controller and to the passive compliance of the hydraulic actuators. Figure 5.2(middle) shows a similar model for a leg with a stiff foot. The stiff foot is the original HyQ foot that consists just of a rigid connection between the foot tip and the lower-leg link. Even though the models depicted in Fig. 5.2 (left and right) may give qualitatively interesting insights on the shape of the ground forces, to select the passive foot spring a more accurate model of the leg is necessary which includes the actuator dynamics and is able to represent the articulated nature of the leg (Fig. 5.2(right)). In fact, in the case of the HyQ leg (left front) (see Fig. 2.7(right)) it is not trivial to sort out from the articulated leg model, which is the value of the mass m_i to put in the spring-mass model. In particular, since the foot spring stiffness K_f which is aligned with the lower-leg, it is not easy to understand how that stiffness would map into the vertical direction to obtain the value of K_p . For this reason in our study we consider a model of the HyQ leg (Fig. 5.2(right)), built in the SL environment, where the dynamics of the actuators is also considered (see Fig. 5.3). The model in Fig. 5.2(left) will still be useful to interpret the results of these simulations.

The target is to select the passive spring to reduce impact forces that arise after dropping the leg from a certain height when the impedance controller action is delayed due to the limited bandwidth. This is a good template also to represent non-nominal situations (power failure, controller failure, sensor failure, etc) in which the robot be exposed to undergo high impact forces.

Therefore, simulations are carried out dropping the leg from a 10 cm height to a very stiff surface (worst situation) and ground reaction forces are logged at the moment of the impact. To reduce the degrees of freedom of the design problem we need to add some specifications.

The ground reaction force depends on several aspects: configuration of the leg at the moment of touchdown, impedance gains and bandwidth, ground stiffness and foot stiffness. Therefore we will restrict the analysis considering a *default* leg configuration ($HAA=0$, $HFE=0.7$, $KFE=-1.4$ rad see Fig. 5.2 (right)) about which the periodic foot trajectories are generated for HyQ locomotion. We will consider a joint space implementation of the impedance controller with the impedance parameters ($P_{gain} = 300N/m$ and $D_{gain} = 6Nms/rad$) that we most frequently use in our experiments.

The results of the 10 cm drop tests are presented in Fig. 5.4. The plots show the torque generated by the impact in the knee joint in the case that the stiff foot is considered and in the case the passive foot is considered with different spring stiffness K_f . The mass of the leg is set at 11 kg to be consistent with the experimental setup. To interpret the results, we can make use

5.1. Selection of the passive compliance

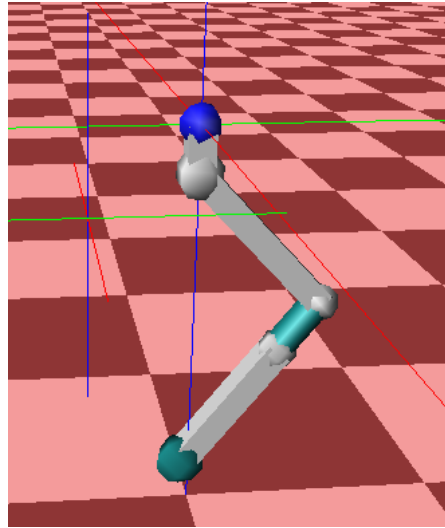


Figure 5.3: SL model of the HyQ leg used for simulating drop tests. The dynamics of the actuators are considered in the model.

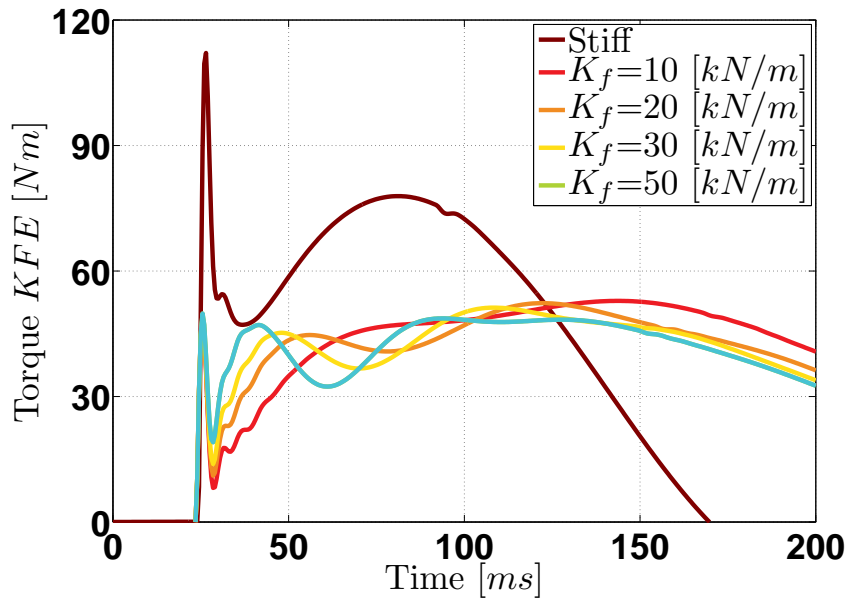


Figure 5.4: Simulation of the drop tests of the HyQ leg from 10cm height. The curves represent the joint torque measured by the loadcell at the knee. The different curves represent the simulated forces for different foot spring stiffness (ranging from 10000 to 50000N/m) and for the case of the stiff foot.

of the models depicted in Fig. 5.2. The first peak (from the left) is due to the small unsprung

5. PASSIVE COMPLIANCE IN ROBOT LEGS

mass m_u of the foot end-tip. This peak will be directly transmitted to the knee joint in the case of the stiff foot and thus is very high. If a compliant foot is used the end-tip is decoupled from the lower leg link and the very first short peak will be significantly filtered. This is already an important result. However, including the foot spring, a second peak can arise due to the deceleration of the intermediate inertia m_i . This second peak cannot be controlled and will be present in the knee torque signal because the torque sensor (loadcell) is directly connected to the intermediate inertia m_i that represents the lower leg inertia). The third peak depends only on the selected impedance and can be controlled. The foot spring stiffness affects the second peak by decoupling more or less the influence of the intermediate inertia m_i to a smaller or bigger extent. Figure 5.4 shows that selecting a passive spring of $K_f = 10000$ or $K_f = 20000$ can reduce the first peak by more than than 60% and also significantly smooth the second one. An additional constraint, when selecting the value of the spring, is that the maximum compression achieved during locomotion must be lower than the maximum compression allowed for of the spring. Indeed, if the spring compresses completely the decoupling effect introduced by the spring is no longer present and the force will be transmitted directly to the structure like in the case of the stiff foot (a rubber padding at the end-stop could slightly damp this effect). Table 5.1 gives the maximum compression values of the foot spring for the simulated drop tests of Fig. 5.4:

Table 5.1: Foot maximum compression for 10 cm drop tests with different foot springs K_f

Stiffness K_f [kN/m]	10	20	30	50
Maximum compression [mm]	26	15	11	8

5.1.1 Discussion

Another constraint to the maximum compression can be given by the locomotion task. Indeed the compression of the spring represents an uncontrollable error in the foot position accuracy. Depending on the nature of the locomotion task different trade-offs must be accepted. If the task is a highly dynamic trot it is more important to reduce the peak forces than keeping the positioning error low, thus a more compliant spring will be preferred. Conversely, if a more precise positioning task is performed, in general lower impact forces are involved but more strict requirements will exist on foot positioning accuracy. In this case a stiffer spring is preferred. This reasoning seems quite intuitive from a qualitative point of view; however, the proposed methodology allows to quantitatively select a limited range of passive springs that satisfies the requirements given by the locomotion task at hand. This highlights the main limitation of using passive element which may restrict the versatility of the robot, because a certain value for the

passive spring that is suitable for one task might not be good for another one and a trade-off is always required between foot position errors and impact reduction. In order to avoid this trade-off, variable stiffness actuators (VSAs) have been recently proposed [Ham et al., 2009; Tsagarakis et al., 2011]. VSA are compliant actuators which can vary their passive stiffness with a second actuator, allowing to set the stiffness to the value which is most suitable for the task at hand. However, even though VSA is a promising solution for compliant robots, aspects such as weight, volume, and velocity saturation still limit its use in highly-dynamic robots. The other alternative (which we pursued in the HyQ robot) is to increase as much as possible the range of frequencies in which the desired impedance is tracked in order to have the controller react as fast as possible, thus actively controlling the impact forces. For this reason high bandwidth actuators (e.g. hydraulics cylinder equipped with fast MOOG servo valves) are of great importance as demonstrated in [Boaventura, 2013].

5.2 Experiments

5.2.1 Drop tests

To demonstrate the effectiveness of the compliant foot prototype in reducing the first peak of the impact forces, several drop tests have been carried out for comparison with the stiff foot on a real setup (see Fig. 5.5). The joint configuration was the same as in simulation. The dropping tests have been performed on a single robotic leg mounted on a vertical slider. An absolute encoder (Austrian MicroSystems AS5045), connected to a steel cable and pulley system, was used to measure the vertical position of the leg on the slider. In this analysis only the 2 links on the HyQ leg in the sagittal plane (*HFE* and *KFE*) are considered (see Fig. 2.7 for nomenclature). The total weight of the leg is 11 kg which includes also the slider carriage. For the tests with the compliant foot a passive spring ($K_f = 16\text{kN/m}$) has been selected which, according to the simulations, should reduce the initial peak by at least 50%. The compliant foot is attached to the HyQ leg as shown in Fig. 2.7 (right). The leg is dropped from 10cm height and load-cells, in series with the cylinder rods, measure the torque at the joints. To assess the transmission of the impact forces we plot in Fig. 5.6 the torque signal measured by the loadcell at the knee. If we consider the path of transmission of the force from the ground to the body, the loadcell sensors are located right after the foot spring and therefore can give a reliable estimate of the force which is transmitted to the leg structure and then to the body. This measurement can also tell us if the peak force is within the mechanical overload limits of the loadcell sensor. Figure 5.6 shows that using the compliant foot almost 50% reduction of the first peak is obtained. This is coherent with the theoretical prediction made in Section

5. PASSIVE COMPLIANCE IN ROBOT LEGS

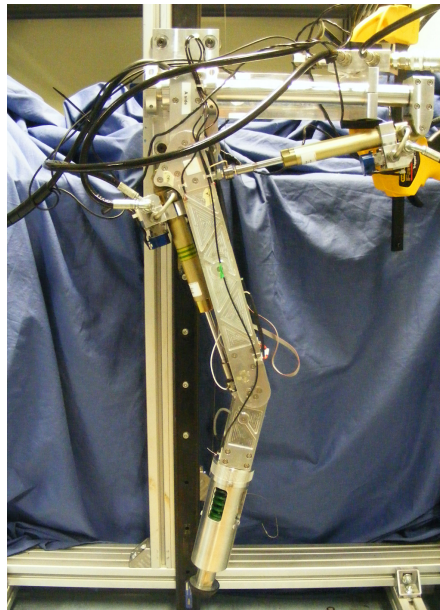


Figure 5.5: HyQ leg with the passive compliant foot mounted on a setup for dropping tests.

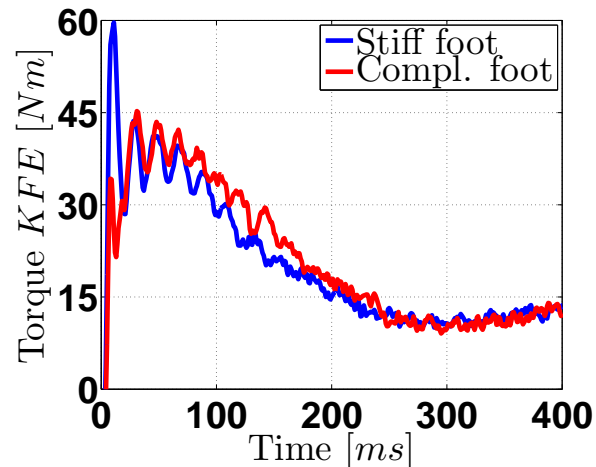


Figure 5.6: Experimental results: drop tests of the HyQ leg with the compliant and stiff foot from a height of 10cm. The impact force transmitted to the leg structure is estimated from the knee torque measured by the loadcell.

5.1. This demonstrates the effectiveness of the compliant foot in reducing the transmission of impact forces to the body resulting in a smoother loading of the robot structure and lower stress. The experimental torque is also quantitatively coherent with the simulation results of

5.3. Flying trot without torque control at the joints

Fig. 5.4 demonstrating the reliability of the model built in SL. The first impact comes from the lagging of the controller that is not fast enough to emulate and render promptly the desired leg stiffness.

5.3 Flying trot without torque control at the joints

In this section we will show that a compliant foot can be of great help whenever torque sensors at the joints are not available and a torque controller cannot be implemented. In this case pure position control algorithms are traditionally used for locomotion. In fact most legged robots

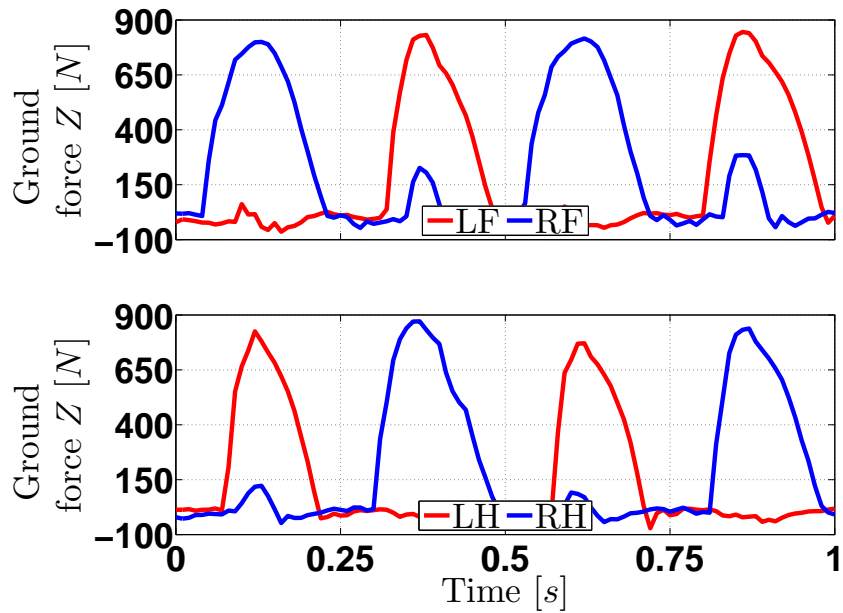


Figure 5.7: Vertical ground reaction forces at the robots feet during 2 cycles of a running trot with flying phase. Left-front (*FL*), Right-front (*RF*), Left-hind (*LH*) and Right hind (*RH*) leg.

usually employ high gain position control motivated by the necessity of having high tracking accuracy (e.g for accurate foot placement). Such controllers can achieve the desired locomotion at relatively low speed. However, for very dynamic motions (e.g. trotting) such controllers are not very robust because the high impacts with the ground caused by the interaction with a stiff controller would create destabilizing forces on the robot body, imposing a serious risk to the overall stability.

Using stiff position control schemes can result in high impact forces also when high-bandwidth valves are used. Indeed, the aim of a stiff position controller is to reject interaction forces not to accommodate them. A trivial way to reduce these forces would be to reduce the

5. PASSIVE COMPLIANCE IN ROBOT LEGS

position gains but this comes at the cost of inferior tracking accuracy [Buchli et al., 2009a]. Since there is not an inner torque loop, inverse dynamics algorithm cannot be used to improve the tracking while having low gains. In these cases equipping the robot with springs at the end effectors can be an alternative solution to reduce the strong impacts while still keeping enough tracking accuracy (thanks to the high position gains) during the leg swing phase (e.g. for accurate foot placement).

In the experimental results of Fig. 5.7 we show that the HyQ robot is able to effectively perform very dynamic tasks (a flying trot) also when a stiff position controller is implemented (instead of impedance control) and low-bandwidth proportional valves (Wandfluh NG3-Mini) are used. Figure 5.7 shows the vertical ground reaction forces of the four feet during 2 cycles of a periodic running trot [Semini et al., 2011a]. The plot shows four distinct force peaks indicating the periods in which the two diagonal leg pairs (left-front *LF*/right-hind *RH*) and (right-front *RF*/left-hind *LH*) are in contact with the ground. An important characteristic number to analyse and describe legged locomotion is the Duty-Factor (D_F), which is defined as the fraction of the stride period that a limb is in contact with the ground [Biewener, 1983]. Values below 50% lead to running. In our experiment the 180 ms stance phase leads to a D_F of 36%. The presence of this flight phase shows that the robot is running.

5.4 Summary

In case the robot is equipped with low-bandwidth actuators, also the bandwidth of the impedance control is reduced. In these cases the actuator is not able to track the impedance sufficiently fast to reduce the impacts forces due the interaction with the ground. In particular, high peaks can result in the first milliseconds after the impact because the controller action is delayed, and the only compliance in the leg is represented by the passive compliance in the hydraulic actuators. In this situation the introduction of a compliant element can be beneficial to reduce these peak forces that would otherwise be transmitted to the body before the controller reacts. This helps to protect the weakest mechanical components of the leg (gearbox, loadcells), and prevent the damage and over time fatigue failure. The selection of this passive compliance is not an easy task and requires the aid of an accurate model of the robotic leg (including actuator dynamics). The value of the passive spring can be determined by an iteration of simulations while checking for which value the desired force peak reduction is achieved. Alternatively, making use of a proper optimization method (future works), it is possible to find which is the optimal results considering different leg configurations. It is important also to check if with the selected stiffness the resulting maximum compression is within the physical limits of the real spring and if it fulfills the requirements given by the locomotion task at hand (in terms of

5.4. Summary

maximum position error).

5. PASSIVE COMPLIANCE IN ROBOT LEGS

6

Semi-active damping with magneto-rheological fluids

In the previous chapter a passively compliant foot element was designed to be added to the HyQ leg with the goal of reducing the transmission of the impact force to the structure and protect delicate component like loadcells, gearboxes, etc. An aspect that has been overlooked in the previous chapter is that such compliant element introduce additional dynamics and may introduce unwanted oscillations. Depending on the relationships between the robot mass, the desired impedance set in the robot controller, and the actual value of the selected foot spring, an impact may result in bouncing/chattering [Alexander, 1990]. Chattering is a phenomenon according to which the foot might leave the ground and return repeatedly. This is undesirable because it leads to a momentary loss of traction with the ground. This is particularly critical when the robot is negotiating slippery or inclined terrain. The solution suggested in this chapter is to let the spring freely compress during the impact and gradually dissipate the energy stored in the spring during the extension phase via a controlled damping force. This energy can in principle be dissipated using a passive damping element. However a passive damper would perform well only for certain robot mass and vertical travel combinations while our goal is to enhance robot versatility in any condition. Furthermore the force generated by a passive damping element will always be present and will be acting against the compression motion at the moment of touchdown, thus creating a higher impact force. This would generate additional forces that would reduce the beneficial effect in terms of peak reduction given by the spring. For this reason we will investigate the feasibility of using controlled semi-active damping [Jalili, 2002] to reduce bouncing. This allows the activation the damping force only in the extension phase, after the spring has achieved its maximum compression. Since the velocity changes sign the damping force will have opposite direction respect to the spring force thus reducing

6. SEMI-ACTIVE DAMPING WITH MAGNETO-RHEOLOGICAL FLUIDS

it but never adding to it. A promising class of semi-active dampers are magneto-rheological (MR) ones [Fischer and Isermann, 2004], which are widely used in automotive semi-active suspensions. They are called semi-active suspension because the active element adds no energy to the system. The main goals of a vehicles semi-active suspension are to maximize traction and reduce vertical acceleration transmitted to the chassis. Therefore, in collaboration with Esa Kostamo (Aalto university) we designed a new custom foot prototype (*MR foot*) that consists of a linear spring and a magneto-rheological damper. By utilizing MR technology in the damper element, the damping coefficient of the compliant foot can be altered in a wide range without any additional moving parts. The damping force can be controlled in a range that goes an be controlled in a range from 15 N to 310 N with a bandwidth up to 100 Hz . The design of the MR foot is described in Appendix B.3. This chapter presents a control algorithm and drop experiments that demonstrate the effectiveness of this device.

6.1 Magneto-rheological fluids and damper

Magneto-rheological fluids are a group of smart materials for which is possible to change the apparent viscosity by applying a magnetic field, resulting in a continuous change of the behavior from a Newtonian "fluid" state to a Bingham-like "toothpaste" state [Bossis et al., 2002]. A typical MR fluid consists of micron-size magnetisable particles in a low viscosity carrier fluid (e.g oil). The yield stress of the fluid can be controlled very accurately by varying the magnetic field intensity, hence the apparent viscosity and so the fluid's ability to transmit force can be controlled with an electromagnet that creates a desired magnetic field. Because the change in the fluids viscosity is completely reversible, this allows us to control the damping coefficient. The advantages of the use of active fluids for damping are that there are not parts which can wear, fast response time, compact dimensions, and a high force level that can be achieved with a low power consumption.

6.2 Robotic leg with MR foot

The robotic leg setup chosen to test the effectiveness of the MR damper is the same one used in Section 5.2. The slider arrangement allows only vertical movements of the leg base. The experimental setup is presented in Fig.6.1(left). Figure 6.1 (right) shows a close-up view of the manufactured prototype of the MR foot. The MR damper was mounted into the lower part of the HyQ leg for this study, thus we have two rotational degrees of freedom (*HFE* and *KFE*) and one prismatic joint degree of freedom (foot compression/extension *FCE*). The joint nomenclature and frame definitions are the same used for the passive foot (refer to Fig. 2.7(right)).

6.2. Robotic leg with MR foot

To simplify the analysis of the damping performance of the MR foot, we substitute the two hy-

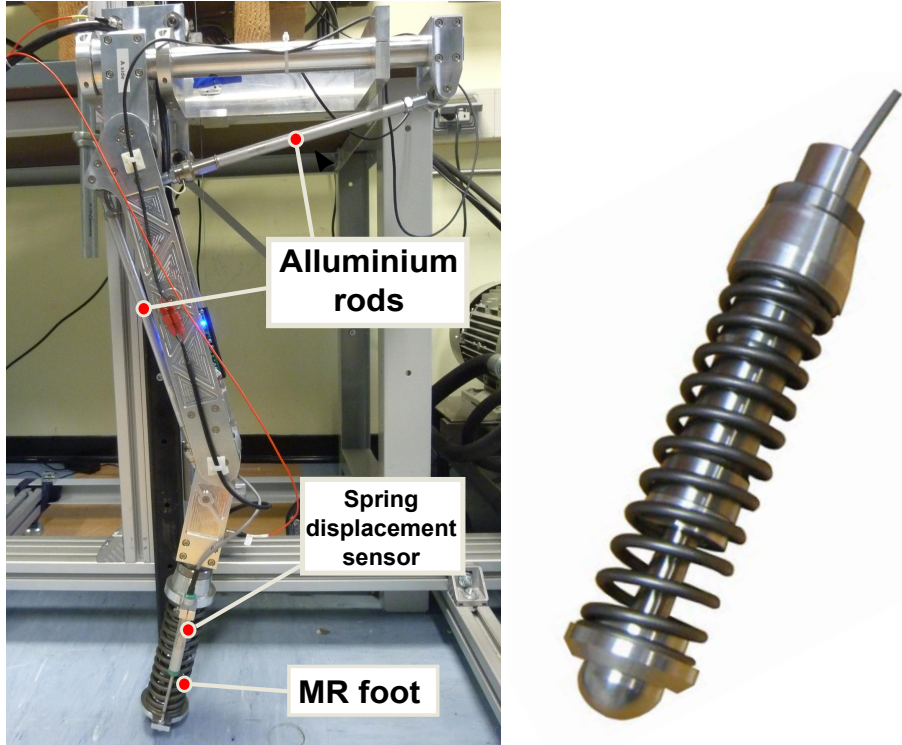


Figure 6.1: Picture of the HyQ robotic leg with the MR foot attached to a vertically sliding test setup (left). A close-up view of the built prototype of the MR foot (right).

draulic pistons with stiff aluminum rods (see Fig. 6.1(left)). Thus the joint configuration space is reduced to 1 DOF (*FCE*). This enables to neglect the influence of the compliance of the oil and the hydraulic hoses, and the only passive compliance in the system is the one represented by the passive spring of the MR foot. This simplification does not prevent the extension to a more general case in which hydraulic compliance is considered. The aluminum support rods were cut to certain length to obtain a configuration for which the foot-tip locates exactly under the hip axis (*HFE* = 0.2 and *KFE* = -0.4 rad). This leg configuration is more stretched than the one used in Section 5.2 to better demonstrate the action of the controller. The spring displacement in the compliant foot was measured by a linear potentiometer (Burster 8709). Due to the presence of an end-stop the spring can only compress. The total leg mass (including the MR foot and the slider carriage) has a total weight of 7 kg. The difference in weight with the setup used in Section 5.2 is due to the absence of the actuation units. The spring in the compliant foot was chosen ($K_f = 16\text{kN/m}$) to have a stiffness that is consistent with the one chosen for the passive foot in Section 5.1.

6. SEMI-ACTIVE DAMPING WITH MAGNETO-RHEOLOGICAL FLUIDS

6.3 Control algorithm

The main goal of the control law, proposed in this chapter, is to eliminate the bouncing of the leg after the first ground contact. This consists essentially in dissipating the excess energy (stored in the spring) that, if released naturally, would create re-bouncing. To implement a control law that eliminates bouncing, first we must note that bouncing is related to the spring elongation velocity. The elongation velocity is strictly related to the body vertical (upward) velocity. If when the spring hits its end-stop, the elongation velocity is not zero, the body will keep moving upwards trailing behind the spring that cannot extend further, thus leading to a loss of traction. Therefore by controlling the elongation velocity to be zero in the moment the spring reaches its resting length, we can reduce the chance of bouncing/chattering. A consequence of this is that all the energy stored in the spring must be gradually dissipated during the extension until the spring reaches the end-stop (free length condition). It is worth to underline that the useful time (e.g. extension phase) interval to apply the control is very short (between 100-200 ms). Therefore, in order to allow the feedback action to have a significant influence on the dynamics, some useful design guidelines are the following: the duration of the controlled interval must be as long as possible, the control law complexity must be low and the feedback signals (e.g. spring displacement) must have a high signal to noise ratio (the noise for the Burster 0709 was measured to be around 0.2 mm).

6.3.1 Critical damping law

During the spring compression phase the control is not active and the compliance of the system is mainly determined by the passive spring and the ground compliance. It must be underlined that, during compression phase, any force created by the damper would increase the force transmitted to the robot body. Therefore, in order to minimize the accelerations transmitted to the robot body, the controllable damping force is applied only during the elongation phase of the spring. A consequence of this is that a damping force is applied which is always opposite to the passive spring force. As explained in the previous section controlling the elongation velocity to be zero in the moment the spring reaches its resting length is an intuitive way to reduce the chance of bouncing. If the spring compression is considered as the state variable of a simple spring-mass system, this can be achieved, by setting a critically damped dynamics. To obtain this we propose a control law where the damping force is controlled as a combination of a virtual negative spring and a virtual damping element. The damping force F_D , can be formulated as:

$$F_D = K_{MR}x_{FCE} - D_{MR}\dot{x}_{FCE} \quad (6.1)$$

6.3. Control algorithm

where x_{FCE} is the spring compression (see definition in Fig. 2.7(right)), K_{MR} is the negative spring constant and D_{MR} is the virtual damping coefficient. These are the two degrees of freedom of the controller that must be set. Now, if we consider the leg during the stance phase, we can describe the spring extension dynamics (starting from the maximum compression) as a second order spring-mass system where the mass m_{eq} is the equivalent body mass seen by the spring, K_f is the spring mass and F_D is the damping force:

$$m_{eq}\ddot{x}_{FCE} = -K_f x_{FCE} - D_f \dot{x}_{FCE} + F_D \quad (6.2)$$

where D_f is the passive damping introduced by friction in the linear bearing (cfg. Fig.B.13) which has been identified to be $D_f = 226Ns/m$. For the sake of simplicity we neglect the effect of gravity. Further on, by substituting (6.1) into (6.2) the controlled dynamics during the elongation phase becomes:

$$m_{eq}\ddot{x}_{FCE} + (K_f - K_{MR})x_{FCE} + (D_f + D_{MR})\dot{x}_{FCE} = 0 \quad (6.3)$$

From (6.3) we see that the effect of K_{MR} to reduce the stiffness of the passive spring (enables to slow down the extension) while the effect of D_{MR} is to increase the damping (in order to attain critical damping). The natural frequency of the system ω_n and the damping factor ξ can be expressed:

$$\omega_n = \sqrt{\frac{K_f - K_{MR}}{m_{eq}}} \quad \xi_{crit} = \frac{D_{MR} + D_f}{2m_{eq}\omega_n} = \frac{D_{MR} + D_f}{2\sqrt{m_{eq}(K_f - K_{MR})}} \quad (6.4)$$

Since K_{MR} directly affect the natural frequency ω_n , it can be set to have a different elongation settling time t_s ($t_s = 4.6/\xi\omega_n$), this has an impact on the responsiveness of the controller. A higher value of K_{MR} will result in a more compliant dynamics and the energy stored in the spring is dissipated in a longer time interval. On the other hand, if the goal is to damp the oscillation in shorter time, a lower value of K_{MR} must be set. In effect, a smaller K_{MR} means a higher ω_n and thus a smaller settling time. Once K_{MR} has been fixed D_{MR} is chosen to obtain a critically damped response ($\xi = 1$) for which no over-shoot should occur. Having no over-shoot is the necessary requirement to have zero elongation speed when the spring achieves its resting length:

$$D_{MR} = 2\sqrt{m_{eq}(K_f - K_{MR})} - D_f \quad (6.5)$$

To generate the damping force F_D required by (6.1), a current must be driven in the MR coil according to the damper characteristic depicted in Fig.B.15. We need to underline that (6.5)

6. SEMI-ACTIVE DAMPING WITH MAGNETO-RHEOLOGICAL FLUIDS

requires the estimation of the equivalent body inertia m_{eq} seen from the foot spring's point of view. However, a closed form for m_{eq} is very hard to obtain because it depends on the leg configuration and on the foot orientation at the touchdown. Therefore we take advantage of the compression phase during which the controller is not active to identify m_{eq} . In fact after the touchdown the dynamics of the spring compression depends both on the foot compliance K_f on the passive damping of the foot D_f and on the equivalent body mass m_{eq} . Therefore an estimate of the natural frequency can be obtained by using the measurements of the spring displacement. In this method the spring compression time Δt and the maximum spring compression is measured every time the legs land on the ground. The measuring sequence is illustrated in Fig. 6.2. By roughly assuming that Δt is a fourth of the oscillation period of time T of the damped

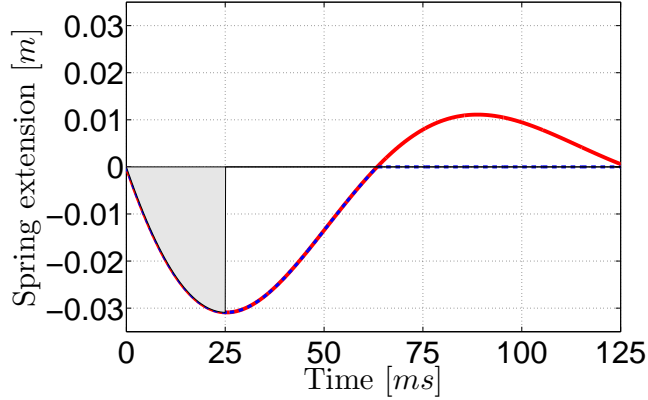


Figure 6.2: Simulation plot showing the damped response of a second order spring-mass-damper system (solid) and the compression of the spring after the impact (dashed). Once the spring has recovered its rest length a mechanical end-stop prevents further extension. The shaded area indicates the duration Δt of the compression phase.

oscillatory response, the damped natural frequency ω_d of the system can be calculated as:

$$T = 4\Delta t \Rightarrow \bar{\omega}_d = \frac{2\pi}{4\Delta t} = \sqrt{\omega_n^2 - \frac{D_f^2}{4m_{eq}^2}} = \sqrt{\frac{K_f}{m_{eq}} - \frac{D_f^2}{4m_{eq}^2}} \quad (6.6)$$

rearranging in function of m_{eq} a second order equation is obtained:

$$4m_{eq}^2 \bar{\omega}_d^2 - 4K_f m_{eq} + D_f^2 = 0 \quad (6.7)$$

the passive damping D_f is known (after earlier identification), $\bar{\omega}_d$ is obtained by the measurement of Δt and m_{eq} can be obtained solving the second order equation and taking the positive root.

6.4 Experimental results

This section presents experimental results using the proposed control law for different values K_{MR} . During the elongation phase of the compliant foot, the total damping force must always be lower than the spring force to prevent that the elongation stops before the maximum extension of the foot spring. This suggests the convenience to express K_{MR} as a fraction of the K_f stiffness by introducing the K_{ratio} variable:

$$K_{MR} = K_f \frac{K_{ratio}}{100} \quad (6.8)$$

The effectiveness of the proposed control law was studied, by free fall experiments, by dropping the leg from 0.3 m. The tests were performed with different values of the parameter K_{ratio} . A test has been performed also with the controller turned off. The body position was measured by the slider displacement and the commanded virtual damping force F_D was also logged. The results of the drop tests are shown in Fig. 6.3. In the figure the slider displacement zero level corresponds to the level of the ground and the time line starts at the moment of touchdown. The experiments show a complete bounce reduction in the case of $K_{ratio} = 50$ and a bounce reduction of 92% and 63% for $K_{ratio} = 30$ and $K_{ratio} = 0$ respectively. 0% bounce reduction represent a perfect elastic impact. In all the cases where the controller was active multiple bouncing is eliminated. On the other hand, when the controller is disabled, the leg rebounds twice and reaches in the first bounce a maximum height of 2.4 cm with respect to ground. As expected $K_{ratio} = 50$ presents the slowest response due to the highest settling time. The fact that $K_{ratio} = 0$ has the highest over-bounce suggests that the damping D_{MR} that has been set is not high enough to achieve a critical damping behaviour. This can be due to a bad estimation of the parameter m_{eq} . Further research work is needed in this particular point. In general even if the control action is implemented at local level (MR foot) satisfactory results are obtained also in the vertical dynamics of the whole leg.

6.5 Generalization

The system considered in the last developments, has only 1 DOF because we were substituting the hydraulic pistons with aluminum rods. Considering the real application on the robot, the hydraulic joints are present and their influence on the dynamics must be taken into account. Indeed the source of compliance is not unique anymore because also the passive actuator compliance and the active compliance of the controller is present. Without any loss of generality the natural frequency can still be estimated during the compression but in this case two un-

6. SEMI-ACTIVE DAMPING WITH MAGNETO-RHEOLOGICAL FLUIDS

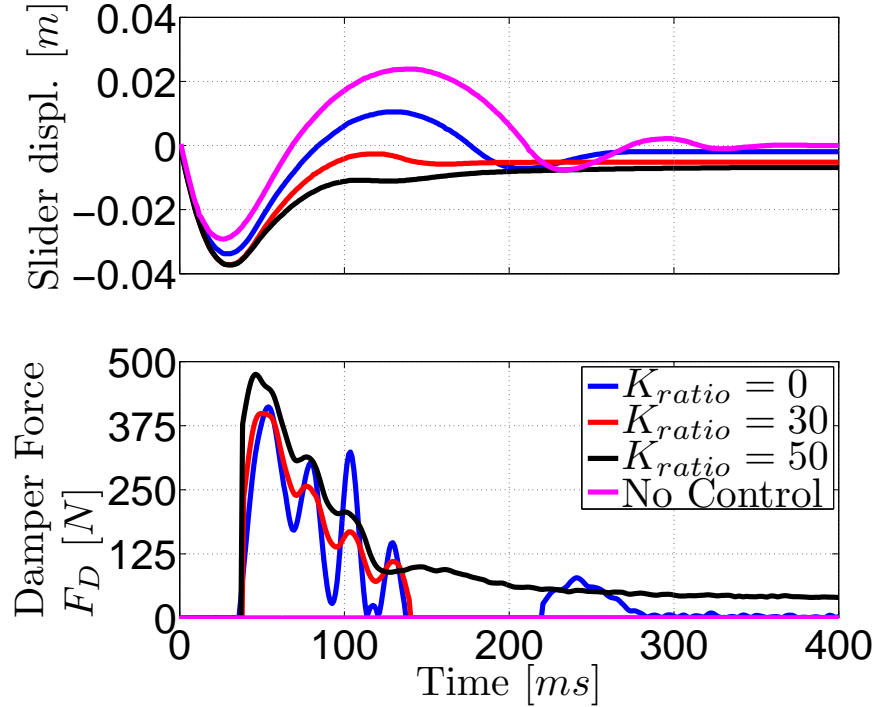


Figure 6.3: Experimental drop tests from 0.3 m height with $K_{ratio} = 0$ (blue), $K_{ratio} = 30$ (red), $K_{ratio} = 50$ (black). The upper plot is the slider displacement while the lower plot is the damper force F_D .

known must be estimated: the parameter m_{eq} and the equivalent stiffness K_{eq} which includes the influence of the hydraulic compliance and of the foot spring. More elaborate identification techniques must be implemented to understand how K_f and the compliance of the controlled actuators contribute to K_{eq} .

6.6 Discussion and limitations

The main drawback of using an MR foot are related to the increased complexity of the system (coil and MR fluid vessel) and to the additional weight (1.25 kg) introduced by the device in point (the foot) which is inconvenient for the leg dynamics. In comparison, the stiff foot is much lighter (0.2 kg) while the passive foot is a little bit heavier (1.35 kg) although the latter enables to fit different types of springs (cfg. Section B.2). The benefits of the proposed control law are limited to the use on dynamic systems where the source of compliance is located in only one joint. More studies must be carried out in the case other compliances (e.g passive compliance, impedance control) are present in the system. Another limitation is related to the

technological design. Figure 6.3 shows that for $K_{ratio} = 50$ the damping force is exceeding 485 N. According to Table B.6 this is the maximum force that the damper is able to generate, therefore the damper reaches the saturation during that experiment. The maximum force is limited by the magnetic field in the steel cylinder. This depends on different factors: a higher field might be achieved either by reducing the fluid channel width (but this would increase the minimum passive damping) or by increasing the current (increasing the power consumption). Alternatively a higher force limit can be achieved by reducing the saturation of the ferro-magnetic material adopting a thicker wall design in the cylinder but this leads to a heavier foot.

6.7 Summary

In this chapter we presented the control and the experimental evaluation of the performances of a novel actively-damped compliant foot (MR foot) for the feet of a quadruped robot. The compliant element in the MR foot, is represented by a linear spring while magneto-rheological technology was used to integrate a semi-active damper into the foot construction. The use of MR fluids demonstrated the feasibility of real-time control of the damping force during single ground contact in which case the traction of the foot can be improved. A control law has been designed to impose a desired dynamics to the spring elongation, which has impact also on the vertical dynamics of the leg, during the stance phase. The aim of the control is to dissipate all the kinetic energy during the first ground contact sequence. To achieve this the damping force of the compliant foot has been commanded in order to emulate a negative spring and a virtual damping element in order to set a critically damped behaviour to the dynamics and reduce the chance of bouncing. We used, as feedback information for the control law, only the spring compression measured by a displacement sensor. The effectiveness of the compliant foot in reducing the bouncing has been assessed by drop-down experiments where the robotic leg, equipped with the MR foot, was fixed to a vertical slider that allowed only vertical motion. The experiments demonstrated the effectiveness of the MR foot in significantly reducing or completely eliminating the bounces. A final discussion analyzed the limitations of the system and pointed out the main drawbacks of the device.

6. SEMI-ACTIVE DAMPING WITH MAGNETO-RHEOLOGICAL FLUIDS

7

Discussion and Conclusions

ALTHOUGH the main results have been already summarized in the sections at the end of each chapter, we would like to condense them in this chapter to draw a general discussion and finally make a few remarks on future directions of the research.

7.1 Discussion

There are still many open questions in the robotics community that must be answered. Defining a set of parameters for the desired impedance as well as the relevant frequency range of operation is an important step before any controller design can be formulated as a meaningful control problem. However this is by no means a trivial problem because most of times there is a lack of understanding of the tasks to be achieved. Therefore, further research is required to understand how to define the desired performances of the impedance controller.

Assuming that a set of specifications is given, the next step is to consider how these specifications can be achieved. In Chapter 4 we showed that in nested loop implementations of the impedance control, increasing the bandwidth of the innermost loop reduces the region of stable impedance parameters (stiffness and damping) that can be set. Even though this seems rather counter-intuitive at a first sight, actually it is not if we think that stability in control system is related to the loop gain of the system. Since we have a nested loop architecture the loop gain of the whole system will depend on both the gains of the two loops (even if an analytical representation of the loop gain is hard to be obtained). Increasing the torque bandwidth is like increasing the loop gain of the inner loop, while setting higher impedance parameters is like increasing the loop gain in the outer loop. Stability depends on the loop gain of the whole system. In particular there is an upper bound to preserve stability. Therefore this explains why if the inner loop gain is increased the system can become unstable for high impedance

7. DISCUSSION AND CONCLUSIONS

gains because they result in a loop gain that exceeds the maximum allowable stable gain for the whole system. On the other hand, a certain amount of torque bandwidth results beneficial to track the impedance in a larger range of frequency. Indeed, increasing the bandwidth improves the tracking of the impedance but only up to a certain "critical" frequency above which further improvements cannot be achieved. As a matter of fact, this limit is related to the inertial effects of the load that start to dominate at high frequency. This issue cannot be circumvented even by choosing actuators with higher bandwidth. This is expected because at high frequencies a higher order system cannot be made to behave as a first ($K + Ds$) or second order system ($K + Ds + Js^2$).

If the locomotion task requires impedance gains that lay in the unstable region, the inner loop bandwidth must be necessarily decreased accepting in exchange, a degradation in the tracking performance of the impedance. Therefore, a trade-off must be found between different requirements: having a reasonably high bandwidth to ensure good impedance tracking, and keeping the bandwidth low to increase the range of stable impedance values that can be rendered.

The analysis done in Section 4.1.3 serves as a basis for quantitative trade-offs, allowing selection of the more suitable controller in each situation. In particular, depending on the value of the desired impedance, a gain scheduler can be implemented to find the value for the bandwidth of the inner loop, that satisfies the requisite of stability and at the same time maximizes the range of frequencies in which the impedance is emulated. In addition, it is worth to remark that the stability regions can change according to the joint configuration in which the system is linearized and therefore a more sophisticated gain scheduling is necessary that takes into account also the different leg configurations in the workspace. The important point is that once the analysis is carried out off-line for the locomotion situation of interest, then a lookup table can be hard-coded in software to be used in the real-time controller.

The region of stable impedance parameters is also affected by averaging filters (e.g to filter velocity signal) or sampling time. In particular it turns out that the region of stable parameters shrinks whenever the sampling time interval increases or the filtering gets stronger. Since both sampling and filtering are time delays, this suggest that the size of the stability region may strongly depend on how much delay is introduced in the control loop. Therefore a good design choice is to have a sampling frequency which is much higher than the loop frequency and then do the filtering or averaging at this higher frequency in order to have a signal that has no delay at the control loop rate. An advantage of the proposed method, that makes use of a detailed model of the system, is that, after an initial experimental identification phase, allows to minimize laborious, trial-and-error experimentation.

To be sure that the robot always remains stable during interactions, it is important to check

7.1. Discussion

if the robot remains always passive in the different situations where the gain scheduler modifies the torques bandwidth or the leg configuration changes. Again the model is an useful tool to check if the controller parameters that have been set, violate the passivity property. In the past passivity has been analyzed using simple models that gave mainly *qualitative* results. The contribution of the proposed approach, based on an accurate model of the system, is that it considers all the kind of non-idealities (actuator dynamics, discrete implementation, filtering, nested loops) and provides *quantitative* results. Stability regions can be represented graphically for a single DOF joint but they become hyper-surfaces in case of more than one joint. Indeed, if we consider the whole leg and the impedance controller implemented at the end-effector, in place of having just two parameters (P_{gain} and D_{gain}) we have six of them which are the parameters on the diagonals of the stiffness and damping matrix, respectively. An analysis of the stability regions and of the passivity considering all the leg joints is part of future works. The fact that the impedance cannot be tracked after a certain frequency means, for example, that the desired stiffness behavior cannot be rendered. In particular, looking at the bode plots if Fig. 4.8 and 4.9, we can see that, at high frequencies, higher load torques (impedance is the transfer function between load position and load torque) are generated in the case of the real impedance with respect to the desired one ($K + D_s$). This is due to the higher roll-off of the real impedance that has an order which is higher than the desired one.

The use of SEAs to control interaction forces introduces problems of bandwidth limitation and uncontrollability (passive dynamic elements are added to the system). The philosophy followed in the design of HyQ, is to use an inherently stiff (hydraulics and geared electric motor) and fast (MOOG valves with high open loop bandwidth) actuation system. If the robot is equipped with torque-controlled joints, the control of interaction forces can be entirely delegated to the impedance controller which shapes the output impedance. In fact an active implementation of the compliance permits to deal with impact forces without having to rely on uncontrollable compliant passive elements.

In this view it becomes of great importance to maximize as much as possible (given the above-mentioned constraints on stability) the range of frequencies where the impedance is emulated. Indeed achieving a large range of frequency where the impedance is tracked, enables to react promptly to the load impacts by controlling the torque via sensor feedback (following the paradigm *stiff inside-soft outside*). In this case, only a limited amount of physical passive compliance at the foot is necessary to reduce the peak forces at the touchdown, that arise due to the limited bandwidth of the impedance controller. As a matter of fact the initial impact is usually very fast and therefore part of its spectrum is out of the range of frequencies (bandwidth) where the impedance controller is able to react. We have shown in Chapter 5 how to select the exact value of this passive compliance to primarily cope with this peak forces while still

7. DISCUSSION AND CONCLUSIONS

taking advantage of the versatility of impedance control when dealing with forces that have a frequency content that is inside the controller bandwidth. This way forces are controlled (or at least reduced) in all the spectrum of relevant frequencies for locomotion . Since the robot is equipped with stiff actuators, this is of great importance because it helps to protect the weakest mechanical components of the leg (gearbox, loadcells), and prevent their damage over time.

Introducing a spring in the leg of a quadruped robot is a delicate task, because it means introducing additional dynamics and possibly unwanted oscillations. These oscillations can lead to chattering/bouncing at the foot with consequent (temporary) loss of traction which is detrimental for locomotion. This oscillations are related to the energy which is stored in the spring after the impact. Active damping is a suitable solution to dissipate this energy before it can generate chattering. Active damping control is not a novel solution in the robotics community [Chew et al., 2004]. A way to actively control the damping force, well-known in the automotive field, makes use of magneto-rheological fluids which are a special kind of smart fluids that change their apparent viscosity by controlling a magnetic field applied to them. We built a hybrid prototype (MR foot) which has a passive spring and a active MR damper designed to control the damping force with an input current. The novelty of our approach is that the control of the damping force is turned off during the compression phase consequent to an impact, taking advantage of the force filtering effect of the passive compliance, while it is activated during the extension phase to dissipate the energy stored in the spring and thus eliminate or reduce the chance of chattering. It is worth to remark that a damper compared with a spring, is a zero order system and would create a very high peak force at the moment of touchdown because the velocity of the foot is not zero. Moreover, the damping force is a "friction" force, thus always opposite to the motion. This means that any damping force during the compression phase would add up to the spring force thus increasing the output impedance. This motivates us to activate the damping force only during the extension phase. In particular the attempt of the implemented critical damping control law is to attain zero elongation velocity when the spring reaches its resting length (the presence of an end-stop prevents further extension). To do this, a local controller is implemented that uses the equivalent robot inertia seen by the foot, estimated by the compression time of the spring. However, the benefits of this proposed control law are limited to the use on dynamic systems where the source of compliance is located only in one joint (e.g. the prismatic joint at the foot). In fact in the experiments, aluminium rods have been used in place of the pistons. If the hydraulic joints are considered, the estimation of the robot inertia must take into account additional sources of compliance (e.g the active compliance due to the impedance controller) and more robust estimation methods must be found. Other drawbacks of the MR foot are the increased complexity of the system (coil and MR fluid vessel) and the weight (1.25 kg) which is added to the foot. Further enhancing the damping

7.1. Discussion

force capabilities is possible at the cost of additional weight. This is due to thicker walls, which must be designed in the damper to increase the saturation point of the material and achieve a stronger magnetic field and so higher damping forces. The stiff foot is much lighter (0.2 kg) in comparison with the built prototypes of passive foot and MF foot. A heavier foot significantly increases the leg inertia thus restricting the impedance bandwidth and the position tracking. The best solution does not exist and the choice depends on the evaluation of the locomotion needs. For instance, if the robot mainly runs on stiff surfaces it is worth to use the passive foot and give up some tracking accuracy to increase the protection level of the loadcells. If very high jumps are needed, an MR foot is beneficial to avoid chatter and loss of traction. If the robot is mainly negotiating natural terrains (e.g grass and forest), which have usually softer surface compliance, a stiff foot might be the best option.

We claimed, in the above discussion, that a higher inner torque bandwidth enlarges the range of frequency in which the impedance is tracked (at least below a certain critical frequency). Therefore trying to achieve a high torque bandwidth is an important control requirement. If no velocity compensation is used, the torque closed-loop performance is limited by the zero introduced in the torque transfer function by the load dynamics when the torque is controlled on a load that is free to move. Considering a PI controller, this zero attracts the pole of the controller integrator and prevents it from going to higher frequencies. This low-frequency pole will be the dominant one and it will limit the responsiveness of the system in closed-loop. The *velocity compensation* is a state feedback that compensates for the natural load velocity feedback in order to make the torque dynamics independent from the load dynamics. This eliminates the intrinsic bandwidth limitation in torque resulting in a system that is easier to control with simple controller structures like a P, PI or PID. In general we can see in (3.6), that the higher the load friction (damping), the higher the frequency of the zero. An alternative solution, to obtain a faster torque without the use of velocity compensation, could be to intentionally introduce damping load-side. However, in the HyQ robot the load friction is mainly due to the bearings on the links and we want to keep it very small to achieve high speed motions. The limiting zero, therefore, is very close to the imaginary axis representing a limit to the bandwidth that cannot be overcome without velocity compensation. Since velocity compensation is a model-based compensation, it is susceptible to parameter uncertainties. Then, a perfect zero/pole cancellation is as challenging as creating a perfect model. In practice, the velocity will be either under or over compensated. In general, it is demonstrated that tuning the velocity compensation gain to have a slight over-compensation it is the best choice in face of parameter uncertainties.

7. DISCUSSION AND CONCLUSIONS

7.1.1 Discrete time

All the proposed controller designs and analysis have been carried out in discrete time. As a matter of fact discrete time implementations can lead to results that are very different from the continuous time implementations. This issue has been often overlooked particularly in many recent publications where often the analysis is carried out in continuous time and using oversimplified models. Then the assumption is that sampling sufficiently fast and "discretizing" the controller will give very similar results to those in the continuous time framework. This is a misconception that is not always true. Sampling always introduces loss of information, time delays (computational and communication), and can also introduce non-minimum phase behaviour (even when the continuous time system is minimum phase). Some of these problems become more significant as the sampling time is reduced. As a matter of fact it is not difficult to give examples of linear feedback control systems that show an infinite gain margin when implemented as continuous time controllers but have a finite gain margin when implemented in discrete time. Therefore it is crucial to consider the discrete time domain when the purpose is to investigate the real control performances of the system.

7.1.2 Open-loop actuator dynamics vs power limitation

In this section we will investigate whether the actuator dynamics (in our case the electric motor) should be included in the model for the purpose of controlling the torque. A generic force/torque control problem can be generalized considering only three elements: a velocity source, a transmission, and a load [Boaventura et al., 2012a]. In the case of the hydraulic joints, the velocity source is the pump and valve together. The pump pressurizes the fluid and the valve controls the fluid flow that is going into the hydraulic cylinder. We can consider the supply line as perfect pressure source. Therefore, the velocity source dynamics is determined only by the valve and flow dynamics, while the transmission stiffness depends on the fluid compressibility and volume. In the case of HyQ, very fast (MOOG) proportional valves are used whose dynamics can be neglected. Indeed this dynamics is constant in terms of gain and phase up to 250Hz [MOOG Inc., 2003]. Thus they can be considered ideal velocity sources in the range of frequencies of interest (which for legged robot locomotion is lower than 250 Hz). In the case of electric actuators the velocity source is the rotor while the transmission is the gear box. Looking at the parameters in Table 3.1, it is possible to see that the inherent open loop bandwidth of the rotor inertia (motor dynamics) is very low. The transfer function

between current and motor velocity:

$$\frac{\dot{\theta}_m(s)}{I_m(s)} = \frac{k_t}{J_m s + B_m} \quad (7.1)$$

has a pole ($s = -\frac{B_m}{J_m} = -26 \text{ rad/s}$) at low frequency. Due to the small open loop bandwidth the electric motor cannot be considered as an ideal velocity source and its dynamics must be necessarily incorporated in the model of the system.

Ideally with a good design of the controller it could be possible to achieve high control bandwidth even with a low-bandwidth actuator (as *actuator bandwidth* we consider the open loop one). In fact a feedback controller could ideally move the system poles to any desired location. However, the real limitation to the closed loop bandwidth is not the open loop actuator bandwidth (which can be low) but the power saturation of the actuator.

A rule of thumb can be drawn from the above discussion: unless the actuator bandwidth is an order of magnitude larger than the desired bandwidth we want to target, then the actuator dynamics cannot be neglected for the synthesis of the controller and must be included in the model of the system.

7.1.3 Safety: active vs passive compliance

One of the main motivations for using SEAs is to improve safety in the interaction with humans. This is a very common misconception in the VSA and SEA robotics community that often results from a quite superficial analysis. First of all we need to properly clarify what human-robot safe interaction is. Safety is related to the magnitude of the force that arise from the interaction between the human and the robot. The statement that compliant drive trains are inherently safe since they do not produce the large impact loads associated with high impedance designs [Shin et al., 2008], is not necessary true. As a matter of fact the impact force depends on the velocity and on the "unsprung" mass/inertia located "after" the spring. Furthermore, the fact that a passive compliance is located between this mass and the actuator, it means that we completely lose controllability on this unsprung mass. In addition to this, if the SEA is located in the more proximal links of a robot (e.g. the hip for the HyQ robot), the "unsprung" mass becomes significant and so an eventual impact load. In fact, the controller has no authority on the uncontrollable mass. So the statement that a spring in series to an actuator improves safety is in general incorrect. Conversely a higher bandwidth control with stiff actuators can increase the safety because the robot is able to promptly stop/deviate if required.

7. DISCUSSION AND CONCLUSIONS

7.2 Conclusions

The goal of this thesis was to improve the control of interaction forces during locomotion of a legged robot with the aim to make the robot more robust and safe. Following goals have been reached to meet the final objective:

- A detailed model of the abduction-adduction joint has been built including, actuator dynamics, filters, discrete implementation.
- A compensation strategy (*velocity compensation*) has been proposed to eliminate the intrinsic bandwidth limitation that arise when controlling the torque on a load that is free to move. The result, after the compensation, is a system that is easier to control for which good control performance (high torque bandwidth) can be achieved by using well-established and less sophisticated controller structures like a P, PI or PID.
- The concept of velocity compensation has been extended to a more general case which is independent by the actuator technology.
- Considering the impedance control implemented with an inner torque loop, a methodology was presented to compute the influence of inner loop bandwidth, filters, sampling time and velocity compensation on the region of stable impedance parameters and on passivity.
- The widespread believe that the bandwidth of the innermost loop must be always maximized in designing nested loop control systems has been negated. In particular has been shown that a trade-off must be found between different requirements: having a high bandwidth to ensure good impedance tracking, and keeping the bandwidth low to increase the range of stable impedance values that can be rendered.
- Implementation of impedance control for the whole leg both at joint and at end-effector level. For the end-effector implementation some procedures or rule of thumb were suggested to quantitatively select the impedance parameters according to locomotion requirements.
- A procedure was outlined to select the minimum amount of passive stiffness to be introduced at the foot to protect the structure from the peak impact forces that occur when the robot is equipped with low bandwidth actuators or when the input forces have a frequency content higher than the bandwidth of the impedance controller.

- A novel solution to dissipate the energy stored in the compliant element was presented (MR foot). The purpose is to improve foot traction by eliminating the chattering than can occur after an impact, by actively controlling the damping force via magneto-rheological fluids.

7.3 Future works

The design of a high performance low-level controller is just the first step in the evolution of a legged robot. The implemented controller will be the base on top of which higher level locomotion tasks will be implemented (e.g. push recovery). The following list includes a selection of these future activities related to impedance control:

- Perform the analysis of the stability regions and of the passivity considering all the leg joints (MIMO case).
- Since the leg is a not linear system, the analysis must be repeated for different leg configurations in order to cover the whole workspace.
- Design of a gain scheduling approach to adapt the bandwidth of the inner torque controller that satisfies passivity and stability, according to the impedance parameters set by the user, while maximizing the range of frequency where the impedance is tracked (impedance bandwidth).
- In this work impedance control at the end-effector has been implemented neglecting the mutual interactions between the legs. Future implementations of impedance control will be considering these mutual interactions.
- Better investigate how to specify the impedance parameters for locomotion, and develop a more systematic approach to specify performances that take into account the fact that the leg inertia is different during the stance and the swing phase.

7. DISCUSSION AND CONCLUSIONS

Appendix A

Miscellaneous mathematical derivations

A.1 Derivation of the velocity compensation gain for the model with two inertia

In this section the velocity compensation gain $VC(s)$ to compensate for the load dynamics will be derived. This is related to the development introduced in section 3.4.3. For the following derivation we recall the expression of the torque derivative (3.9):

$$\dot{T}_l = K_{te} \left(\frac{\dot{\theta}_m}{N} - \dot{\theta}_l \right) \quad (\text{A.1})$$

and the dynamics of the electric motor (first of (3.1)) where the current variable I_m is expressed as function of the voltage:

$$J_m \ddot{\theta}_m + B_m \dot{\theta}_m + \frac{k_w k_t}{R} \dot{\theta}_m + T_l = k_t \frac{V_m}{R} \quad (\text{A.2})$$

The electrical dynamics has been ignored because the following derivation is for the model with two inertia that was not considering it. However similar relations can be obtained if the electrical dynamics is included. If we take out $\dot{\theta}_m$ from (A.2) and substitute into (A.1) we

A. MISCELLANEOUS MATHEMATICAL DERIVATIONS

obtain:

$$\dot{\theta}_m = \frac{\frac{V_m k_t}{R} - T_l}{\underbrace{(B_m + \frac{k_w k_t}{R}) + J_m s}_P} \quad (\text{A.3})$$

$$\dot{T}_l = \frac{K_{te} k_t V_m}{NRP} - \frac{K_{te} T_l}{P} - K_{te} \dot{\theta}_l \quad (\text{A.4})$$

$$\dot{T}_l \underbrace{\left(1 + \frac{K_{te}}{sP}\right)}_Q = \frac{K_{te} k_t V_m}{NRP} - K_{te} \dot{\theta}_l \quad (\text{A.5})$$

$$\dot{T}_l = \frac{1}{Q} \frac{K_{te} k_t V_m}{NRP} - \frac{1}{Q} K_{te} \dot{\theta}_l \quad (\text{A.6})$$

To find the velocity compensation gain we need to determine the extra-voltage that must be applied to the motor to have a motion that compensates for load motion. In other words we want to make the torque dynamics (A.1) independent from the load velocity $\dot{\theta}_l$. This is equivalent to set the constraint $\dot{T}_l = 0$ on (A.6):

$$\begin{aligned} V_{m_{VC}}|_{\dot{T}_l=0} &= \frac{NRP}{k_t} \dot{\theta}_l \\ V_{m_{VC}} &= \frac{N}{k_t} [R(J_m s + B_m) + k_t k_w] \dot{\theta}_l = VC(s) \dot{\theta}_l \end{aligned} \quad (\text{A.7})$$

from this the expression of the velocity compensation gain can easily be obtained:

$$VC(s) = \frac{N}{k_t} R(J_m s + B_m) + k_t k_w \quad (\text{A.8})$$

A.2. Derivation of the torque transfer function for the model with three inertia

A.2 Derivation of the torque transfer function for the model with three inertia

In this section we will describe the derivation of the transfer function (3.20) from voltage V_m to torque T_l for the model with three inertia. Gravity effects will not be taken into account here. Firstly we rewrite the system dynamic equations (3.18) in matrix polynomial form:

$$M = \begin{bmatrix} J_{L2}s^2 + B_{L2}s + D_p s + K_p & -(D_p s + K_p) & 0 & 0 \\ -(D_p s + K_p) & J_{L1}s^2 + (B_{L1} + D_p + D_{te})s + K_p + K_{te} & -\frac{1}{N}(D_{te}s + K_{te}) & 0 \\ -\frac{1}{N}(D_{te}s + K_{te}) & 0 & J_m s^2 + B_m s + \frac{1}{N^2}(D_{te}s + K_{te}) & -k_t \\ 0 & 0 & k_w s & Ls + R \end{bmatrix} \quad (\text{A.9})$$

where:

$$M \begin{bmatrix} \theta_{L2} \\ \theta_{L1} \\ \theta_m \\ I_m \end{bmatrix} = \begin{bmatrix} T_{dist} \\ 0 \\ T_{fr} \\ V_m \end{bmatrix} \quad (\text{A.10})$$

$$\begin{bmatrix} \theta_{L2} \\ \theta_{L1} \\ \theta_m \\ I_m \end{bmatrix} = M^{-1} \underbrace{\begin{bmatrix} 0 \\ 0 \\ 0 \\ V_m \end{bmatrix}}_{M_{adj}} = \frac{1}{\Delta} \begin{bmatrix} x & x & x & a \\ x & x & x & b \\ x & x & x & c \\ x & x & x & d \end{bmatrix} \begin{bmatrix} 0 \\ 0 \\ 0 \\ V_m \end{bmatrix} \quad (\text{A.11})$$

where $\Delta = \det(M)$, and a, b, c, d are the cofactors of the last row in the matrix M . M_{adj} is the adjoint matrix (the transpose of the cofactor matrix) of M . For the input V_m a, b, c, d are the

A. MISCELLANEOUS MATHEMATICAL DERIVATIONS

only entries that must be computed. After some algebra we get:

$$\begin{aligned}
 a &= \frac{k_t}{N} (D_p s + K_p) (D_{te} s + K_{te}) \\
 b &= \frac{k_t}{N} (D_{te} s + K_{te}) (J_{L2} s^2 + B_{L2} s + D_p s + K_p) \\
 c &= K_{te} (J_{L2} s^2 + B_{L2} s + D_p s + K_p) (J_{L1} s^2 + B_{L1} s + D_p s + K_p + D_{te} s + K_{te}) \\
 &\quad + K_{te} (J_{L2} s^2 + B_{L2} s) (D_p s + K_p) \\
 d_1 &= (J_{L1} s^2 + B_{L1} s) (J_m s^2 + B_m s + \frac{D_{te} s + K_{te}}{N^2}) + (J_m s^2 + B_m s) (D_{te} s + K_{te}) \\
 d &= (J_{L2} s^2 + B_{L2} s + D_p s + K_p) d_1 + (J_{L2} s^2 + B_{L2} s) (D_p s + K_p) J_m s^2 + B_m s + \frac{D_{te} s + K_{te}}{N^2}
 \end{aligned}$$

then the relevant transfer functions can be found:

$$\begin{aligned}
 \theta_{L2}(s) &= \frac{a}{\Delta} V_m(s) \\
 \theta_{L1}(s) &= \frac{b}{\Delta} V_m(s) \\
 \theta_m(s) &= \frac{c}{\Delta} V_m(s) \\
 I_m(s) &= \frac{d}{\Delta} V_m(s)
 \end{aligned} \tag{A.12}$$

The determinant of M can be expressed in terms of the cofactors c and d :

$$\Delta = d(Ls + R) + ck_w s \tag{A.13}$$

To obtain the transfer function between voltage and torque we need to express the torque as linear combination of the state variables $T_l = (K_{te} + sD_{te}) \left(\frac{\theta_m}{N} - \theta_{L1} \right)$ and substitute the (A.12):

$$G_t = (D_{te} s + K_{te}) \left(\frac{\theta_m}{N} - \theta_{L1} \right) = \frac{1}{\Delta} (D_{te} s + K_{te}) \left(\frac{c}{N} - b \right) \tag{A.14}$$

A.3. Derivation of the torque transfer function for the model with three inertia, with velocity compensation

After some algebraic manipulations the transfer function G_t can be expressed as:

$$G_t = \frac{k_t p_1}{N \Delta} (D_{te}s + K_{te}) \quad (\text{A.15})$$

where:

$p_1 = (J_{L2}s^2 + B_{L2}s)(J_{L1}s^2 + B_{L1}s) + [(J_{L2}s^2 + B_{L2}s) + (J_{L1}s^2 + B_{L1}s)](D_p s + K_p)$ The determinant Δ , which is the characteristic polynomial of G_t it can also be expressed in terms of the polynomial p_1 :

$$\Delta = p_1 q_1 + q_2 q_3 \quad (\text{A.16})$$

where:

$$\begin{aligned} q_1 &= (Ls + R) \left(J_m s^2 + B_m s + \frac{D_{te}s + K_{te}}{N^2} \right) + k_t k_w s \\ q_2 &= \frac{N}{k_t} (Ls + R)(J_m s^2 + B_m s) + N k_w s \\ q_3 &= \frac{k_t}{N} (J_{L2}s^2 + B_{L2}s + D_p s + K_p)(D_{te}s + K_{te}) \end{aligned} \quad (\text{A.17})$$

A.3 Derivation of the torque transfer function for the model with three inertia, with velocity compensation

This section describes the derivation of the transfer function (3.24) from voltage V_m to torque T_l for the model with three inertia, when the positive feedback of the velocity compensation is closed. The gravity effects also be taken into account. First consider the positive feedback loop (3.23):

$$V_{m_{VC}} = \frac{N}{k_t} [(Ls + R)(J_m s + B_m) + k_t k_w] \dot{\theta}_{L1} = VC(s) \dot{\theta}_{L1} \quad (\text{A.18})$$

This has been obtained with a derivation similar to section A.1) including the electrical dynamics because, differently from the model with two inertias, this is present in the model with three inertias. Closing the the positive feedback loop creates an entry $-VC(s)s$ in the

A. MISCELLANEOUS MATHEMATICAL DERIVATIONS

system matrix M (A.9) that changes to:

$$M = \begin{bmatrix} J_{L2}s^2 + B_{L2}s + D_p s + K_p + K_{L2} & -(D_p s + K_p) & 0 & 0 \\ -(D_p s + K_p) & J_{L1}s^2 + (B_{L1} + D_p + D_{te})s + K_p + K_{te} & -\frac{1}{N}(D_{te}s + K_{te}) & 0 \\ -\frac{1}{N}(D_{te}s + K_{te}) & 0 & J_m s^2 + B_m s + \frac{1}{N^2}(D_{te}s + K_{te}) & -k_t \\ 0 & -VC(s)s & k_w s & Ls + R \end{bmatrix} \quad (\text{A.19})$$

We recall that the influence of the gravity is represented by the term K_{L2} in the load dynamics. After closing the positive feedback, the new closed loop characteristic polynomial (computed with the cofactor determinant rule) is:

$$\Delta_{VC} = \Delta - VC(s)s q_3 = p_1 q_1 + q_2 q_3 - VC(s)s q_3 = p_1 q_1 + (q_2 - VC(s)s) q_3 \quad (\text{A.20})$$

Since the positive feedback affects only the last row of M , the cofactors b and c in (A.14) are not changed. Therefore the torque transfer function with velocity compensation becomes:

$$G_{tvc} = \frac{k_t(D_{te}s + K_{te})p_1}{N(p_1 q_1 + (q_2 - VC(s)s) q_3)} \quad (\text{A.21})$$

where:

$$\begin{aligned} p_1 &= (J_{L2}s^2 + B_{L2}s + K_{L2})(J_{L1}s^2 + B_{L1}s) \\ &\quad + [(J_{L2}s^2 + B_{L2}s + K_{L2}) + (J_{L1}s^2 + B_{L1}s)](D_p s + K_p) \\ q_1 &= (Ls + R) \left(J_m s^2 + B_m s + \frac{(D_{te}s + K_{te})}{N^2} \right) + k_t k_w s \\ q_2 &= \frac{N}{k_t} (Ls + R)(J_m s^2 + B_m s) + N k_w s \\ q_3 &= \frac{k_t}{N} (J_{L2}s^2 + B_{L2}s + D_p s + K_p + K_{L2})(D_{te}s + K_{te}) \end{aligned}$$

Appendix B

Design of components

B.1 Six axis foot sensor design

This section describes the mechanical design of a six axis foot sensor that has the purpose to measure the ground contact forces during locomotion. A sensor is located at the tip of each foot of the HyQ robot.

B.1.1 Specifications for a six axis foot sensor

Before carrying out the design it is important to determine which are the specifications required for the force sensor according to the intended use. In our case, HyQ has been designed for being a versatile robot platform; this means that it must be able to perform highly dynamic motions, such as running and jumping, but also careful navigation over very rough terrain [Semini et al., 2011c]. For this reason the different requirements of ruggedness and high force resolution must be met at the same time. The specifications for the sensor are detailed in Table B.1. The range of forces and the maximum overload is determined by simulating the ground interactions for very dynamic locomotion scenarios and inspecting the experimental data of the actual locomotion experiments. Specification for torques are not reported because torques measurements are not of interest, since the robot has point feet. To the knowledge of the authors there is no commercial sensor available in the market that meet these specifications. This strongly motivated the design of a custom one.

B. DESIGN OF COMPONENTS

Table B.1: Six axis foot sensor specifications.

SP.1	Force range X, Y [N]	1000
	Force range Z [N]	2000
SP.2	Maximum overload X, Y [N]	2000
	Maximum overload Z [N]	4000
SP.3	Weight [kg]	< 0.1
	Maximum diameter [m]	0.05
SP.4	Noise to Signal ratio	low
SP.5	Linearity	high
SP.6	Temperature sensitivity	low

B.1.2 Selection of the sensing technology

The most common way to measure a force is by measuring the elastic deformation of a mechanical element which deflects under the load of the force. To capture this deformation, several sensor principles are used according to different physic principles depending on the nature of the sensing element. The range of possible solutions is vast: force sensors can be implemented based on capacitive or resistive change, on piezoelectric or on optical interpherometry [[Broistedt et al., 2009](#)]. Because of its ruggedness and simplicity we decided to select the strain-gauge technology which is the most well-established and widespread force transducer technology. Strain gages are devices which vary in resistance as strain is applied to them. Gages made from semiconductor materials have advantages over more conventional (foil) types strain-gages. Namely semiconductor gages provide an output signal which is 25 to 50 times higher, have greater durability, longer service life, and a very low noise output.

Table B.2: Semiconductor strain-gages characteristics.

Operating Strain [μstr]	± 2000
Linearity	better than $\pm 1.5\%$ for $1500 \mu m / mm$
Gage factor	140
Resistance R [Ω] (at $25^\circ C$)	500 ± 50
Temperature standard matching	$0.6\%R$

On the other hand foil gauges remain popular due to their lower cost and the desirable feature of being less affected by environmental temperature changes. However, the benefits of foil gauges as it relates to temperature changes become evident only when extreme temperature changes occur. Therefore, as core technology for the force sensitive elements, we choose semiconductor strain-gages. The mechanical/electrical properties of the selected gage are reported

B.1. Six axis foot sensor design

in Table B.2.

A CAD view of the sensor with the local coordinate frame (*footframe*) is illustrated in Fig. B.1 (left).

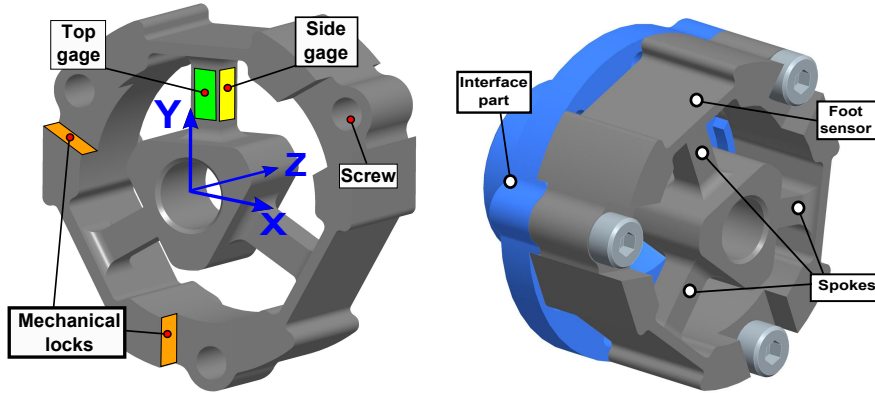


Figure B.1: Foot sensor: CAD isometric view (left). The green and the yellow areas highlight the position of gages on the top and the side of a spoke. The blue arrows indicate the coordinate frame (*foot frame*) in which the forces are measured. An interface part enable to preserve the calibration when the sensor is mounted (right).

To define the number of gages and their location in the sensor we need to consider which are the forces we intend to measure with the sensor. As previously anticipated, because we have point feet, we are only interested in the Cartesian (X, Y, Z) forces not in the torques. Therefore, three gages may seem enough to estimate the Cartesian forces. However, since there is an offset between the contact point (at the foot tip) and the center of the spokes (which is the center of the foot sensor frame), torques arise together with the forces. Gages are just measuring deformations and are not able to discriminate between torques and forces. Therefore, to correctly estimate the three Cartesian forces and also the three torques (about the axis of the *sensor frame*), at least six gage are necessary (six unknowns). These gages will be glued on the top and side face of the three spokes as depicted in Fig. B.1 (right). The central cylindrical part is where the foot tip is mounted. The actual design with spokes ensures that there is no contact between the inner cylindrical part and the outer support part. This allows that all load forces are transmitted only through the spokes creating deflections that can be measured by the gages.

B.1.3 Design guidelines

To achieve the specifications listed in Table B.1, some design guidelines have been followed. Each guideline is related to a particular specification:

B. DESIGN OF COMPONENTS

- **SP.1, SP.2 and SP.5: Material choice** The material of the sensor must be selected considering that the stress created by the maximum overload forces (see Table B.1 SP.2) should be lower than the yield stress point (to remain inside the range of elasticity of the material). Regarding the deformations generated by the range of nominal forces (SP.1), they must be in the range of linearity of the gage (see Table B.2). We chose a special steel alloy with good machinable characteristics together with a high yield stress ($\sigma = 540MPa$) and stiff elastic modulus ($E = 210GPa$). Then we performed a *FEM* optimal analysis to find the dimensions of the cross section of the spokes that maximize the sensor sensitivity given the mechanical characteristics of the alloy. This means have the maximum deflection of $1000 \mu_{str}$ (where a 0.5% linearity is ensured) in correspondence of the maximum nominal forces defined in SP.1 (2000 N for Z and 1000 N for X and Y). After the dimensions were selected we checked that the maximum overload forces (SP.2) were creating stress within the limit of the material. From the design point of view we added rounds to smooth the sharp edges of the spokes in the places where these discontinuities would result in stress accumulation points.
- **SP.3: the sensor must be easily embeddable in the lower leg link and easily replaceable.** Whenever the sensor is dismounted by the leg and mounted again, small residual stress can arise in the material that would invalidate the calibration. For this reason in order to preserve the calibration of the sensor even if this is dismounted from the leg, an interface part (see Fig. B.1) has been designed. Indeed, the calibration of the foot sensor is done together with the interface part (see Section B.1.4).
- **SP.4: Minimize noise and maximize sensitivity.** To increase the signal strength, instead of one single element, a pair of gages is used to measure spoke deformation. Each pair of gage is glued on opposite side face of each spoke. This way, a spoke deformation that compress one gage, will stretch the other that is glued on the opposite face. If a half-bridge (Wheatstone) arrangement is used (Fig. B.2). this arrangement will result in a output voltage that has double amplitude respect to read a single sensing element. Therefore 4 gages are glued in 2 pairs on top-bottom left-right faces of each spoke, resulting in a total of 12 gages for the whole sensor with 6 analog output signals. The signal coming out from the 6 half-bridges are then connected (trough wire) to the electronic conditioning board (Fig. B.2). As nomenclature we will call P1, P2, P3 the gage pairs that are on the side (left-right) of the spokes while P4, P5, P6 the pairs that are on top-bottom faces.

To improve the signal to noise ratio these wires must be as short as possible. This requires that the amplification of the signals must be done close to the sensing elements.

B.1. Six axis foot sensor design

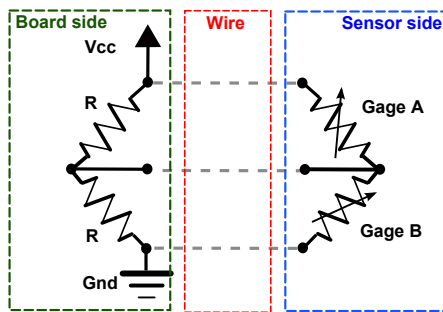


Figure B.2: Wiring of the gages in a half-wheatstone bridge arrangement.

This enhances robustness in face of electro-magnetic noise that can couple the cable that connects the board to the acquisition board that is generally located in the the torso of the robot (far away from the sensor). A circular 3 cm diameter custom electronic board amplifies the 6 outputs coming from the gages of the sensor (6 channels). The board is designed to be fit on the top of the inner cylindrical part, in a dust-protected space between the sensor and the interface part. A thin layer of rubber is placed under the board to damp vibrations that could be induced by the impacts and provide electrical insulation. The electric signals after the amplification, are passed through an analog filter (cut frequency 250 Hz) to further decrease the noise level.

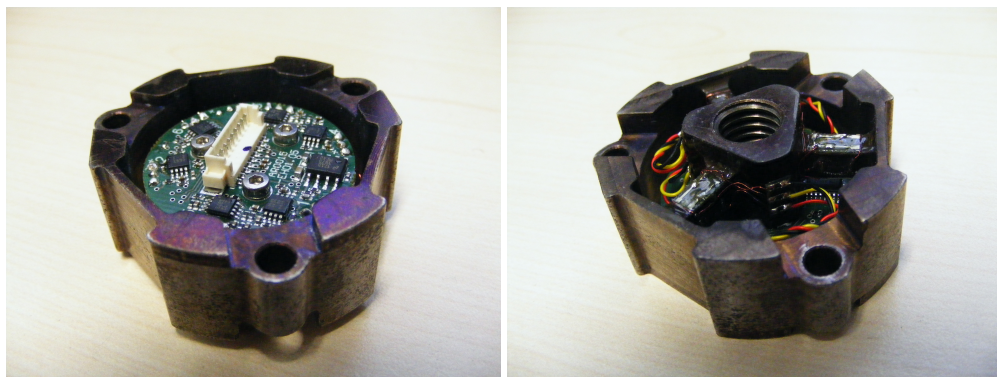


Figure B.3: Picture of the sensor prototype. View from the top (left) and from the bottom (right). The amplification board is located on the top of the sensor.

- **SP5: Minimize load-dependent offsets and hysteresis.** Load-dependent offsets and hysteresis in force sensors are mainly due to residual stress that change with load direction and intensity. This is often related to the design of the interface connection of the sensor with the rest of the robot. If this interface is not completely stiff and micro-movements are possible, then a hysteresis can appear in the force signal. Let us illustrate

B. DESIGN OF COMPONENTS

this with a simple example. Whenever two parts are connected together by screws (e.g the sensor and its interface), typically one part has the thread where the screw is inserted while the other one has a hole which has a diameter that is larger than the screw itself. If a torque is applied around an axis perpendicular to the surface between the parts, unless different solutions are adopted, the friction between the surfaces is how the torque is transmitted. Friction depends on the normal force which depends on the tightening of the screw. Even with high tightening, whenever high loads are applied, stick-slip micro-movements can occur between the parts. These micro-movements are responsible for hysteresis that will be present in the torque measurement. To solve this issue, tightly tolerance machined mechanical locks (teeth) have been designed to transmit the forces from the sensor to the lower leg (see Fig. B.1(right)). The screws have the only function to keep the parts together not to transmit the force. Thanks to the mechanical locks solution, time-varying load-dependent offsets are eliminated. However some offsets are still present that are due to the light press-fit mounting. These offsets are constant and can be compensated in the amplification board.

- **SP.6: Matching of thermal coefficient for temperature compensation.** The half-bridge arrangement, besides doubling the sensitivity, has also the purpose to perform common-mode temperature compensation. In fact, drift due to temperature changes is the main drawback of using semi-conductor gages. We measured the behavior of each gage at different temperatures estimating the *temperature coefficient*. Then we matched the gages in pairs that have the same temperature coefficient. If the thermally matched pair is connected with a half-bridge arrangement, the resistance variation due to a temperature change, will create the same voltage offset across both gages. This common mode disturbance will be rejected thanks to the differential measurement of the bridge. Thus with a half-bridge measurement meant the only requirement to have temperature compensation is that the pair of gages has temperature coefficients that match in the range of operation temperatures.

B.1.4 Calibration

An Easydur MZ3 material testing device (stress-strain machine) (see Fig B.4 (right)) has been used for the calibration of the sensor. The motivation to use a stress strain machine instead of simple weights, to generate calibration forces, is that the nominal range of forces (SP.1) would be difficult to achieve with weights (for a 1000 N force is a 98 kg weight is needed which can be very bulky to handle). The drawback is that a slight misalignment of the pressing stick of the machine can create a force that is not perfectly aligned with the desired calibration direction.

B.1. Six axis foot sensor design

Therefore a commercial 6 axis force sensor (Mini 45 ATI) is rigidly connected in series to our sensor and the calibration forces are applied to this via an appropriate interface part. Since the two sensors are connected together they will be subjected to the same forces/torques (with a small offset which will be considered) and the measures of the ATI sensor can be taken as the true references for the calibration. A custom calibration test-rig with an adjustable plate (see Fig.B.4 (left)) has been designed to enable the positioning of the sensors inside the stress strain machine, in order to be able to apply forces in the X , Y and Z direction. Calibrating the sensor

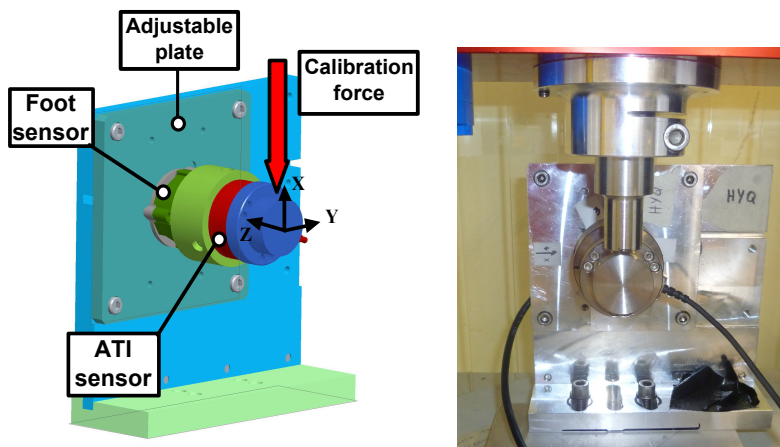


Figure B.4: CAD view of the test rig with the mini 45 ATI commercial sensor for calibration (left). Picture of the calibration test-rig inside the Easydur MZ3 stress-strain machine (right).

means to identify the 6×6 transformation matrix that permits to convert the sampled voltage data coming from the strain gauges into the associated torque/force values expressed in the foot frame. To obtain a well conditioned transformation matrix (e.g. to avoid zero entries) an exhaustive coverage of the cartesian force space is required. This means that different forces must be applied in the X , Y , and Z directions that cover the nominal range specified in SP.1. The calibration is carried out repeating the following procedure for each force of the calibration set:

- Collect static measurements (forces/torques) from the ATI sensor. These forces are defined in the coordinate frame of the ATI sensor and must be mapped (by homogeneous transformation) into the *foot frame*. The foot frame is aligned with the ATI sensor frame but has the origin in the geometric center of the foot sensor.
- Collect the 6 voltage reading (after averaging filtering) from the gage channels.

The vector of forces/torques are stacked as rows of the *force matrix* \mathbf{F} while the relative voltage readings from the gage channels are the rows of a matrix called *channel matrix* \mathbf{C}_h . The

B. DESIGN OF COMPONENTS

transformation matrix \mathbf{T} can be obtained by:

$$\mathbf{T} = \mathbf{C}_h^\dagger \mathbf{F}; \quad (\text{B.1})$$

where \mathbf{C}_h^\dagger is the Moore-Penrose pseudo-inverse. Using the Moore-Penrose pseudo-inverse is equivalent to solve a least square fitting problem. Then, during the normal robot operation, given a 6×1 vector of voltage readings V the relative force/torque vector F can be obtained as follows:

$$\mathbf{F} = \mathbf{T}^T \mathbf{V} \quad (\text{B.2})$$

B.1.5 Experimental results

B.1.5.1 Static tests

In this section we report the experiments that have been carried out to demonstrate the effectiveness of the foot sensor in static considerations. Figure B.5 shows the plots of the voltage outputs of the six channels associated to static input forces ranging from 0 to 500 N in X,Y direction and from 0 to 1000 N for Z direction. The linearity of the sensor can be quantitatively evaluated by looking at the maximum residuals between the samples's data and estimated data as given in Table B.3. The values are scaled as percentage of the full scale range that is 2000 mV. The result show a better linearity for the forces applied in Z direction. We hypothesize this is related to the fact that, due to the topology of the sensor, Z forces create pure flexural deformations on all the spokes while forces in X,Y direction can induce also torsional deformation, leading to a less-linear static response of the sensor. From the data presented in Fig. B.5 we

Table B.3: Maximum residuals of the gage voltages for the forces in Fig B.5. The values are expressed as percentage of the full scale voltage range.

Channel	X direction [%]	Y direction [%]	Z direction [%]
P1	0.185	0.135	0.03
P2	0.086	0.07	0.01
P3	0.35	0.115	0.005
P4	0.32	1	0.087
P5	0.8	0.435	0.0665
P6	0.95	0.365	0.06

identified the transformation matrix T . To assess the quality of the identification we carried out

B.1. Six axis foot sensor design

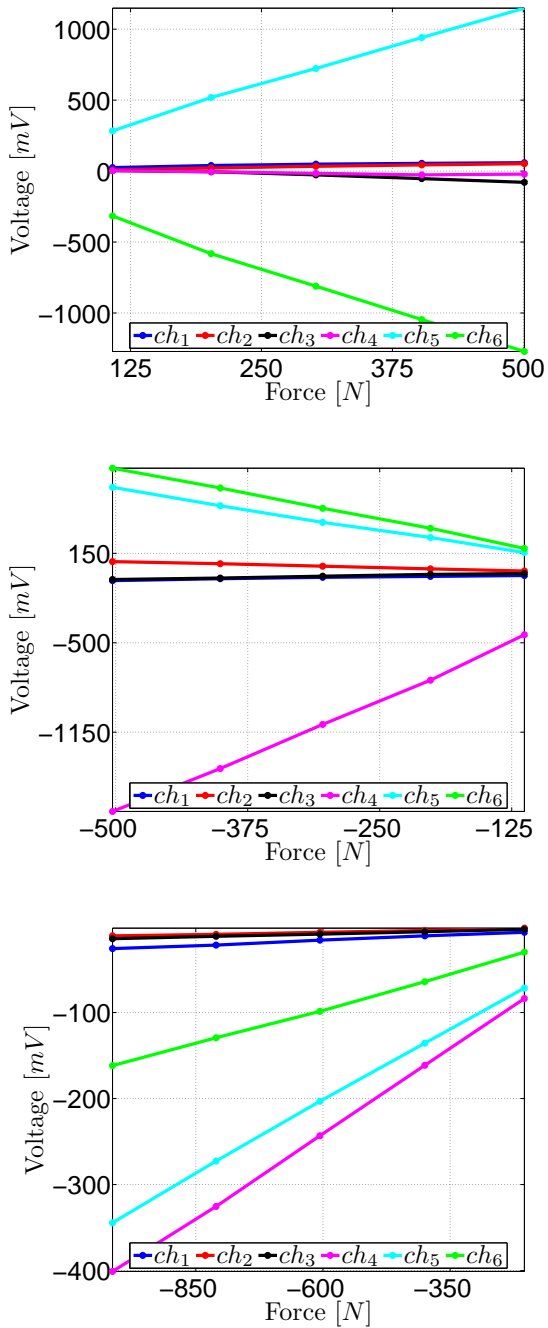


Figure B.5: Static responses of the gage voltages (6 channels) for a range of forces in X (left plot), Y (middle plot) and Z (bottom plot) direction. Circles indicate the sampled data points.

B. DESIGN OF COMPONENTS

validation tests by comparing the output of our sensor with the one of the ATI sensor using a different set of data. Then we computed the error between the two force vectors. This has been

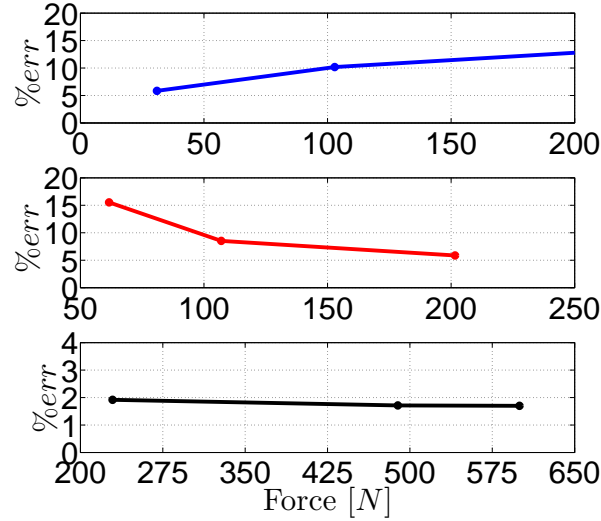


Figure B.6: Norm of the error vector from the validation expressed as percentage of the norm of the applied force. Tests for X (upper plot), Y (middle plot) and Z force direction (lower plot).

repeated for different force magnitudes and directions. In particular, forces ranging from 0 to 200 N have been applied for the X and Y direction while forces ranging from 0 to 600 N for the Z direction. Then we computed the euclidean norm of the force error vector and expressed it as a percentage of the norm of the applied force vector for each measurement. The results reported in Fig. B.6 show that error is always below 1.7% for Z direction while below 15% for X and Y directions. We suppose this has to do with the more complex deformation distribution discussed above. Further reducing these errors, in order to achieve a more reliable force for the estimation of the friction cone, is part of an ongoing work.

B.1.5.2 Dynamic tests

To complete the evaluation of the sensor performances, we carried out dynamic drop tests on the experimental setup made by the real leg attached to the vertical slider (see Fig. B.7). The foot sensor is attached to the tip of a rigid stiff foot, which is attached to the lower leg link. The leg is dropped from 10 cm height and the ground reaction forces generated by the impact are measured. Figures B.8 and B.9 present a comparison of the ground reaction forces measured by a 3-axis Kistler 9260AA6 force platform, by the foot sensor and by loadcells. Indeed, since the leg can be considered as a fixed base manipulator to whom the ground applies external

B.1. Six axis foot sensor design

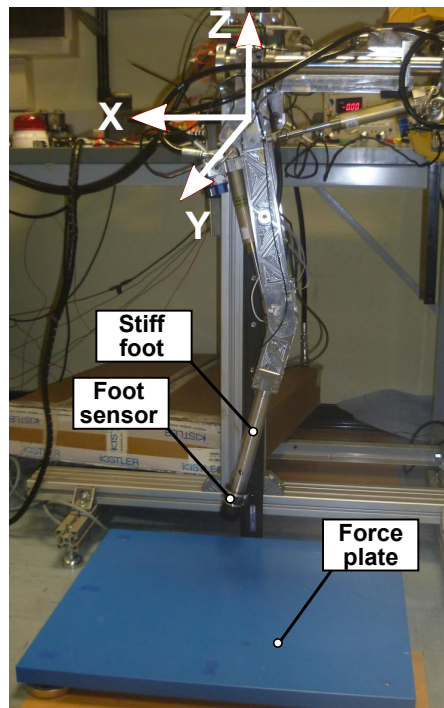


Figure B.7: Picture of the leg mounted on a vertical slider setup to perform drop tests for the evaluation of the foot sensor. The leg base frame is depicted with white arrows.

forces, the (4.23) is valid to estimate ground reaction forces using joint torque (loadcells) data. To enable the comparison, the measurements from these different sensors (which are normally

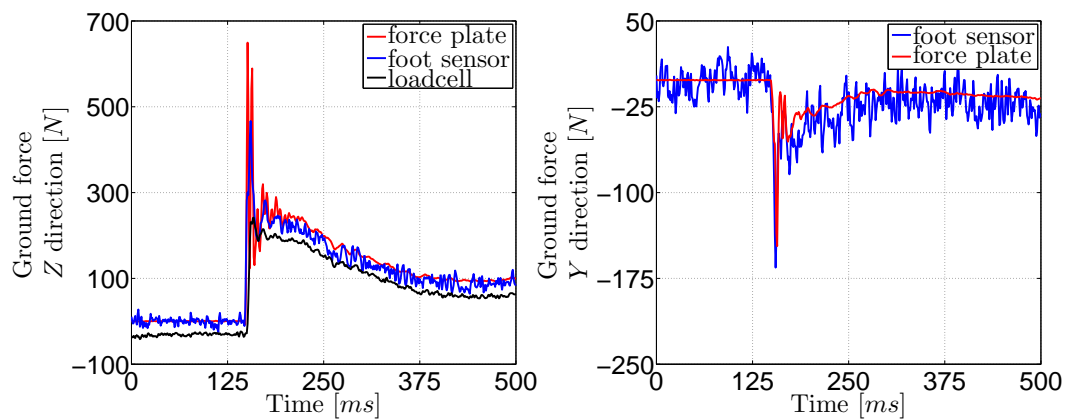


Figure B.8: Dynamic experimental tests: 10 cm drop down of the leg. The plots show the time response of the ground forces measured by the foot sensor (blue), by the force plate (red), and by the loadcells (black) for Z (left) and Y (right) direction .

B. DESIGN OF COMPONENTS

defined in their respective local frames) are all projected in the base frame of the leg (through appropriate homogeneous transformation). The leg that is mounted on the slider is equipped only with the two hydraulic joints (*HFE* and *KFE*); therefore a fixed angle of 15° is set for the adduction/abduction (*HAA*) in the clamping fixture that attaches the leg to the slider. This enables to have a *Y* force different from zero. The leg base frame is depicted in Fig. B.7. The experimental results presented in Fig. B.8 and B.9 show that the forces measured by the foot sensor are in agreement with the ones measured by a commercial force plate for all the directions. Comparing with the forces estimated by loadcell measurements, it can be noticed that the foot sensor captures well the high dynamics of the contact forces while the loadcell presents a more filtered response. This is due to the fact that the loadcells are located at the end of the piston rod and are not directly sensing the contact forces. This fact together with the presence of a structural compliance (any mechanical structure is never completely rigid) of the lower-leg are responsible for this "low-pass filtering" effect. Looking at the loadcell-based

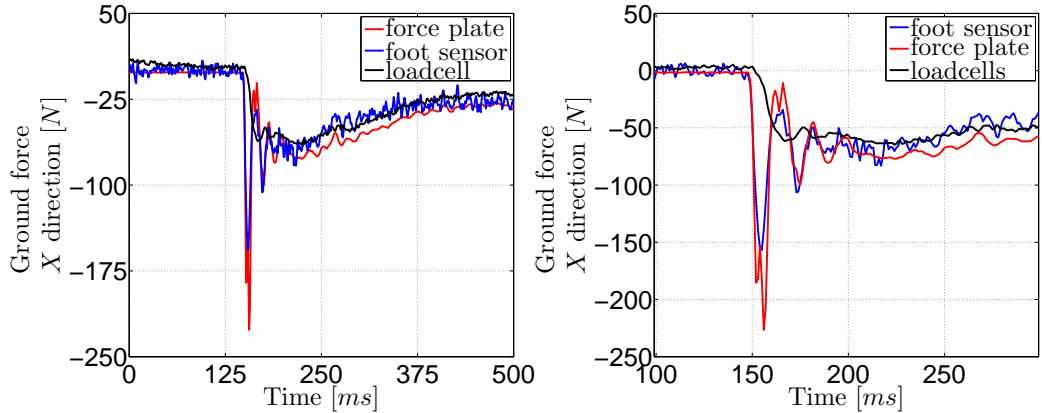


Figure B.9: Dynamic experimental tests: 10 cm drop down of the leg. The plots show the time response of the ground forces measured by the foot sensor (blue), by the force plate (red), and by the loadcells (black) for the *X* direction. Right figure illustrates a magnified view of the impact moment. The signal with less frequency content is the loadcell measurement which is filtered by the structural compliance of the lower-leg.

measurement (black curve) in the figures it can be noticed that this is not zero before the impact. As explained in Section 4.2.4, this is due to an intrinsic limitation of the loadcell's approach to estimate ground forces. This resides in the fact that inertia and gravity forces are measured together with contact forces. The outcome is that an artifact contact force is estimated also when there is no contact (e.g. the leg is moving in the air). This demonstrates that having a foot sensor located at the contact point is a more accurate way to measure contact forces.

B.2 Passive foot design

The design and construction of a passive foot for the HyQ robot leg is described in the following section. The passive compliant element is a linear spring. An appropriate design enables the possibility to fit springs with different size and stiffness. The spring deflection is measured by a displacement sensor. Since the foot must be suitable for locomotion (see Chapter 5), to accomplish a proper design we followed some criteria, that are listed below:

- **Easy to mount:** small number of components.
- **Rugged :** suitable for operating in outdoor environment.
- **Robust:** it must withstand high flexional moments (e.g when the robot falls on the feet with the lowerleg in a non-vertical configuration) and high impact forces.
- **Lightweight:** reduced unsprung mass and in general light weight material.
- **Compact:** reduced volume to easily fit in the lowerleg of HyQ as a replacement of the original stiff foot.

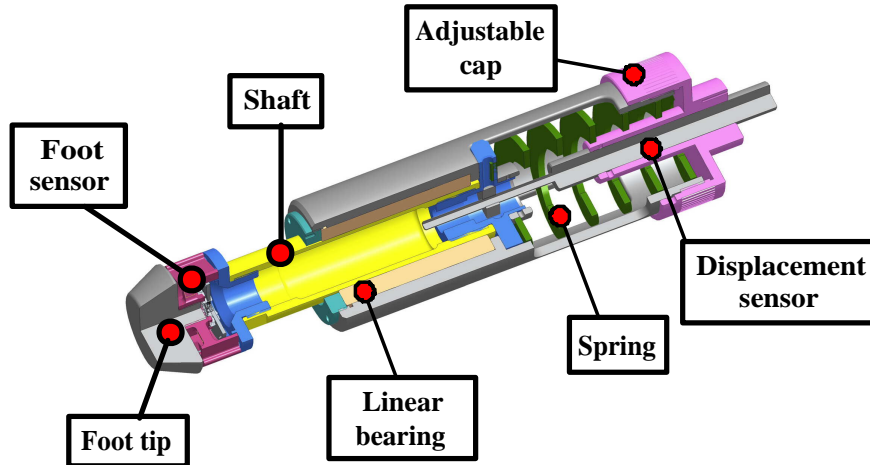


Figure B.10: Cut view of the passive foot. An adjustable cap allows to fit springs with different stiffness.

The components of the foot are listed in Table B.4 and depicted in Fig. B.10. Figure B.12 illustrates an exploded view of the assembly. The table reports the weight in g of all the components. The total weight of the foot ranges from 1.3 kg to 1.65 kg depending on which type of spring is mounted. To simplify the replacement of the inner passive spring, an adjustable cap has been designed (Fig.B.10). This allows an easy dismounting of the main body for the

B. DESIGN OF COMPONENTS



Figure B.11: Picture of the built prototype of the passive foot.

Table B.4: Passive foot components.

Name	Supplier	Model	Mass [g]
Support tap	machined	-	128
Support	machined	-	278
Bearing tap	machined	-	22
Shaft	machined	-	223
Shaft tap	machined	-	58
6 axis foot sensor	machined	-	105
Foot tip	Angst-pfister	APSOvib type G	70
Potentiometer	Burster	8709-5050	34
Linear bearing	Ondrives	LBE30	307
Spring	Spring Master	D13600/CL38x89/C51x89	80/200/430



Figure B.12: CAD exploded view of the passive foot.

spring replacement. The other purpose of the cap it to adjust the angular position of the main body (a set of grub screws located on its periphery will hold the position in order to have the foot sensor frame aligned with the lower-leg link frame. This is of great importance because, thanks to the kinematic transformations, is possible to map the measured forces, that are expressed in the *foot frame*, into the base frame.

B.2.1 Design choices

B.2.1.1 Bearing

In order to achieve the prismatic joint that enables the motion due to the spring compression, a linear ball bearing was located inside the main body. This allows the movement of the shaft during the spring compression. A linear ball bearing was chosen instead of a simpler bushing because of the reduced coefficient of friction. We took advantage from the Ondrives linear bearings which are equipped with a steel housing that results in higher resistance to impact shocks. Moreover, we selected the model bearing to be able to withstand a shock force of 500 N acting at the foot tip with perpendicular to the direction of the lower-leg axis. By equilibrium of forces/moment of forces it can be computed that this force generates transversal forces of 1100N on the bearing. Among the different Ondrives models we chose the LBE30 that has a small diameter (30 mm) and enough dynamic load rating (1500 N both on transversal and longitudinal directions).

B.2.1.2 Shaft

Most parts of the machined components of the foot are made in Ergal (type 7075), an aluminium alloy that is widely used in the aerospace industry due to its excellent strength-to-weight ratio. In particular it has a mass density of 2810 kg/m^3 and yield stress of up to 520 MPa . However for a critical part as the shaft, where a higher strength is needed, a stainless steel AISI 304 material has been chosen. This creates additional weight due to the higher density of the steel. Therefore an iterative FEM analysis has been performed to find out the minimum shaft wall thickness (2.5 mm) for which a 1000N transversal force applied at one end, will create a stress that is inside the limits of the material. As a general rule of thumb, the material has also been removed in other components in the regions that had no structural functions.

B.2.1.3 Springs

The foot has been designed to accommodate different springs and to adjust their pre-compression. In particular three kinds of linear springs (Springmaster), able to store different energy and develop different forces at maximum compression, have been selected. The spring's characteristics are listed in Table B.5. Non linear springs have also been investigated but we abandoned the idea due to their design complexity. The maximum compression of the foot has been chosen to be 35mm considering the maximum compression of the softer spring (D13600 with $K_f = 16 \text{ kN/m}$) that is indicated in Table 5.1. A value of 35mm has been considered as the

B. DESIGN OF COMPONENTS

maximum acceptable (not controllable) error in the foot position tracking to not jeopardize body stability.

Table B.5: Springs characteristics

Model	Stiffness [kN/m]	Max force[N]	Energy stored [J]	Type
C51x89	109	3050	66	hard
CL38x89	51	1785	31	medium
D13600	16	560	10	soft

B.2.1.4 Displacement sensor

We investigated different solutions for the selection of the displacement sensor. The requirements mainly regarded ruggedness, measurement range (0-35 mm) and the necessity of reduced onboard conditioning electronics. It turned out that the possible solutions were based on magnetic, optical, capacitive, inductive (LVDT), resistive (potentiometer) devices. LVDT requires complex electronics for the driving signal generation. Capacitive has too small range, magnetic has not enough precision. Of the different options, the potentiometer-base displacement sensor was the best trade-off because of its associated roughness, good resolution and dynamics.

B.3 Construction of the magneto-rheological compliant foot

In this section we will describe the design of the magnetorheologically damped compliant foot (MR foot) used for the experiments of Chapter 6. This work was made in collaboration with Esa Kostamo (Aalto university). An assembly of the designed prototype is presented in Fig.B.13 where a CAD cross-section details the main functional components of the MR foot. The end caps 4 and 12 are machined of aluminum and the material of the piston shaft 2 is a surface-hardened steel guide bar. Magnetically active parts in the construction are the piston 10 and the cylinder 11 which are manufactured of magnetically soft iron. The coil around the piston is wound of standard 0.4 mm enameled copper wire. The MR compliant foot is assembled as shown in Fig. B.13 and the remaining volume inside the cylinder is filled with magneto-rheological fluid. The piston is manufactured to have one millimeter smaller diameter in relation to the inner diameter of the cylinder tube. This difference forms a 0.5 mm annular fluid gap between the piston and the cylinder which enables the MR fluid to flow from one side of the piston to the other when the compliant foot is compressed or extended. Since

B.3. Construction of the magneto-rheological compliant foot

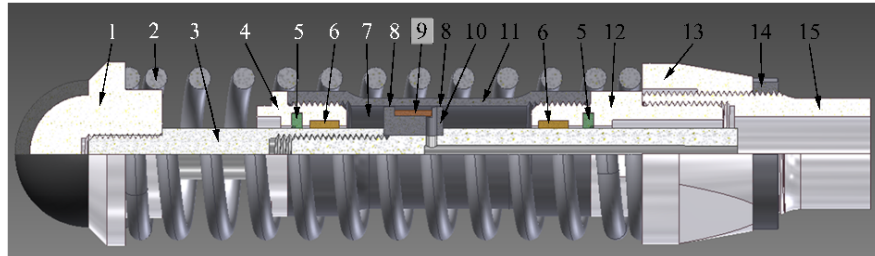


Figure B.13: CAD cross-section view of the MR foot. Numbered components: **1**: rubber coated foot tip, **2**: spring, **3**: piston shaft, **4**: lower end cap, **5**: seal, **6**: sliding bushing, **7**: MR fluid, **8**: MR fluid gap, **9**: solenoid, **10**: piston, **11**: cylinder, **12**: upper end cap.

the hydraulic components of the damper are designed to be symmetric, no gas reservoir is needed to compensate the movement of the piston. The solenoid around the piston is used

Table B.6: MR foot specifications

Weight [kg]	1.25
Total length [mm]	232
Stroke [mm]	34
Largest diameter [mm]	49
Cylinder inner diameter [mm]	26
Piston diameter[mm]	25
Fluid gap [mm]	0,5
Spring constant [kN/m]	16
Max damping force [N] (4A electric current)	485
Operating bandwidth [Hz], -3dB limit	≥ 100
Max input power [W]	≤ 4

to generate the magnetic field between the piston and the cylinder. When electric current is applied, magnetic flux circulates in-between the piston and the cylinder tube over two fluid gaps (**8**: in Fig. B.13) and induces an increase in the MR fluids yield stress. This increase in yield stress restricts the fluid flow over the piston, generating pressure difference over the piston and consequently generating damping force when the piston rod is moved. Because the change in the fluids rheological properties is completely reversible, the damping force can be continuously controlled by adjusting the electric current in the coil. The key parameters of the magneto-rheological compliant foot are listed in Table B.6.

B. DESIGN OF COMPONENTS

B.3.1 Performances

First static performances of the MR damper was identified by using an Easydur MZ3 material testing device (stress-strain machine). In the experiment the magneto-rheological compliant foot was mounted to the test setup without the spring in order to be able to study only the characteristic properties of the MR damper. In one measurement the damper was compressed and extended five times at a constant velocity and electric currents from 0 A to 2 A were supplied. From the measured results the constant velocity and the mean constant force were calculated resulting in five vertical force points in positive and negative directions for the static characteristic curves. This measuring procedure was repeated 60 times with different velocities in order to identify the static performance of the developed MR damper. The characteristic curves are presented in Fig. B.14. The zero speed force depends on the electric current induced yield

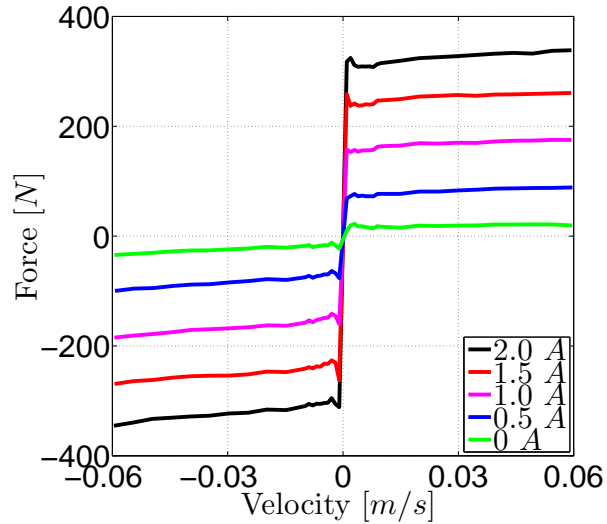


Figure B.14: Experimental static force-velocity characteristic for different electric current inputs (0-2 A).

stress of the MR fluid and the friction in the seals and sliding bushings. In addition the viscous forces will increase the measured total force as the damper begins to move. The force response of the damper was also studied as a function of the applied electric current. In this measurement the damper was compressed at a constant velocity of 40 mm/s and electric currents with increment of 1 A up to 4 A were applied. The measured damping force is presented in Fig. B.15.

B.3. Construction of the magneto-rheological compliant foot

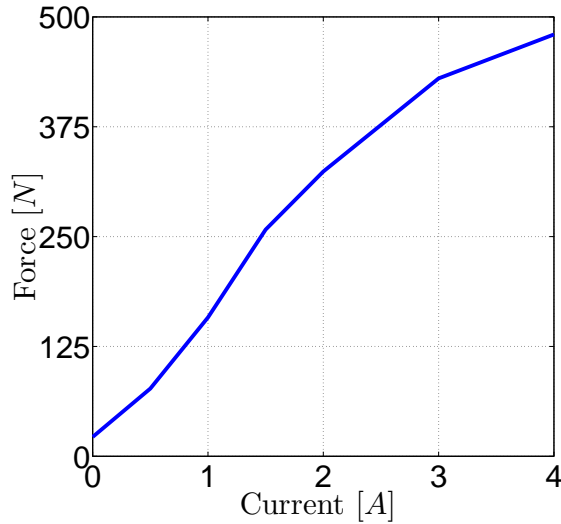


Figure B.15: Measured damping force responses of the magneto-rheological damper of the MR foot as a function of the electric current.

B.3.1.1 Frequency response measurements

The dynamic performance of the MR damper was studied by frequency response measurements. In these measurements the damper was compressed and extended at a constant velocity of 30 mm/s and a sinusoidal current excitation was used. The peak-to-peak value of the current excitation was 2 A and the measured frequency band ranged from 2 Hz to 100 Hz with an increment of 2 Hz . The data were acquired at 1 kHz . The magnitude and phase curves of the frequency response measurement are presented in Fig. B.16. The figure shows that the open loop bandwidth for the damping force is around 100 Hz .

B. DESIGN OF COMPONENTS

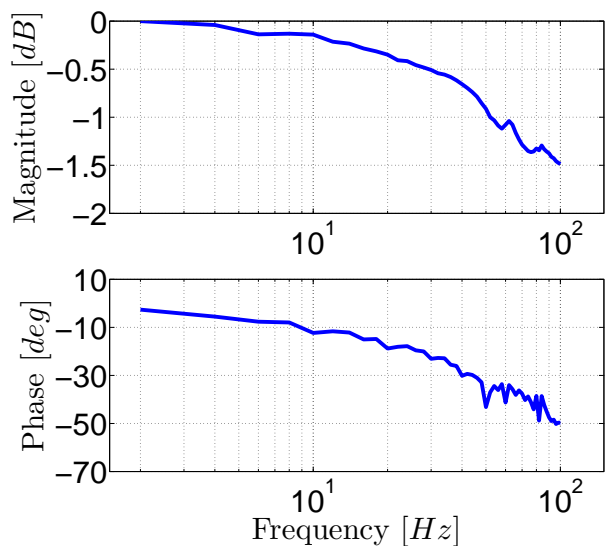


Figure B.16: Frequency response of the damping force of the magneto-rheological damper.

B.4 Publications and patents

MICHELE Focchi was born in Rimini, Italy. He holds a Master of Science in Control System Engineering from Politecnico di Milano in 2007. His final project dealt with dynamic modelling of hydraulic turbines for energy generation carried out at the Federal University of Santa Catarina, Brazil. Until 2008 he worked at the *R&D* department of Indesit company where he worked with design and dynamic modeling of hydraulic, thermal and mechanical phenomena and system identification for house appliances. On the 2009 he was employed as a fellow at the Advanced Robotic Department (ADVR) at IIT developing a prototype of Novel concept for an air-pressure driven micro-turbine for power generation for which he obtained an international patent and several awards. He also gained some experience with force control with pneumatic muscles. In 2010 he started a PhD getting involved in the Hydraulically Actuated Quadruped Robot project at the Dynamic Legged Systems Laboratory at ADVR under the supervision of Prof. Darwin Caldwell. His research interests range from dynamic locomotion with legged robots, to actuation technologies. He is also involved in the design of components for the HyQ quadruped robot and in the implementation of low-level controllers for locomotion purposes.

B.5 List of publications

Conferences

- **Focchi, M.**; Barasuol V.; Havoutis I., Buchli, J.; Semini C. and Caldwell, D.G. "Local Reflex Generation for Obstacle Negotiation in Quadrupedal Locomotion", Proc. of the 16th Int. Conf. on Climbing and Walking Robots (CLAWAR), 2013
- Boaventura, T.; Semini, C.; Buchli, J.; Frigerio, M.; **Focchi, M.** ; Caldwell, D. G. "Dynamic Torque Control of a Hydraulic Quadruped Robot", IEEE International Conference in Robotics and Automation, 2012, 1889-1894
- Semini, C.; Khan, H; Frigerio, M.; Boaventura, T.; **Focchi, M.**; Buchli, J. and Caldwell,D. G., "Design and Scaling of Versatile Quadruped Robots", Int. Conf. on Climbing and Walking Robots (CLAWAR), 2012.
- Boaventura, T.; **Focchi, M.**; Frigerio, M.; Buchli, J.; Semini, C.; Medrano-Cerda, G. A. ; Caldwell, D. G. "On the role of load motion compensation in high-performance force control", IEEE/RSJ International Conference on Intelligent Robots and Systems (IROS), 2012, 4066-4071

B. DESIGN OF COMPONENTS

- **Focchi, M.**; Boaventura, T.; Semini, C.; Frigerio, M.; Buchli, J. ; Caldwell, D. G. "Torque-control Based Compliant Actuation of a Quadruped Robot", Proc. of the 12th IEEE Int. Workshop on Advanced Motion Control (AMC), 2012
- Semini, C.; Buchli, J.; Frigerio, M.; Boaventura, T.; **Focchi, M.**; Guglielmino, E.; Cannella, F.; Tsagarakis, N. G. ; Caldwell, D. G. "HyQ – A Dynamic Locomotion Research Platform", Int.l Workshop on Bio-Inspired Robots, Nantes (France), 2011
- **Focchi, M.**; Persico, G.; Guglielmino, E. ; Caldwell, D. G. "Novel concept for an air-pressure driven micro-turbine for power generation", ASME Turbo Expo, 2011
- **M. Focchi**, E. Guglielmino, **C. Semini**, T. B. Cunha, Y. S. Yang, D. G. Caldwell, "Control of a Hydraulically-Actuated Quadruped Robot Leg," IEEE Int. Conf. on Robotics and Automation (ICRA), 2010.
- **Focchi, M.**; Guglielmino, E.; Semini, C.; Parmiggiani, A.; Tsagarakis, N.; Vanderborght, B. ; Caldwell, D. G. "Water/air performance analysis of a fluidic muscle", IEEE/RSJ International Conference on Intelligent Robots and Systems (IROS), 2010, 2194-2199

Journals

- **Focchi, M.**; Cerda, G. A.; Boaventura, T.; Frigerio, M.; Semini, C.; Buchli, J. ; Caldwell, D. G. "Robot Impedance Control and Passivity Analysis with Inner Torque and Velocity Feedback Loops", Transactions on Industrial Electronics, 2013 (under review)
- Kostamo, E.;**Focchi, M.**; Guglielmino, E.; Kostamo,J.; Semini, C.; Buchli, J; Pietola, M.; Caldwell, D.G. "A Magnetorheologically Damped Compliant Foot for a Legged Robotic Application", Journal of Mechanical Design, 2013 (under review)
- Semini, C.; Tsagarakis, N.; Guglielmino, E.; **Focchi, M.**; Cannella, F. ; Caldwell, D. "Design of HyQ—a hydraulically and electrically actuated quadruped robot", Proceedings of the Institution of Mechanical Engineers, Part I: Journal of Systems and Control Engineering, SAGE Publications, 2011, 225, 831-849

B.6 Patents

- **Focchi, M.**; Guglielmino, E.; Pane, G.; Cordasco, S.; Tacchino, C. ; Caldwell, D. G. "Device for generating electric power from a source of air or other gas or fluid under pressure", WO 2012/004738 A1, 2012

B.7 Awards

Some prizes have been obtained with the microturbine project:

- 1st prize "Premio Nazionale Innovazione", Bari, 2013 (25keuro)
- 1st prize "StartCup il sole 24 ore", Genova, 2012
- 1st prize "ItaliaCamp", Verona, 2012

B. DESIGN OF COMPONENTS

References

- Albu-Schäffer, A., Ott, C., and Hirzinger, G. (2007). A unified passivity-based control framework for position, torque and impedance control of flexible joint robots. *The International Journal of Robotics Research*, 26(1):23–39.
- Alexander, M. (1988). *Elastic mechanisms in animal movement*. Cambridge University Press.
- Alexander, R. (1990). Three uses for springs in legged locomotion. *The International Journal of Robotics Research*, 9(2):53–61.
- An, C. H. (1986). *Trajectory and force control of a direct drive arm*. PhD thesis.
- An, C. H. and Hollerbach, J. M. (1987). Dynamic stability issues in force control of manipulators. In *American Control Conference, 1987*, pages 821–827.
- Anderson, B. D. O. and Vongpanitlerd, S. (2006). *Network analysis and synthesis: a modern systems theory approach*. Courier Dover Publications.
- Biewener, A. (1983). Allometry of quadrupedal locomotion: the scaling of duty factor, bone curvature and limb orientation to body size. *Journal of Experimental Biology*, 105(1):147–171.
- Bin Hammam, G., Orin, D. E., and Dariush, B. (2010). Whole-body humanoid control from upper-body task specifications. In *Robotics and Automation (ICRA), 2010 IEEE International Conference on*, pages 3398–3405.
- Bishop, R. E. D. and Johnson, D. C. (2011). *The mechanics of vibration*. Cambridge University Press.
- Blickhan, R. (1989). The spring-mass model for running and hopping. *J. Biomechanics*, 22(11–12):1217–1227.

REFERENCES

- Boaventura, T. (2013). *Hydraulic Compliance Control of the Quadruped Robot HyQ*. PhD thesis, Italian Institute of Technology and University of Genoa.
- Boaventura, T., Focchi, M., Frigerio, M., Buchli, J., Semini, C., Medrano-Cerda, G. A., and Caldwell, D. G. (2012a). On the role of load motion compensation in high-performance force control. In *IEEE/RSJ International Conference on Intelligent Robots and Systems*.
- Boaventura, T., Semini, C., Buchli, J., Frigerio, M., Focchi, M., and Caldwell, D. G. (2012b). Dynamic torque control of a hydraulic quadruped robot. In *IEEE International Conference in Robotics and Automation*, pages 1889–1894.
- Bossis, G., Lacis, S., Meunier, A., and Volkova, O. (2002). Magnetorheological fluids. *Journal of Magnetism and Magnetic Materials*, 252:224–228.
- Boston Dynamics Corp. (2011). website. Accessed February 2013 at http://www.bostondynamics.com/robot_petman.html. Press release information.
- Boston Dynamics Corp. (2012). Website. Accessed February 2012 at <http://www.bostondynamics.com>.
- Broistedt, H., Petz, M., and Tutsch, R. (2009). Force transducer based on a geometric-optical displacement sensor. In *Optomechatronic Technologies, 2009. ISOT 2009. International Symposium on*, pages 164–168.
- Buchli, J., Kalakrishnan, M., Mistry, M., Pastor, P., and Schaal, S. (2009a). Compliant quadruped locomotion over rough terrain. In *IEEE/RSJ International Conference on Intelligent Robots and Systems*.
- Buchli, J., Kalakrishnan, M., Mistry, M., Pastor, P., and Schaal, S. (2009b). Compliant quadruped locomotion over rough terrain. In *Proceedings of IEEE/RSJ International Conference on Intelligent Robots and Systems (IROS)*, pages 814–820.
- Buehler, M., Playter, R., and Raibert, M. (2005). Robots step outside. In *Int. Symp. Adaptive Motion of Animals and Machines (AMAM)*.
- Carrella, A. (2011). Force transmissibility of a nonlinear vibration isolator with high-static-low-dynamic-stiffness.
- Cavagna, G. A., Saibene, F. P., and Margaria, R. (1964). Mechanical work in running. *J. Appl. Physiol.*, 19(2):249–256.

REFERENCES

- Cheng, G., Hyon, S., Morimoto, J., Ude, A., Hale, J. G., Colvin, G., W., S., and Jacobsen, S. C. (2007). Cb: a humanoid research platform for exploring neuroscience. *Journal of Advanced Robotics*, 21:1097–1114.
- Chew, C., Hong, G., and Zhou, W. (2004). Series damper actuator: a novel force/torque control actuator. In *4th IEEE/RAS International Conference on Humanoid Robots, 2004*, volume 2, pages 533–546.
- Colgate, E. and Hogan, N. (1989). An analysis of contact instability in terms of passive physical equivalents. In *IEEE International Conference on Robotics and Automation*, pages 404–409 vol.1.
- Colgate, J. (1986). *The control of dynamically interacting systems*. PhD thesis, Massachusetts Institute of Technology, Cambridge, Massachusetts.
- Colgate, J. E. (1994). Coupled stability of multiport systems – theory and experiments. *Transactions of ASME, Journal of Dynamic Systems, Measurement and Control*, 116:419–428.
- Colgate, J. E. and Brown, J. M. (1994). Factors affecting the z-width of a haptic display. In *IEEE International Conference on Robotics and Automation*, pages 3205–3210.
- Colgate, J. E. and Hogan, N. (1988). Robust control of dynamically interacting systems. *International Journal of Control*, 48(1):65–88.
- Colgate, J. E. and Schenkel, G. G. (1997). Passivity of a class of sampled-data systems: Application to haptic interfaces. *Journal of Robotic Systems*, 14(1):37–47.
- Conrad, F. and Jensen, C. (1987). Design of hydraulic force control systems with state estimate feedback. In *IFAC 10th Triennial Congress*, pages 307–31, Munich, Germany.
- Cunha, T. B., Semini, C., Guglielmino, E., De Negri, V. J., Yang, Y., and Caldwell, D. G. (2010). Gain scheduling control for the hydraulic actuation of the hyq robot leg. In De Negri, V. J., Perondi, E. A., Cunha, M. A. B., and Horikawa, O., editors, *ABCM Symposium Series in Mechatronics*, volume 4, pages 673 – 682. ABCM - Brazilian Society of Mechanical Sciences and Engineering, Rio de Janeiro, RJ, Brazil. ISBN 978-85-85769-47-5.
- Dhaouadi, R., Kubo, K., and Tobise, M. (1993). Analysis and compensation of speed drive systems with torsional loads. In *Proc. Conf Power Conversion Conf., Yokohama*, pages 271–277.

REFERENCES

- Dimig, J., Shield, C., French, C., Bailey, F., and Clark, A. (1999). Effective force testing: A method of seismic simulation for structural testing. *J. Structural Engineering*, 125(9):1028–1037.
- Dyke, S., Spencer Jr., B., Quast, P., and Sain, M. (1995). Role of control-structure interaction in protective system design. *Journal of Engineering Mechanics, ASCE*, 121 No.2:322–38.
- Ellis, G. (2000). *Control System Design Guide*. 2nd edition, Academic Press, London.
- Emoteq Inc. (1998). High torque series - brushless dc motors data sheet. Accessed March 2010 at http://www.alliedmotion.com/Data/Documents/HT_High_Torque_Selection_Guide.pdf.
- Eppinger, S. and Seering, W. (1987). Understanding bandwidth limitations in robot force control. In *Robotics and Automation. Proceedings. 1987 IEEE International Conference on*, volume 4, pages 904–909. IEEE.
- Eppinger, S. D. and Seering, W. P. (1992). Three dynamic problems in robot force control. *Robotics and Automation, IEEE Transactions on*, 8(6):751–758.
- Estremera, J. and Waldron, K. J. (2008). Thrust control, stabilization and energetics of a quadruped running robot. *International Journal of Robotics Research*, 27:1135–1151.
- Ferris, D., Louie, M., Farley, C., Ferris, D., Louie, M., and Farley, C. (1998a). Running in the real world: adjusting leg stiffness for different surfaces. *Proceedings of the Royal Society of London. Series B: Biological Sciences*, 265(1400):989–994.
- Ferris, D. P., Louie, M., and Farley, C. T. (1998b). Running in the real world: adjusting leg stiffness for different surfaces. *Proc. R. Soc. Lond. B*, 265:989–994.
- Fischer, D. and Isermann, R. (2004). Mechatronic semi-active and active vehicle suspensions. *Control Engineering Practice*, 12(11):1353–1367.
- Focchi, M., Boaventura, T., Semini, C., Frigerio, M., Buchli, J., and Caldwell, D. G. (2012). Torque-control based compliant actuation of a quadruped robot. In *Proc. of the 12th IEEE Int. Workshop on Advanced Motion Control (AMC)*.
- Frank, A. A. (1968). Automatic control systems for legged locomotion machines. Technical report, DTIC Document.
- Ganguli, A. (2005). *Chatter reduction through active vibration damping*. PhD thesis, Université Libre de Bruxelles.

REFERENCES

- Geyer, H., Seyfarth, A., and Blickhan, R. (2006). Compliant leg behaviour explains basic dynamics of walking and running. *Proceedings of the Royal Society B: Biological Sciences*, 273(1603):2861–2867.
- Gonzales de Santos, P., Garcia, E., and Estremera, J. (2006). *Quadrupedal Locomotion*. Springer London.
- Goswami, A., Espiau, B., and Keramane, A. (1996). Limit cycles and their stability in a passive bipedal gait. In *Robotics and Automation, 1996. Proceedings., 1996 IEEE International Conference on*, volume 1, pages 246–251. IEEE.
- Grizzle, J., Hurst, J., Morris, B., Park, H.-W., and Sreenath, K. (2009). Mabel, a new robotic bipedal walker and runner. In *American Control Conference, 2009. ACC'09.*, pages 2030–2036. IEEE.
- Ham, R., Sugar, T., Vanderborght, B., Hollander, K., and Lefeber, D. (2009). Compliant actuator designs. *Robotics & Automation Magazine, IEEE*, 16(3):81–94.
- Harmonic Drive Inc. (2009). Harmonic gear csd & shd series data sheet. Accessed March 2010 at http://www.harmonicdrive.de/cms/upload/pdf/GK2007/english/1_Component_Sets/3_CSD/CSD_complete_en.pdf.
- Herr, H. and Wilkenfeld, A. (2003). User-adaptive control of a magnetorheological prosthetic knee. *Industrial Robot: An International Journal*, 30(1):42–55.
- Hirose, S., Fukuda, Y., Yoneda, K., Nagakubo, A., Tsukagoshi, H., Arikawa, K., Endo, G., Doi, T., and Hodoshima, R. (2009). Quadruped walking robots at tokyo institute of technology. *IEEE Robotics and Automation Magazine*, 16:104–114.
- Hirzinger, G., Albu-Schaeffer, A., Haehnle, M., Schaefer, I., and Sporer, N. (2001). On a new generation of torque controlled light-weight robots. In *Robotics and Automation, 2001. Proceedings 2001 ICRA. IEEE International Conference on*, volume 4, pages 3356–3363. IEEE.
- Hogan, N. (1985). Impedance control: An approach to manipulation: Part II – Implementation. *ASME, Transactions, Journal of Dynamic Systems, Measurement, and Control*, 107:8–16.
- Hogan, N. and Colgate, E. (1989). Stability problems in contact tasks. In *The robotics review 1*, pages 339–348. MIT Press.

REFERENCES

- Hori, Y., Iseki, H., and Sugiura, K. (1994). Basic consideration of vibration suppression and disturbance rejection control of multi-inertia system using sflac (state feedback and load acceleration control). *IEEE Transactions on Industry Applications*, 30(4):889–896.
- Hutter, M., Gehring, C., Bloesch, M., Hoepflinger, M., Remy, C. D., and Siegwart, R. (2012). Starleth: A compliant quadrupedal robot for fast, efficient, and versatile locomotion. In *Proc. of the International Conference on Climbing and Walking Robots (CLAWAR)*.
- Jalili, N. (2002). A comparative study and analysis of semi-active vibration-control systems. *Journal of vibration and acoustics*, 124(4):593–605.
- Janabi-Sharifi, F., Hayward, V., and Chen, C.-S. (2000). Discrete-time adaptive windowing for velocity estimation. *Control Systems Technology, IEEE Transactions on*, 8(6):1003 –1009.
- Kajita, S., Kanehiro, F., Kaneko, K., Yokoi, K., and Hirukawa, H. (2001). The 3d linear inverted pendulum mode: A simple modeling for a biped walking pattern generation. In *Intelligent Robots and Systems, 2001. Proceedings. 2001 IEEE/RSJ International Conference on*, volume 1, pages 239–246. IEEE.
- Kaneko, K., Suzuki, N., Ohnishi, K., and Tanie, K. (1991). High stiffness torque control for a geared dc motor based on acceleration controller. In *Proc. IECON '91. Conf. Int Industrial Electronics, Control and Instrumentation*, pages 849–854.
- Kazerooni, H., Sheridan, T., and Houpt, P. (1986). Robust compliant motion for manipulators, part i: The fundamental concepts of compliant motion. *IEEE Journal of Robotics and Automation*, 2(2):83–92.
- Khatib, O. (1987). A unified approach for motion and force control of robot manipulators: The operational space formulation. *Robotics and Automation, IEEE Journal of*, 3(1):43–53.
- Kong, K., Bae, J., and Tomizuka, M. (2009). Control of rotary series elastic actuator for ideal force-mode actuation in human–robot interaction applications. *Mechatronics, IEEE/ASME Transactions on*, 14(1):105–118.
- Koolen, T., De Boer, T., Rebula, J., Goswami, A., and Pratt, J. (2012). Capturability-based analysis and control of legged locomotion, part 1: Theory and application to three simple gait models. *The International Journal of Robotics Research*, 31(9):1094–1113.
- Krupp, B. T. and Pratt, J. E. (2006). A power autonomous monopedal robot. In *Proceedings of SPIE-The International Society for Optical Engineering*, volume 6201.

REFERENCES

- Kuo, A. (2007). Choosing your steps carefully. *Robotics & Automation Magazine, IEEE*, 14(2):18–29.
- Lawrence, D. A. (1988). Impedance control stability properties in common implementations. In *Proc. Conf. IEEE Int Robotics and Automation*, pages 1185–1190.
- Lawrence, D. A. (1989). Actuator limitations on achievable manipulator impedance. In *Robotics and Automation, 1989. Proceedings., 1989 IEEE International Conference on*, pages 560–565. IEEE.
- Liston, R. and Mosher, R. (1968). A versatile walking truck. In *Proceedings of the Transportation Engineering Conference*.
- McGeer, T. (1990). Passive dynamic walking. *International Journal of Robotics Research*, 9(2):62–82.
- McMillan, G. K., Considine, D. M., Bristol, E., Hall, G., Hansen, P. D., Higgins, S. P., Magison, E., Nelson, J. M., Osborne, R. L., Stevenson, J., et al. (1999). *Process/industrial instruments and controls handbook*. McGraw Hill.
- Meka robotics (2011). A2 compliant arm. www.mekabot.com/arm.html.
- Mistry, M., Buchli, J., and Schaal, S. (2010). Inverse dynamics control of floating base systems using orthogonal decomposition. In *IEEE International Conference on Robotics and Automation (ICRA), 2010*, pages 3406–3412. IEEE.
- MOOG Inc. (2003). *Data Sheet of E024 Series Microvalve*.
- Mosadeghzad, M., Medrano-Cerda, G., Saglia, J., Tsagarakis, N. G., Caldwell, D., et al. (2012). Comparison of various active impedance control approaches, modeling, implementation, passivity, stability and trade-offs. In *Advanced Intelligent Mechatronics (AIM), 2012 IEEE/ASME International Conference on*, pages 342–348. IEEE.
- Murakami, T., Yu, F., and Ohnishi, K. (1993). Torque sensorless control in multidegree-of-freedom manipulator. *Industrial Electronics, IEEE Transactions on*, 40(2):259–265.
- Murphy, M. P., Saunders, A., Moreira, C., Rizzi, A. A., and Raibert, M. (2011). The littledog robot. *The International Journal of Robotics Research*, 30(2):145–149.
- Mussa-Ivaldi, F., Hogan, N., and Bizzi, E. (1985). Neural, mechanical, and geometric factors subserving arm posture in humans. *The Journal of Neuroscience*, 5(10):2732–2743.

REFERENCES

- Nichol, J. G., Singh, S. P., Waldron, K. J., Palmer, L. R., and Orin, D. E. (2004). System design of a quadrupedal galloping machine. *The International Journal of Robotics Research*, 23(10-11):1013–1027.
- Ohnishi, K., Shibata, M., and Murakami, T. (1996). Motion control for advanced mechatronics. *Mechatronics, IEEE/ASME Transactions on*, 1(1):56–67.
- Poulakakis, I., Smith, J. A., and Buehler, M. (2005). Modeling and experiments of untethered quadrupedal running with a bounding gait: The scout II robot. *International Journal of Robotics Research*, 24:239–256.
- Pratt, G. (2002). Low impedance walking robots. *Integr Comp Biol*, 42(1):174–181.
- Pratt, G. and Williamson, M. (1995). Series elastic actuators. In *IEEE International Conference on Intelligent Robots and Systems (IROS)*.
- Pratt, G., Williamson, M., Dillworth, P., Pratt, J., and Wright, A. (1997). Stiffness isn't everything. *Experimental Robotics IV*, pages 253–262.
- Pratt, J., Carff, J., Rakunov, S., and Goswami, A. (2006). Capture point: A step toward humanoid push recovery. In *Humanoids*.
- Pratt, J., Chew, C., Torres, A., Dilworth, P., and Pratt, G. (2001). Virtual model control: An intuitive approach for bipedal locomotion. *The International Journal of Robotics Research*, 20(2):129–143.
- Raibert, M., Blankespoor, K., Nelson, G., Playter, R., and the BigDog Team (2008). Bigdog, the rough-terrain quadruped robot. In *Proceedings of the 17th World Congress The International Federation of Automatic Control (IFAC)*.
- Raibert, M. and Craig, J. (1981). Hybrid position/force control of manipulators. *ASME Journal of Dynamic Systems, Measurement, and Control*, 107:126–133.
- Raytheon Sarcos (2010). Website. Accessed March 2010 at http://www.raytheon.com/newsroom/technology/rtn08_exoskeleton/.
- Robinson, D. (2000). *Design and analysis of series elasticity in closed-loop actuator force control*. PhD thesis, Massachusetts Institute of Technology.
- Rutishauser, S., Sprowitz, A., Righetti, L., and Ijspeert, A. J. (2008). Passive compliant quadruped robot using central pattern generators for locomotion control. In *Biomedical*

REFERENCES

- Robotics and Biomechatronics, 2008. BioRob 2008. 2nd IEEE RAS & EMBS International Conference on*, pages 710–715. IEEE.
- Schaal, S. (2009). The sl simulation and real-time control software package. *University of Southern California*.
- Sciavicco, L. and Siciliano, B. (2000). *Modelling and Control of Robot Manipulators*. Springer.
- Sciavicco, L. and Siciliano, B. (2001). *Modelling And Control Of Robot Manipulators*. Springer.
- Semini, C. (2010). *HyQ – Design and Development of a Hydraulically Actuated Quadruped Robot*. PhD thesis, Italian Institute of Technology and University of Genoa.
- Semini, C., Buchli, J., Frigerio, M., Boaventura, T., Focchi, M., Guglielmino, E., Cannella, F., Tsagarakis, N. G., and Caldwell, D. G. (2011a). HyQ – a dynamic locomotion research platform. In *Int.l Workshop on Bio-Inspired Robots, Nantes (France)*.
- Semini, C., Tsagarakis, N., Guglielmino, E., Focchi, M., Cannella, F., and Caldwell, D. (2011b). Design of hyq—a hydraulically and electrically actuated quadruped robot. *Proceedings of the Institution of Mechanical Engineers, Part I: Journal of Systems and Control Engineering*, 225(6):831–849.
- Semini, C., Tsagarakis, N. G., Guglielmino, E., Focchi, M., Cannella, F., and Caldwell, D. G. (2011c). Design of HyQ - a hydraulically and electrically actuated quadruped robot. *IMechE Part I: J. of Systems and Control Engineering*, 225(6):831–849.
- Sentis, L. (2007). *Synthesis and control of whole-body behaviors in humanoid systems*. PhD thesis, Stanford University.
- Seok, S., Wang, A., Otten, D., and Kim, S. (2012). Actuator design for high force proprioceptive control in fast legged locomotion. In *Intelligent Robots and Systems (IROS), 2012 IEEE/RSJ International Conference on*, pages 1970–1975. IEEE.
- Shin, D., Sardellitti, I., and Khatib, O. (2008). A hybrid actuation approach for human-friendly robot design. In *Robotics and Automation, 2008. ICRA 2008. IEEE International Conference on*, pages 1747–1752. IEEE.
- Siciliano, B. and Villani, L. (1999). *Robot force control*, volume 540. Springer.

REFERENCES

- Song, S. and Chen, Y. (1991). A free gait algorithm for quadrupedal walking machines. *Journal of Terramechanics*, 28(1):33–48.
- Song, S.-M. and Waldron, K. J. (1989). *Machines That Walk - The Adaptive Suspension Vehicle*. The MIT Press.
- Stewart, D. (1965). A platform with six degrees of freedom. *Proceedings of the Institution of Mechanical Engineers*, 180(1):371–386.
- Taylor, M. (2011). *A compact series elastic actuator for bipedal robots with human-like dynamic performance*. PhD thesis, MS Thesis, Carnegie Mellon University.
- Tsagarakis, N. G., Morfey, S., Cerdá, G. M., Li, Z., and Caldwell, D. G. (2013). Development of compliant humanoid robot COMAN: Body design and stiffness tuning. In *IEEE International Conference on Robotics and Automation (ICRA)*. [accepted for publication].
- Tsagarakis, N. G., Sardellitti, I., and Caldwell, D. G. (2011). A new variable stiffness actuator (compact-vsa): Design and modelling. In *Intelligent Robots and Systems (IROS), 2011 IEEE/RSJ International Conference on*, pages 378 –383.
- Vallery, H., Ekkelenkamp, R., Van Der Kooij, H., and Buss, M. (2007). Passive and accurate torque control of series elastic actuators. In *Intelligent Robots and Systems, 2007. IROS 2007. IEEE/RSJ International Conference on*, pages 3534–3538. IEEE.
- von Jose de Gea Fernandez (2010). *Predictive Context-Based Adaptive Compliance for Interaction Control of Robot Manipulators*. PhD thesis, Universitat Bremen.
- Vukobratovic, M. and Borovac, B. (2004). Zero-moment point - thirty five years of its life. *International Journal of Humanoid Robotics*, 1(1):157–173.
- Walker, D. S. and Niemeyer, G. (2010). Examining the benefits of variable impedance actuation. In *Intelligent Robots and Systems (IROS), 2010 IEEE/RSJ International Conference on*, pages 4855–4861. IEEE.
- Walker, D. S., Thoma, D. J., and Niemeyer, G. (2009). Variable impedance magnetorheological clutch actuator and telerobotic implementation. In *Intelligent Robots and Systems, 2009. IROS 2009. IEEE/RSJ International Conference on*, pages 2885–2891. IEEE.
- Wandfluh (2007). Proportional spool valves - ng3-mini. (online). www.wandfluh.com.

REFERENCES

- Whitney, D. E. (1985). Historical perspective and state of the art in robot force control. In *Robotics and Automation. Proceedings. 1985 IEEE International Conference on*, volume 2, pages 262 – 268.
- Williamson, M. (1995). Series elastic actuators. Master's thesis, MIT.
- Wyeth, G. (2006). Control issues for velocity sourced series elastic actuators. In *Proceedings of the Australasian Conference on Robotics and Automation 2006*. Australian Robotics and Automation Association Inc.
- Zeng, G. and Hemami, A. (1997). An overview of robot force control. *Robotica*, 15(5):473–482.
- Zinn, M., Roth, B., Khatib, O., and Salisbury, J. K. (2004). A new actuation approach for human friendly robot design. *The international journal of robotics research*, 23(4-5):379–398.